UC Santa Cruz
UC Santa Cruz Electronic Theses and Dissertations

Title
High Temperature Experimental Characterization of Microscale Thermoelectric Effects

Permalink
https://escholarship.org/uc/item/1px4j71f

Author
Favaloro, Tela

Publication Date
2014

Copyright Information
This work is made available under the terms of a Creative Commons Attribution-NonCommercial-NoDerivatives License, availalbe at
https://creativecommons.org/licenses/by-nc-nd/4.0/

Peer reviewed|Thesis/dissertation

eScholarship.org Powered by the California Digital Library
University of California

UNIVERSITY OF CALIFONIA
SANTA CRUZ

HIGH TEMPERATURE EXPERIMENTAL CHARACTERIZATION OF MICROSCALE THERMOELECTRIC EFFECTS

A dissertation submitted in partial satisfaction
of the requirements for the degree of

DOCTOR OF PHILOSOPHY

in

ELECTRICAL ENGINEERING

by

Tela Favaloro

September 2014

The Dissertation of Tela Favaloro is approved:

____
Professor Ali Shakouri, Chair

____
Professor Joel Kubby

____
Professor Nobuhiko Kobayashi

____
Tyrus Miller
Vice Provost and Dean of Graduate Studies

Copyright © by

Tela Favaloro

2014

This work is licensed under a Creative Commons Attribution-

NonCommercial-NoDerivatives 4.0 International License

Table of Contents

List of Figures vi

List of Tables xiv

Nomenclature xv

Abstract xviii

Acknowledgements and Collaborations xxi

Chapter 1 Introduction 1

1.1 Applications of thermoelectric devices for energy conversion 1

1.2 Physical Effects 6

Seebeck Coefficient 6

Peltier Effect 8

Joule heating 9

1.3 Thermoelectric material properties governing efficiency 10

Thermoelectric module design 10

Material Figure of Merit 12

1.4 Advances in material synthesis 14

Interdependence of thermoelectric material properties 14

Material nanostructuring theory 16

1.5 Advanced materials in this work 18

III-V films with embedded nanostructures 18

Nitride superlattices 20

Nanostructured bulk Mg_2Si 21

Vanadium dioxide nanobeams 22

1.6 High temperature material characterization methodologies and scope of work 24

In-plane and cross-plane measurements 24

Thermoreflectance imaging microscopy 25

Transient Harman technique 27

High temperature considerations 28

Chapter 2 Characterization techniques for thermoelectric material and device properties 29

2.1 In-plane measurements 30

Van der Pauw method for electrical conductivity 30

Differential Seebeck coefficient measurement 33

Consolidation of in-plane measurements 39
2.2 Cross-plane measurements 41
3ω method for measurement of thermal conductivity 41
Extension to measurement of the cross-plane Seebeck coefficient 48
Chapter 3 Thermoreflectance Thermal Imaging 52
3.1 General Principle 53
4-bucket approach to thermal imaging: homodyne method 55
8-bucket technique: simultaneous imaging of Peltier and Joule 59
Transient thermal imaging: pulsed boxcar averaging 61
3.2 Applications of thermal mapping: Peltier and Joule surface thermal profiles for high temperature imaging 63
3.3 High temperature experimental calibration method 69
Room temperature calibration measurements 69
High temperature calibration methodology 72
Gold 79
Platinum 84
Aluminum 86
Equations governing temperature dependence and the effect of passivation 88
Chapter 4 Transient Harman technique for direct measurement of the cross-plane figure of merit of thin films at high temperatures 95
4.1 Theory and measurement requirements 96
4.2 Optimization of device design 98
4.3 Measurement Details and Results 103
Application of the transient Harman technique 103
Thermoreflectance imaging 107
High temperature experimental results and cross-plane Seebeck 109
4.4 Finite Element Modelling 114
Chapter 5 High magnification imaging of vanadium dioxide nanobeams 121
5.1 VO_2 material background information 121
5.2 Measurement Specifics 123
5.3 Measurement results: periodic domain organization 125
5.4 Measurement results: irregular domain configuration 129
5.5 Discussion 133
Chapter 6 Design and fabrication of high temperature vacuum thermostat 139

6.1 General Considerations 139
6.2 Bulk measurement stage 141
6.3 Chamber for optical measurement 144
Chapter 7 Conclusions 147
High temperature thermoreflectance imaging and transient Harman characterization of thermoelectric energy conversion devices 150
Characterization of the temperature dependence of the thermoreflectance coefficient for conductive thin films 151
Direct observation of nanoscale Peltier and Joule effects at metal-insulator domain walls in vanadium dioxide nanobeams 152
References 155

List of Figures

Figure 1.1: Radioisotope thermoelectric generator used by NASA to power the Curiosity Mars rover. Right hand side is a picture taken by the rover with RTG visible. 2

Figure 1.2: Energy flow diagram of a diesel engine equipped with a Bi_2Te_3 thermoelectric generator used for the recovery of waste heat. 3

Figure 1.3: An example of a biomass fueled advance stove featuring Bi_2Te_3 thermoelectric module, developed by Philip's Research. Picture taken from reference 18. 5

Figure 1.4: Schematic depicting the movement of charge carriers in response to a temperature gradient. The representative probability distributions (f(E)) governed by Fermi-Dirac statistics for the different temperatures experienced in the material. 7

Figure 1.5: Ohmic contact formed between a metal and an n-type semiconductor.. 9

Figure 1.6: Thermoelectric couple configured for energy generation. 11

Figure 1.7: The effect of nanostructuring on the density of states in the conduction band. 17

Figure1.8: High resolution SEM images of n-type and p-type III-V materials with embedded nanoparticles. 19

Figure 1.9: HfN/ScN superlattice with roughened interface. 21

Figure 1.10: Mg_2Si unit cell for an 'advanced' bulk thermoelectric material. 22

Figure 1.11: VO_2 nanobeam in the phase coexisting regime exhibiting periodic domain structure. Alternating Peltier cooling and heating signals occur at the interface between the metal and insulating phases in this material. 23

Figure 2.1: van der Pauw sample configurations. The left hand sample displays an optical image of the vdP clover leaf pattern. 31

Figure 2.2: Schematic of the side view of a sample mounted for in-plane measurement depicting the circuit used for the differential Seebeck measurement. 35

Figure 2.3: In-plane Seebeck coefficient measurement of thin film samples at approximately 650 K by the differential method. 36

Figure 2.4: (a) A top down view of the sample stage for simultaneous measurements of electrical conductivity and Seebeck coefficient of a sample with clover leaf vdP geometry. (b) The high temperature behavior of the Seebeck coefficients shows substrate contributions around 550 K. (c) Electrical conductivities of the films are displayed. 40

Figure 2.5: Experimental schematic/circuitry used for high temperature 3ω measurement.44

Figure 2.6: The characteristic 3ω curve for a simple case of a metal (gold) heater line deposited on a silicon substrate at 295 K. The thermal conductivity of silicon is determined to be 156 W/m-K, which matches well with reference values.' 46

Figure 2.7: High temperature thermal conductivity of a silicon substrate, attained by 3ω measurement using various metal heater line compositions, plotted in comparison to the data from references 42 and 43. 48

Figure 2.8 (a) Schematic of a superlattice device prepared for cross-plane Seebeck and thermal conductivity measurements. b) The measured 2ω Seebeck voltages in a device and reference sample generated in the thermoelectric superlattice layer plotted as a function of frequency.. 51

Figure 3.1: Basic experimental apparatus for high temperature thermoreflectance thermal imaging.. 54

Figure 3.2: Schematic describing the principles of the different thermoreflectance methodologies. 59

Figure 3.3: Transient thermoreflectance imaging of a 50 μm 0.2 % ErAs:InGaAs thermoelectric device. a) Comparison of transient data of the total temperature response in cooling mode at different locations on the device. b) Thermoreflectance images taken with long phase delay of the total temperature response and c) extracted Peltier cooling. 63

Figure 3.4: Comparison of thermal images of different device sizes in an early generation transient Harman device design. 64

Figure 3.5: Thermal images portraying the functionality of the modified 4-bucket method, (a), compared with thermal images produced by the conventional 4-bucket approach, (b), of a 25 μm 0.2 % ErAs:InGaAs energy conversion device.(c) The absolute values of the amplitudes of the respective temperature signals of the two techniques. d) Cross-sectional thermal profiles of Peltier images indicating current spreads preferably toward the edges of the mesa. 67

Figure 3.6: Schematic of the experimental set up for thermoreflectance coefficient calibration at room temperature. 71

Figure 3.7: Experimental apparatus for thermoreflectance imaging with simultaneous 3ω measurement. 73

Figure 3.8: a) Optical image of the sample with several heater designs for the different evaporated metals. b) Diagram of the sample cross-section; 74

Figure 3.9: The acquired amplitude of the temperature oscillations and the relative reflectivity of a gold heater line. 76

Figure 3.10: a) Optical greyscale images of the gold, aluminum and platinum heater lines in different areas on the same chip after experiencing temperatures above 800 K. b) SEM images in different locations on the gold heater line. 77

Figure 3.11: Experimentally measured C_{TR} for gold, aluminum and platinum displayed with respect to illumination wavelength. The spectral behavior of the coefficient is from literature, while the individual values are from this work.. 78

Figure 3.12: Peltier magnitude (a) and phase (b) images of the active gold heater line at room temperature. No 1st harmonic temperature signature is present in these images. 79

Figure 3.13: The change in the reflectivity of a gold heater line under 530 nm, 470 nm, and 455 nm illuminations, in response to temperature oscillations with amplitude 3.7 K. a) exhibits the optical images under the three wavelengths. b) and c) depict the magnitude and phase of *ΔR/R,* respectively. 81

Figure 3.14: The temperature trends of *ΔR/R* measured by thermoreflectance imaging and $\Delta T_{2\omega}$ calculated by 3ω method. 82

Figure 3.15: C_{TR} behavior with temperature for bare gold (a) and gold with a 200 nm thick layer of SiN_x (b). The maximum change in the coefficient is exhibited under 470 nm illumination; ~20 % over the temperature range, or approximately 0.20 x 10^{-4} per 100 K. .. 83

Figure 3.16: Thermal images of the platinum heater line at 700 K for $\Delta T_{2\omega}$ = 8.3 K. The phase images show that the sign of the thermoreflectance coefficient flips with passivation under 470 nm illumination. 85
Figure 3.17: C_{TR} of bare platinum (a) and passivated platinum (b) up to 800 K. 86
Figure 3.18: Comparison of the change in reflectivity due to Joule heating of 3.7 K at room temperature and 8.1 K at 600 K.. 87
Figure 3.19: The trend of the coefficient of thermoreflectance for bare and passivated aluminum. C_{TR} shifts at a rate of about 0.22 x 10^{-4} per 100 K temperature change for bare aluminum, which is quite substantial considering the small values of C_{TR}. 88
Figure 3.20: Schematic of the effect of a temperature increase on the physical processes in a bulk metal which can lead to modification of the optical properties. 90
Figure 3.21: The reflectivity of light of the different measurement wavelengths plotted as a function of passivation layer thickness. The grey line indicates the actual measured SiN_x thickness. 92
Figure 3.22: The thermoreflectance coefficients of platinum and gold under different illumination wavelengths plotted with respect to the passivation layer thickness.. 94

Figure 4.1: (a) Schematic of improved device design for thin-film transient Harman measurement. (b) Trade-off between heat leakage through the current injection lead and heat flow into the device due to Joule heating dissipated in the injection neck of a 25 µm thick 0.2 % ErAs: InGaAs film, plotted as a function of current injection neck width. 100

Figure 4.2: The measured voltage response of the thermoelectric energy conversion device to 100 mA bipolar excitation at select ambient temperatures. The positive and negative measured voltages are plotted such that time t =0 is taken as the device turn-off time. .. 104

Figure 4.3: The Peltier (a) and Joule (b) transient Seebeck voltages taken at various applied biases at room temperature for a 50 µm × 50 µm device. The insets display the total amplitude of the transient voltage signal plotted against input current. 107

Figure 4.4: Thermoreflectance imaging of the 50 µm × 50 µm device at room temperature taken at 100 mA bias, separated into Peltier and Joule components.. 109

Figure 4.5: Transient Seebeck voltages under ~100 mA excitation at different ambient temperatures, from room temperature to 550 K with 50 K temperature steps. (a) Peltier component of the Seebeck voltage. (b) Joule component of the Seebeck voltage. 111

Figure 4.6: (a) Peltier and Joule thermoreflectance images of the device at varying ambient temperatures: 300 K, 400 K, and 500 K. (b) Peltier and Joule temperature signals plotted versus ambient temperature; these values are averaged over the mesa. 112

Figure 4.7: Optical images of the device depicting surface degradation effects after experiencing 550K and 600 K ambient temperature. 113

Figure 4.8: Comparison of the measured Seebeck coefficient calculated in the cross-plane direction using the transient Harman technique in conjunction with thermoreflectance

imaging on a 25 µm thick 0.2 % ErAs:InGaAs film (red, closed circles) to that of a 2 µm thin-film measured in the in-plane direction (blue, open squares). 114

Figure 4.9 (a) Schematic depicting the correct current path, and the actual current path in the device (b) as determined by FEM analysis. 117

Figure 4.10: Direct comparison of the measured thermoreflectance images (a) and the finite element modeling results (b) for a 50 µm × 50 µm device in cooling mode.. 118

Figure 4.11: Comparison of the thermal profiles between simulation (dashed lines) and thermoreflectance experiment (open squares) in forward and reverse bias (cooling and heating modes). (a) Optical image of the 50 µm × 50 µm experimental device modeled by ANSYS 3D finite element simulation. Thermal profiles and simulation results at room temperature (b) and 450 K (c).. 119

Figure 5.1: Metal-insulator heterostructures along an individual VO_2 nanobeam. a) Optical images of a typical VO_2 NB upon heating from room temperature (I_{M1}) through coexisting domains (M_R and I_{M2}) to a fully metal M_R state. Scale bar represents 10 µm. b) The physical domains are identified by Raman spectroscopy. c) Band diagram for M and I_M phases. d) Heating and cooling electrical resistance as a function of temperature for NB_{type1}. 123

Figure 5.2 Thermoreflectance thermal images of NB_{type1}taken at 355K with 10µA applied current, after 500 cycles averaging. a),b) Optical images of the nanobeam and 'map' (greyscale). c), d) Peltier temperature magnitude and phase images, respectively. e), f) Joule temperature magnitude and phase images. 126

Figure 5.3: The Peltier a) and Joule b) thermal signals plotted with respect to location along NB_{type1}.. 128

Figure 5.4: Thermal images of non-periodic nanobeam (NB_{type2}) at 348K with 8μA current excitation, averaged for 500 cycles. a-e) Initial thermoreflectance measurement images of NB_{type2} before the RHS segment changed from M-I-M to M-I domain configuration. f-j) Thermal images for the same current bias taken after the RHS segment stabilized. 131

Figure 5.5: Resistance as a function of ambient temperature comparison of the two NBs. 134

Figure 5.6: 3-D plots of preferred domain wall orientations: θ=56˚ for M_R/I_{M1} (green) and θ=89˚ for M_R/I_{M2} (blue)... 135

Figure 5.7: The variation in the magnitudes of temperature for NB_{type2} with 8 μA applied at 348 K. NB_{type2} represented the worst case scenario as it displayed the greatest heating, especially in the RHS peak. 138

Figure 6.1: The bulk measurements chamber, viewed with vacuum lid off. Upper left depicts a diagram of the bulk measurement stage during the design phase. The right hand photo illustrates thermal isolation of the measurement region.. 143

Figure 6.2: Calibration data of the bulk measurement stage for 0.15 % Bi doped Mg_2Si pellets, in comparison with measurements of the same sample performed at JPL. (a) van der Pauw electrical conductivity and (b) In-plane Seebeck measurement calibration results... 144

Figure 6.3: Optical thermostat during high temperature thermal imaging and internal schematic of chamber components. 145

Figure 7.1: The periodic table of elements with color indicators of elemental abundance (scarcity) and the Herfindahl-Hirschman Index values (HHI) signifying market concentration (reserves) and geopolitical data (elemental production) which comprise supply risk......... 148

Figure 7.2: Comparison of the raw image buckets relative to the baseline reflectance (ΔR) of a VO_2 nanobeam (a) and a thermoelectric cooler (b) taken with the 8-bucket thermal imaging method.. 154

List of Tables

Table 3.1: Summary of the at room temperature thermoreflectance coefficients obtained at the specific illumination wavelengths utilized in this work. 78

Table 4.1. Summary of the 25 µm 0.2 % ErAs:InGaAs material parameters in the cross-plane direction determined by either direct measurement or through FEM simulation compared alongside the reported in-plane and 3ω values of a 2 µm thin-film of the same composition. 120

Nomenclature

a	lattice constant
A	area of a sample
A_C	area of contact
B_n	thermoreflectance imaging bins
c	speed of light in a vacuum
CCD	charge coupled device
C_h	volumetric heat capacity
C_R	tetragonal c-axis (nanobeam length)
C_{TR}	thermoreflectance coefficient
D_{Th}	thermal diffusivity
d	layer thickness
d_f	thickness of a thin film
d_C	contact thickness
DUT	device under test
e	fundamental charge of electron/hole
E	Energy
E_a	activation energy
E_C	Energy level of the conduction band edge
E_F	Fermi energy
E_V	Energy level of the valence band edge
F	Electric field
$f(E)$	Fermi-Dirac distribution function
FR_{CCD}	CCD frame rate
h	Planck's constant
h_{eff}	effective heat/current transfer coefficient
I	electric current
I_M	insulating monoclinic phase
J	electrical current density
K	thermal conductance: $\kappa A/L$
k_B	Boltzmann constant
k	optical extinction coefficient
L	length in the direction of current
L_C	characteristic length
L_P	thermal penetration depth
ʟ	Lorenz number
LHS	left hand side
M_R	metallic rutile/tetragonal phase
M-I	metal-insulator domains
MIT	metal insulating transition
n	integer counter
n_e	charge carrier concentration
$\boldsymbol{n}$	complex integer of refraction

NB	nanobeam
p_{Source}	generated volumetric power density
P	dissipated power
q	heat flux (rate of heat flow per unit area)
Q	heat flow
Q_{IN}	rate of input heat energy
Q_{L}	thermal power supplied to load
Q_{J}	Joule thermal power
Q_{P}	Peltier thermal power
r	amplitude of reflectance
R	electrical resistance
R_{C}	contact resistance
R_{DW}	domain wall resistance
R_{ext}	external resistance
R_{h}	heater line resistance
R_{hor}	electrical resistance in the horizontal direction
R_{INT}	internal resistance of thermoelement
R_{L}	load resistance
$R_{L,\eta}$	optimum load resistance for maximum efficiency
R_{Tot}	total electrical resistance
R_{S}	sheet resistance
R_{th}	thermal resistance
R_{ver}	electrical resistance in the vertical direction
RHS	right hand side
RTG	radioisotope thermoelectric generator
Ꞧ	reflectivity
$Ꞧ_{\mathrm{DC}}$	baseline reflectivity
S	Seebeck coefficient
s(t)	reflectivity signal
t	time
T	absolute temperature
TC	thermocouple
T_{C}	cold-side temperature
T_{H}	hot-side temperature
T_{MIT}	temperature of metal to insulating phase transition
V	voltage
V_{ABS}	material absolute Seebeck voltage
V_{meas}	measured voltage
V_{R}	resistive voltage
V_{S}	Seebeck voltage
V_{Source}	source output voltage
V_{SP}	Seebeck voltage induced by Peltier effect
V_{SJ}	Seebeck voltage induced by Joule heating
V_{T}	total voltage including both Seebeck voltage and ohmic voltage
V_{TC}	voltage generated in thermocouples

vdP	van der Pauw technique
w	width of a sample
x(T)	length fraction
ZT	thermoelectric figure of merit
α	temperature coefficient of resistance
α_{TH}	thermal expansion coefficient
β	phase change of reflected light
ΔT	temperature differential
ε	permittivity/complex dielectric constant
η	efficiency
η_{Max}	maximum conversion efficiency
κ	thermal conductivity
κ_{bulk}	thermal conductivity of substrate/bulk material
κ_f	thermal conductivity of thin film
λ	wavelength of incident light
σ	electrical conductivity
σ_d	differential electrical conductivity
σ_{eff}	effective electrical conductivity of the device
σ_f	electrical conductivity of a thin film
θ	angle
Π	Peltier coefficient
τ	thermal time constant
μ	charge carrier mobility
φ	phase delay of an AC signal
ϕ	phase difference of temperature oscillation
ω	frequency of an AC signal

Abstract

High Temperature Experimental Characterization of Microscale Thermoelectric Effects

By

Tela Favaloro

Thermoelectric devices have been employed for many years as a reliable energy conversion technology for applications ranging from the cooling of sensors or charge coupled devices to the direct conversion of heat into electricity for remote power generation. However, its relatively low conversion efficiency has limited the implementation of thermoelectric materials for large scale cooling and waste heat recovery applications. Recent advances in semiconductor growth technology have enabled the precise and selective engineering of material properties to improve the thermoelectric figure of merit and thus the efficiency of thermoelectric devices. Accurate characterization at the intended operational temperature of novel thermoelectric materials is a crucial component of the optimization process in order to fundamentally understand material behavior and evaluate performance.

The objective of this work is to provide the tools necessary to characterize high efficiency bulk and thin-film materials for thermoelectric energy conversion. The techniques developed here are not bound to specific material or devices, but can be generalized to any material system.

Thermoreflectance imaging microscopy has proven to be invaluable for device thermometry owing to its high spatial and temporal resolutions. It has been utilized in this work to create two-dimensional temperature profiles of thermoelectric devices during operation used for

performance analysis of novel materials, identification of defects, and visualization of high speed transients in a high-temperature imaging thermostat. We report the development of a high temperature imaging thermostat capable of high speed transient thermoelectric characterization. In addition, we present a noninvasive method for thermoreflectance coefficient calibration ideally suited for vacuum and thus high temperature employment. This is the first analysis of the thermoreflectance coefficient of commonly used metals at high-temperatures.

High temperature vacuum thermostats are designed and fabricated with optical imaging capability and interchangeable measurement stages for various electrical and thermoelectric characterizations. We demonstrate the simultaneous measurement of in-plane electrical conductivity and Seebeck coefficient of thin-film or bulk thermoelectric materials. Furthermore, we utilize high-speed circuitry to implement the transient Harman technique and directly determine the cross-plane figure of merit of thin film thermoelectric materials at high temperatures.

Transient measurements on thin film devices are subject to complications from the growth substrate, non-ideal contacts and other detrimental thermal and electrical effects. A strategy is presented for optimizing device geometry to mitigate the impact of these parasitics. This design enabled us to determine the cross-plane thermoelectric material properties in a single high temperature measurement of a 25µm InGaAs thin film with embedded ErAs (0.2%) nanoparticles using the bipolar transient Harman technique in conjunction with thermoreflectance thermal imaging. This approach eliminates discrepancies and potential device degradation from the multiple measurements necessary

to obtain individual material parameters. Finite element method simulations are used to analyze non-uniform current and temperature distributions over the device area and determine the three dimensional current path for accurate extraction of material properties from the thermal images. Results match with independent measurements of thermoelectric material properties for the same material composition, validating this approach.

We apply high magnification thermoreflectance imaging to create temperature maps of vanadium dioxide nanobeams and examine electro-thermal energy conversion along the nanobeam length. The metal to insulator transition of strongly correlated materials is subject to strong lattice coupling which brings about the unique one-dimensional alignment of metal-insulator domains along nanobeams. Many studies have investigated the effects of stress on the metal to insulator transition and hence the phase boundary, but few have directly examined the temperature profile across the metal-insulating interface. Here, thermoreflectance microscopy reveals the underlying behavior of single-crystalline VO_2 nanobeams in the phase coexisting regime. We directly observe highly localized alternating Peltier heating and cooling as well as Joule heating concentrated at the domain interfaces, indicating the significance of the domain walls and band offsets. Moreover, we are able to elucidate strain accumulation along the nanobeam and distinguish between two insulating phases of VO_2 through detection of the opposite polarity of their respective thermoreflectance coefficients.

Acknowledgements and Collaborations

There are many people to whom I owe recognition and gratitude for their contribution to this work:

- Quantum Electronics Group
  My advisor Professor Ali Shakouri for his patience and guidance, Amir Ziabari for his simulation work and overall great attitude, Je-Hyeong Bahk for the specialized device processing and Rajeev Singh with whom I worked on the development of the thermostats. Special thanks to James Christofferson and Zhixi Bian.

- UC Santa Barbara
  Hong Lu and Peter Burke for sample growth and fabrication

- UC Berkeley
  Joonki Suh-synthesis of VO_2 nanobeam samples and Joe Feser

- Discovery Park at Purdue University
  Polina Burmistrova, Pankaj Jha, Gautam Yadav, Jeremy Schroeder and Rob Wortman

- UC Davis
  Julia Zaikina and Tanghong Yi

- JPL –Sabah Bux

- Pennsylvania State University
  Yijia Gu and Long-Qing Chen

- My committee members Joel Kubby and Nobuhiko Kobayashi

- Dave Thayer, Darryl Smith and Joe Cox in the UCSC machine shop-you guys rock!

- My personal gratitude to Frances Ruiz-Wood and Bjorn Vermeersch and the advent of cookie time.

This work is dedicated to my mother, who worked almost as hard as I did to see me through…

Chapter 1 Introduction

1.1 Applications of thermoelectric devices for energy conversion

Thermoelectric devices have been employed for many years as a reliable energy conversion technology for applications ranging from localized hot spot cooling to waste heat recovery. These devices are utilized because of their solid-state attributes; they are compact and dependable for long term use in a variety of environments due to the absence of moving parts. However, the relatively low conversion efficiencies have limited the ubiquity of thermoelectric implementation to niche applications.

Since the early 1960s, NASA has been employing radioisotope thermoelectric generators (RTGs) for power generation in deep space and planetary missions which require a constant power supply (Figure 1.1).[1] Solar energy flux weakens and becomes insufficient for the energy requirements of deep space missions, and the long planetary/lunar nights necessitate energy storage capability. These thermoelectric modules directly convert the thermal energy produced during the natural decay of a radioisotope, commonly Plutonium 238 (^{238}Pu) into electrical power. In many of these devices, cogenerated heating is routed away from the module to control the temperature of critical system components while maintaining the cold side temperature.[1,2] The thermoelectric materials that comprise the modules are selected based on their conversion efficiencies in the operational ambient temperature; until recently, SiGe alloys achieved the highest conversion efficiency of ~7 % with a hot side temperature of 1300 K.[1-3] The radioisotope generators deployed by NASA have proven to be robust, exhibiting minimal degradation from environmental factors and

outlasting the intended mission length. The reduction in power output of the thermal source governs the overall lifespan of the generator. In spite of these beneficial qualities, the small heat to electrical power conversion efficiency and the material expense have prevented the use of this technology in terrestrial applications, excepting in small, remote locations.

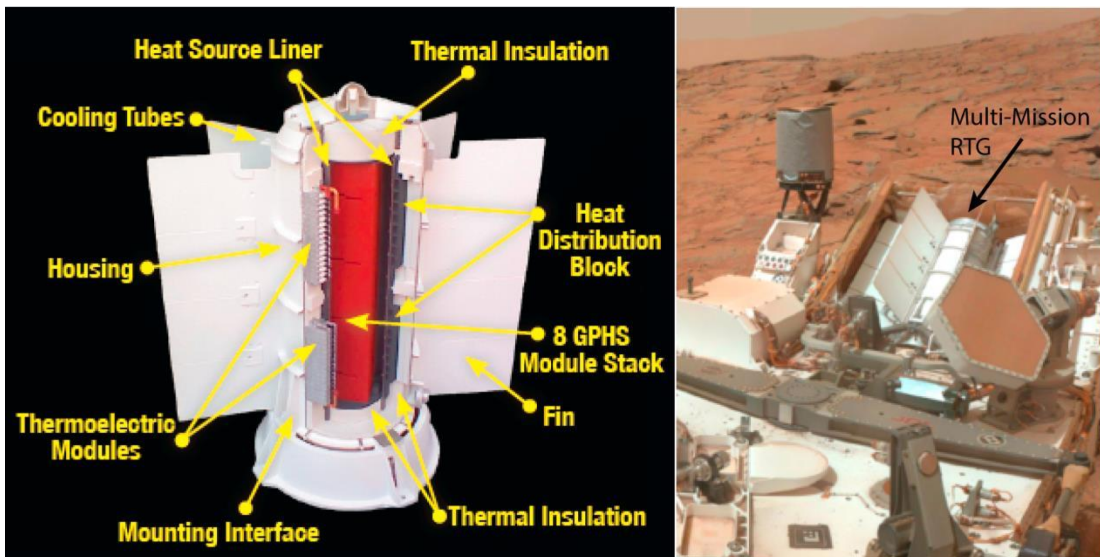

Figure 1.1: Radioisotope thermoelectric generator used by NASA to power the Curiosity Mars rover. Right hand side is a picture taken by the rover with RTG visible. (From Ref. [4]: http://mars.jpl.nasa.gov/msl/files/mep/MMRTG_FactSheet_update_10-2-13.pdf)

The automotive industry would significantly benefit from thermoelectric waste-heat reclamation and has already incorporated thermoelectric technology into some commercially available vehicles. [5] It is estimated that more than 75 % of the power generated in a traditional combustion engine vehicle is lost as heat through the vehicle exhaust, engine cooling lines, and other parasitic losses such as mechanical braking in the wheels.[5,6] For example, the average automobile exhaust produced during normal vehicle

operation is heated in the combustion cycle to temperatures in the range of 650 K to 900 K.[5-7] Refer to Figure 1.2 for an energy flow diagram of a vehicle equipped with a thermoelectric generator. Recently, Bi_2Te_3 thermoelectric generators demonstrated an improvement in fuel consumption of 2.5 % to 4 %, depending on operating conditions, when placed in-line with the vehicle exhaust.[8] This thermoelectric generator was implemented for maximum conversion efficiency; however, its potential impact was limited by the need to incorporate a thermal bypass to limit the temperature of the module to under 550 K and prevent material damage. Yet, the cost per Watt (electrical) generated would not make this thermoelectric generator economically viable. The study mentions cheaper materials able to withstand 900 K ambient temperatures could be economical. Nonetheless, some manufacturers have begun developing similar systems for integration into high-end models to improve overall efficiency.[8,9,10,11]

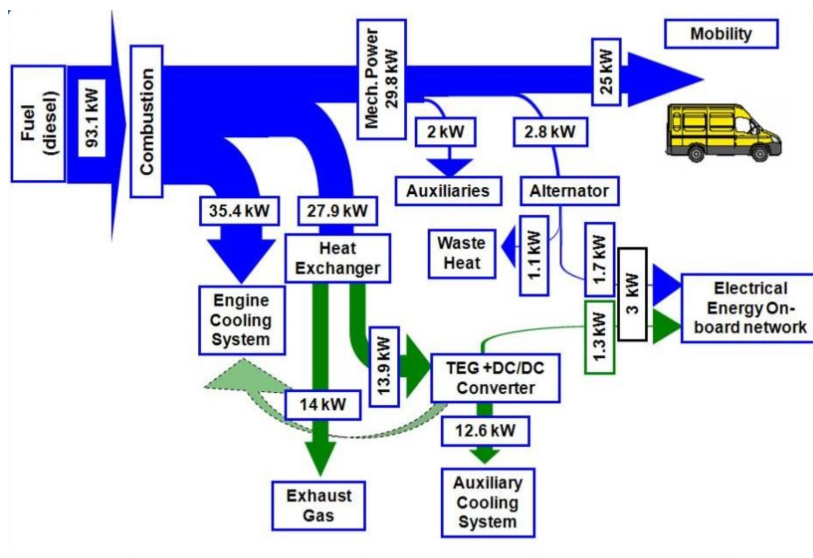

Figure 1.2: Energy flow diagram of a diesel engine equipped with a Bi_2Te_3 thermoelectric generator used for the recovery of waste heat. The efficiency of the thermoelectric generator and thermal efficiency of the heat exchanger among other factors contribute to

overall power (fuel) savings. (Image taken from HeatReCar project website: www.heatrecar.com)

Some non-profit organizations (and humanitarian research sectors of for-profit companies) have begun the development and in-field testing of advanced, biomass-fueled cooking stoves.[12,13,14] A large percentage of the population in developing countries, estimated at around three billion people in total,[15] relies on the combustion of wood or some other biomass for all their cooking and heating needs. This results in many instances of smoke inhalation-related illness (approximately 4.3 million deaths per year[15]) accompanying the substantial in-home air pollution and the overuse of limited natural resources. The new stove design incorporates a thermoelectric module that converts the heat generated in the stove to electrically power a fan. The resultant increased air flow within the stove improves the combustion efficiency; this, combined with other design improvements such as lower thermal mass materials and high environmental isolation also makes the fire burn hotter and thus more cleanly than traditional stoves. Some models preheat the secondary air to burn more completely,[12] while others harness the electricity to power a light[16] or charge a battery.[17] Overall, these stoves have demonstrated more than 90 % toxic emission reduction and around 50 % fuel savings.[18] Commercially available thermoelectric modules, namely bismuth telluride (Bi_2Te_3) are integrated in the stoves to keep costs relatively low (Figure 1.3). However, this material system is not optimal for the temperatures attained in these stoves, ~500 K to 700 K or higher and necessitates additional mechanisms to cool the module or thermal insulation. In addition, tellurium is a rare and toxic element, adding to

the expense. Utilization of more available and scalable materials for the thermoelectric generation will make this technology accessible in developing countries.

Figure 1.3: An example of a biomass fueled advance stove featuring Bi_2Te_3 thermoelectric module, developed by Philip's Research. Picture taken from reference 18.

In spite of these difficulties, the implementation of thermoelectric power generation via waste heat recovery is increasingly attractive; approximately sixty percent of energy consumed in the United States each year is lost as rejected heat.[19] If only 10 % of that amount is reclaimed as electrical power, thermoelectrically generated power could more than account for the residential electricity requirements each year. The technology is many years away from this level of prevalence, but it is progressing; recent advances in semiconductor material synthesis have enabled the selective engineering of material properties to improve the efficiency of energy conversion devices.[20,21,22] These novel materials are able to be optimized to target applications requiring specific operational temperatures, reduced costs, and/or increased performance. Precise characterization of the

anticipated environment is therefore essential to evaluate the behavior of these materials during the device development process.

In this chapter, we provide an overview of the physical mechanisms governing thermoelectric energy conversion and explain how nanostructuring is employed to tune select material properties. The advanced materials analyzed in this work are highlighted. We introduce and discuss the application of the individual characterization techniques implemented and adapted for high temperatures; this chapter sets the foundation for understanding the development of novel thermoelectric materials and the importance of their characterization.

1.2 Physical Effects

Thermoelectric devices exploit the physical relationship between heat and electrical current in suitable materials; though any conductive material will exhibit a finite thermoelectric response. A temperature gradient applied across a material will induce the diffusion of charge carriers away from the hot side as they absorb the higher kinetic energy. As the electric charges move through a material, they transport heat but also dissipate thermal energy back into the material lattice through collisions with ions, phonons, or other such quantized particles. The favorable interplay of these effects leads to a good thermoelectric material.

Seebeck Coefficient

The Seebeck effect describes the voltage developed across a solid state material by the diffusion of charged particles in response to a temperature gradient, as shown in Figure 1.4. It was first observed by Thomas Seebeck in 1821, when the needle on a compass deflected

when placed near a closed loop of two dissimilar metals, with junctions held at two different temperatures. The ensuing movement of charge carriers induced a magnetic field. The Seebeck effect is responsible for the conversion of thermal energy to electricity in thermoelectric power generation devices, though most commonly it provides the functionality for thermocouple-based thermometry.

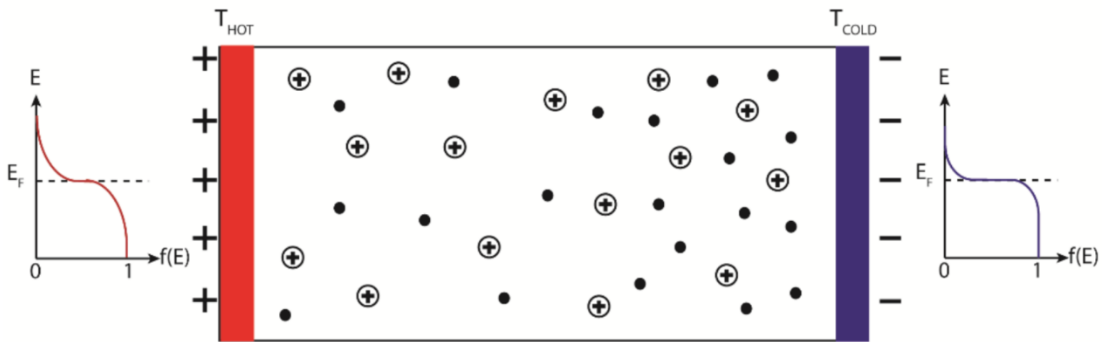

Figure 1.4: Schematic depicting the movement of charge carriers in response to a temperature gradient. In this example, the material is n-type and electrons are representing by closed black dots. The representative probability distributions (f(E)) governed by Fermi-Dirac statistics for the different temperatures experienced in the material.

The Seebeck coefficient, *S*, defines the relationship between the Seebeck voltage (V_S) generated from a given temperature differential, for a given material:

$$V_S = \int S(T)dT.$$

Fundamentally, the Seebeck coefficient is a measure of the temperature dependence of the rate of change in the Fermi level in a solid. In the first order approximation, that is, for a small temperature change, the Seebeck coefficient is constant with temperature and the voltage produced has a linear dependence with temperature change. Common convention

designates the sign of S relative to the cold side: if the hot side of the material accumulates positive charge then S is negative. In many metals, the Seebeck coefficient is quite small, ~ 10 µV/K; whereas semiconductors can exhibit much higher coefficients on the order of many 100 µV/K.

Peltier Effect

Jean Peltier discovered the complementary effect thirteen years later; heating or cooling occurs at the junction of dissimilar materials when under electrical bias. The rate at which heat is created or absorbed is proportional to the applied current through the difference in the Peltier coefficients of the materials (denoted A and B) forming the junction:

$$Q = (\Pi_B - \Pi_A)I$$

In the example provided in Figure 1.5, material A is a metal forming an ohmic contact with material B, an n-type semiconductor. When the two materials are brought into close contact, the more energetic charge carriers in the metal tunnel into the semiconductor; the result is the subsequent alignment of the Fermi levels in the two materials. Thus, in order for current to flow through the junction, charge carriers from the metal must gain energy from the lattice to reach the conduction band in the semiconductor. The junction is therefore cooled by a factor equal to the difference in energy between the conduction band and the Fermi level in the metal (plus the average kinetic energy). Likewise, charge carriers moving from the semiconductor release energy when moving across the interface and heat the junction. This effect is the basis for Peltier cooling modules and thermoelectric heat pumps.

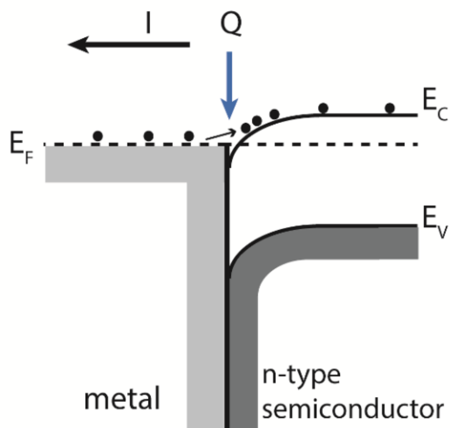

Figure 1.5: Ohmic contact formed between a metal and an n-type semiconductor. For the direction of current depicted here, the junction is cooled by electron flow.

The Peltier coefficient is really a measure of the amount of heat carried per unit charge in a material (relative to its Fermi level) and is expressed with the units W/A. Lord Kelvin (Thomson) established the interdependency between the Peltier coefficient and the Seebeck effect:

$$\Pi_B - \Pi_A = (S_B - S_A)T$$

where T is the absolute temperature. This relationship states that the observed heating/cooling of the interface of two dissimilar materials occurs at the junction of two materials with different *S*; the Seebeck effect is the driving force behind the different thermoelectric phenomena.

Joule heating

While the previously described effects are all reversible, a finite amount of thermal energy is irreversibly lost due to the resistivity of the material. This occurs in any electronic

transport process and is not a thermoelectric effect, though the resultant heating in a material affects thermoelectric performance. The heat dissipated (Q_J) is proportional to the square of the applied current, and is independent of current direction.

$$Q_J = I^2 R$$

where R is the electrical resistance of the material.

1.3 Thermoelectric material properties governing efficiency

Thermoelectric module design

The thermoelectric modules used for energy conversion, briefly described in section 1 of this chapter, consist of arrays of thermoelements connected across an external load. For maximum benefit, these thermoelements are comprised of alternating n-type and p-type legs connected electrically in series and thermally in parallel, refer to Figure 1.6 for a diagram of one of these elements. Ohmic metal contacts connect the materials electrically, while an electrically insulating heat sink creates the parallel thermal circuit. The resultant current flow is generated from the sum of the Seebeck voltages developed across the two legs in response to the temperature gradient; thus, accomplishing useful electrical work. Matching the load resistance (R_L) to the internal resistance (R_{INT}) of the module achieves maximum power output.

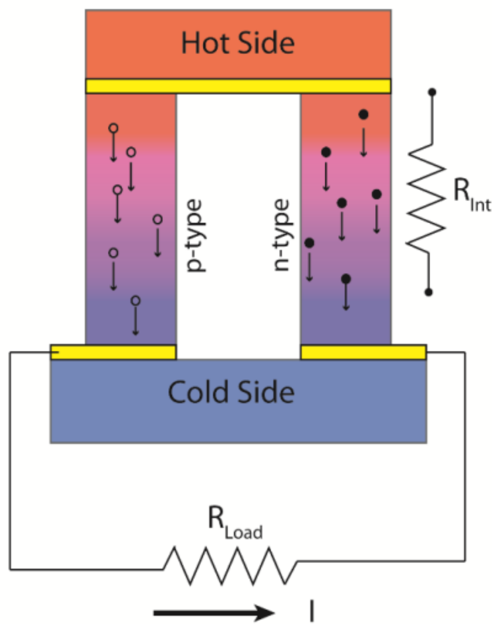

Figure 1.6: Thermoelectric couple configured for energy generation.

The interface described in Figure 1.5 exemplifies thermoelectric heat pumping capabilities. If the thermoelement is run in reverse, that is, if a current is applied to the device, heat will be absorbed at one junction, transported across the thermoelectric legs, and released to the heat sink. The interface that experiences active cooling can be exchanged if the current is reversed.

Interestingly, the materials selected and their respective geometries for the individual elements are not required to be homogenous. For example, NASA (and collaborators) incorporates segmented couples as part of the thermoelectric modules for the RTGs. The MMRTG (multi-mission RTG) features this design to power the Curiosity mars rover, both during transit and after reaching Mars.[3,4] The p-type leg is segmented with multiple advanced bulk materials to accommodate the variation in operational conditions; the

material optimized for higher temperature conversion is positioned closest to the heat source. In this way, an array of materials can be employed across the temperature gradient, each harnessed at their corresponding optimal temperature.

Material Figure of Merit

The maximum theoretical efficiency of a thermoelectric device is governed by a combination of material parameters which, together, comprise the material figure of merit ZT:

$$ZT = \frac{\sigma S^2}{\kappa} T.$$

In this equation, *S* is the Seebeck coefficient, *σ* is the electrical conductivity, *κ* is the thermal conductivity of the material, and *T* is the absolute temperature. The importance of this quantity becomes apparent through examination of the thermoelectric module depicted in Figure 1.6. Thermal isolation must occur between the two sides of the device; ideally, heat transport manifests as energy supporting charge accumulation but does not propagate through the lattice. Thus, the materials used as the elements should exhibit a small thermal conductivity, while supporting charge carrier flow through a large electrical conductivity. The Seebeck coefficient is the most important quantity; it controls the amplitude of the voltage developed for a given temperature differential and clearly should be maximized to achieve electrical power through a load.

The efficiency (*η*) of an energy conversion device is defined as the ratio of electrical energy supplied to the load, Q_L, relative to heat energy absorbed at the hot junction:

$$\eta = \frac{Q_L}{Q_{IN}} = \frac{I^2 R_L}{STI + K\Delta T - ½ I^2 R_{INT}}.$$

K is defined as the thermal conductance, where $\kappa = {K \cdot L}/{A}$ and L is the length of the element and A is the area. The energy entering the thermoelectric module from the hot side (Q_{IN}) is composed of Peltier heating at the interface, heat conducted into the device, and Joule dissipation. The generated Seebeck voltage induces current across the total resistance (R_{Tot}) of the circuit:

$$I = \frac{V_S}{R_{Tot}} = \frac{S\Delta T}{R_{INT} + R_L}.$$

R_{INT} is the effective resistance derived from the electrical conductivities in both legs of the thermoelement: $\sigma = {L}/{R_{INT}A}$. Neither of these geometries necessarily needs to equal the corresponding value across the two material types.

The expression for efficiency can be maximized with respect to the load resistance, giving:

$$\eta_{Max} = \frac{\Delta T}{T_H}\frac{\sqrt{1+ZT}-1}{\sqrt{1+ZT}+\frac{T_C}{T_H}}.$$

The optimum load resistance, $R_{L,\eta}$, for maximum efficiency differs from the matching load condition for maximum power generation:

$$R_{L,\eta} = \sqrt{1+ZT}\,R_{INT}$$

In these expressions, ΔT is the difference between the hot side and cold side temperatures, $\Delta T = T_H - T_C$ and T is approximated as the average temperature ½ΔT. The efficiency approaches the Carnot limit as ZT approaches infinity.

1.4 Advances in material synthesis

For many years, the maximum achievable material figure of merit was that of a Bi_2Te_3 alloy: ZT ~1, which explains its prevalence in commercial thermoelectric modules. This limit was reached due to the impediment of minimizing thermal conductivity without a corresponding sacrifice in electrical conduction. Atomic substitutions into the crystal lattice inhibit phonon propagation in the material; though, too many inclusions substantially disrupt the lattice structure resulting in significant loss of charge carrier mobility. Generally, the material parameters that constitute the thermoelectric figure of merit themselves are interdependent. It was not until 1993 that Hicks and Dresselhaus[23] proposed the idea that thermoelectric material properties can be engineered discretely at the nanoscale level by introducing complex structures and composites associated with thin-film growth.

Interdependence of thermoelectric material properties

Thermal conductivity (κ) is a measure of the ease of thermal energy propagation through a material, expressed in units of W/m·K. It is composed of two factors: a term representing the contribution of lattice vibrations (phonons) and an electronic component from heat transported by the charge carriers themselves. Charge carriers gain kinetic energy through collisions with the lattice and their subsequent higher energies cause them to diffuse to cooler areas. Further scattering imparts heat back into the lattice.

Electrical conductivity (σ) quantifies charge carrier movement in response to an electric field; this expression describes the concentration (n_e) and mobility (μ) of the charge carriers in a material:

$$\sigma = en_e\mu$$

where e is the fundamental charge of the electron/hole. In this work, σ is given in units: $(\Omega\cdot\text{cm})^{-1}$.

The relationship between thermal and electrical conductivities in metals or degenerate, bulk semiconductors is expressed by the Wiedemann-Franz law:

$$\frac{\kappa}{\sigma} = \text{L}T.$$

This expression states that the ratio of conductivities is proportional to ambient temperature through the Lorenz number, where $\text{L} = \pi^2 k_B^2 / 3e^2$, a constant. Thus, it is difficult to vary one parameter without affecting the other.

In semiconductor materials, the lattice contribution dominates the total thermal conductivity, though an increase in carrier concentration may induce a corresponding increase in thermal conductivity, depending on the mechanism introduced. The overall impact of thermal conductivity in these materials is less consequential at high temperatures; κ declines as a result of the increased phonon population while σ in most cases increases due to the thermal activation of intrinsic carriers.

There is also inherent connection between the Seebeck coefficient and electrical conductivity, which adversely affects ZT enhancement. The Fermi level of a bulk, n-type semiconductor, for example, shifts away from the band gap and into the conduction band with an increase in carrier concentration. Here, the density of states is more symmetric around the Fermi level; thus, the energy of charge carriers available to contribute to conduction is not optimal. As mentioned earlier, the Seebeck coefficient is a measure of

thermal energy transported per charge carrier, and can be expressed in terms of carrier energy as:

$$S = \frac{1}{eT}\frac{\int \sigma_d(E)(E - E_F)dE}{\int \sigma_d(E)\, dE}.$$

The term $\sigma_d(E)$ represents the effective electrical conductivity contributed by charge carriers at a given energy level. The total electrical conductivity is then the sum of these contributions over all energy levels. In summary, there is an optimal carrier concentration that balances asymmetry in σ_d (with respect to the Fermi level) while maintaining relatively high total electrical conductivity in bulk semiconductors.

Material nanostructuring theory

The most straightforward approach to improve the material figure of merit is by reducing the thermal conductivity through nanostructuring. This tactic has, by far, yielded the best results; by shrinking device dimensions to the order of the mean-free-path of the phonons, thermal energy propagation through the lattice is inhibited. In alloys, the differences in mass experienced along the lattice behave as atomic scale defects. This primarily affects shorter wavelength phonons. Whereas, interfacial or boundary scattering in superlattices and nanowires (2D and 1D structures) have demonstrated decreased κ to values well below the alloy limit of their respective bulk materials.[20-22] These interfaces are distributed or roughened to increase the scattering rate of phonons with mid to long wavelengths. Distributed nanoparticles or grain boundaries in nanocomposites also effectively disrupt phonons at selected wavelengths; the sizes of the inclusions can be controlled to target mid and/or longer wavelength phonons. The additional scattering of higher energy phonons still

occurs in these materials via atomic substitutions or defects. Thus, the lattice component of the thermal conductivity is minimized with little effect on charge carriers.

As mentioned in the previous section, asymmetry in the available states proximate to the Fermi level in a semiconductor material is necessary for a large Seebeck coefficient. Hicks and Dresselhaus proposed that quantum confinement has a dramatic effect on the density of states in a semiconductor material, which was subsequently verified.[24,25] These sharp features, illustrated in Figure 1.7, can be exploited by aligning the Fermi energy appropriately through careful selection of doping concentration (among other factors). This approach does not necessitate a decrease in carrier concentration; consequently σ can be enhanced along with S.

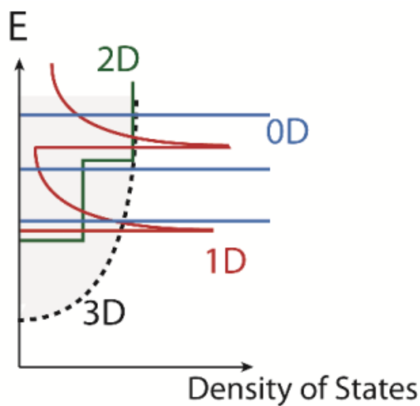

Figure 1.7: The effect of nanostructuring on the density of states in the conduction band.

Alternatively, nanostructures can be implemented as energy barriers for carrier filtering. Hot charge carriers, those with higher kinetic energies, are allowed to transmit over a potential barrier formed in the path of the current flow. In this way, higher energy carriers are

favored thus increasing the average heat transported per particle, i.e. the Seebeck coefficient. There is a corresponding decrease in electrical conductivity. Zide *et al*. experimentally observed electron filtering in nanostructured InGaAs films with InGaAlAs barriers[26] and again in a bulk-like nanocomposite of the same material system[27]. The authors achieved a dramatic increase in *S*, resulting in ZT > 1.3 at 800 K. These materials are used as a basis for characterization in much of this work.

These and many other thermoelectric material systems not mentioned here, validate the premise behind material nanostructuring and exhibit enhancement to the thermoelectric figure of merit. However, in many cases, the mechanisms responsible for the resultant improvements were unanticipated and/or the experimental results were not reproducible, indicating the need for ongoing material characterization. Nevertheless, the potential for more efficient thermoelectric devices has certainly been demonstrated.

1.5 Advanced materials in this work

III-V films with embedded nanostructures

The primary material system analyzed over the course of this work consists of InGaAs thin films with randomly distributed nanoparticles at varying atomic percentages. For higher efficiency n-type thermoelectric materials, erbium is co-deposited during the epitaxial growth of n-type $In_{0.53}Ga_{0.47}As$ semiconductor matrix which spontaneously yields rocksalt structured ErAs nanoinclusions. The resultant nanoparticles are a few nanometers in diameter and are naturally randomly dispersed in the film. Refer to Figure 1.8 for a high resolution image of this material with TbAs embedded nanoparticles. These materials have shown significant improvement in the thermoelectric power factor ($S^2\sigma$) through electron

filtering, while ErAs nanoparticles acting as dopants donate electrons to the matrix. Additionally, long wavelength phonons are scattered by the nanoparticles; higher atomic percentages of ErAs result in greater reduction of the lattice thermal conductivity. 0.2 % ErAs seems to be the most promising concentration, though this and 0.78 % TbAs nanoinclusions have consistently demonstrated ZT >1 at elevated temperatures.

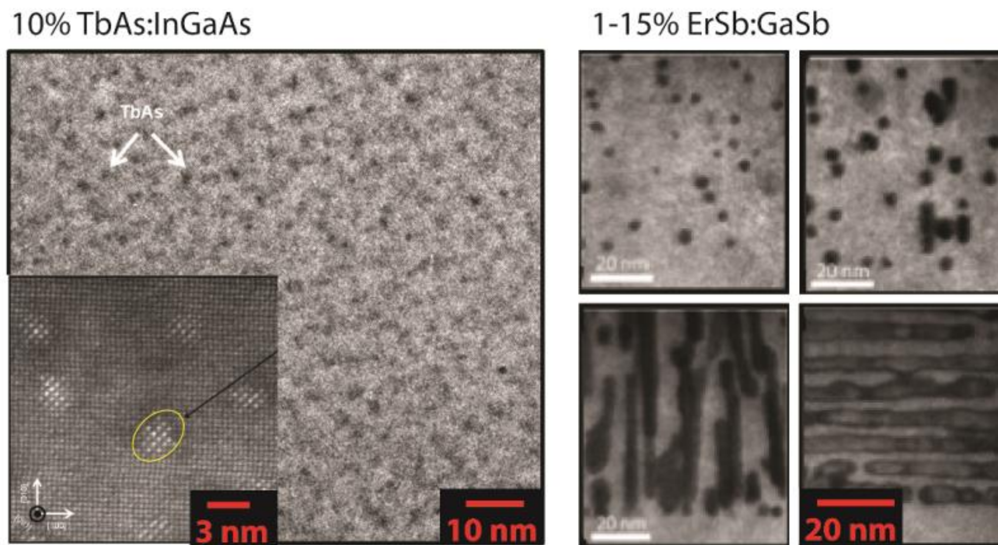

Figure1.8: High resolution SEM images of n-type and p-type III-V materials with embedded nanoparticles. As the the atomic percentage of the nanoparticles (ErSb) increases in the GaSb lattice, the nanoinclusions grow to form vertical 1-D structures at 10 % ErSb concentration and horizontal 1-D structures at 15 %.

Recently, we began investigating InGaSb with ErSb inclusions for the complementary p-type material. This material system is quite interesting; the self-assembled nanoparticles increase in size to eventually form 1-D nanowires with increasing InSb composition, shown in Figure 1.8. As with the n-type material, the nanoinclusions significantly hinder phonon transport. Beryllium co-doping and contributions from ErSb significantly increases electrical

conductivity and instigates metallic behavior in the charge carriers. Thus far, this material has displayed around a 25 % enhancement to ZT at 500 K for 0.8 % ErSb: $In_{0.69}Ga_{0.31}Sb$.

These two materials together are suitable for moderate temperature power generation applications. However, the method of growth and associated crystalline quality with long growth times will constrain their use to applications where high efficiency energy conversion is a more important factor than cost.

Nitride superlattices

Nitride superlattices are a potential material system for high temperature applications. Rocksalt nitrides are good refractory materials; they remain physically and chemically stable at temperatures beyond that of typical thermoelectric materials. The superlattices are formed with alternating metal/semiconductor periods with rough coherent interfaces, see Figure 1.9. We examined ScN as the semiconductor component for use with ZrN, HfN, and other metal alloys. Ideally, Schottky barriers are formed at the metal/semiconductor interfaces which filter out low energy electrons. Experiments have shown that the heterostructures produce a large increase in S while suppressing lattice thermal conductivity in the cross-plane direction, as compared to the individual bulk materials. The electrical conductivity exhibits a semiconductor-like increase with ambient temperature, though the values are too low to be utilized as a good thermoelectric material. This material system has not yet been optimized; tuning of the barrier height is possible through material alloying and by adjusting the superlattice period thickness. Simulations have shown very large ZTs are possible.[28]

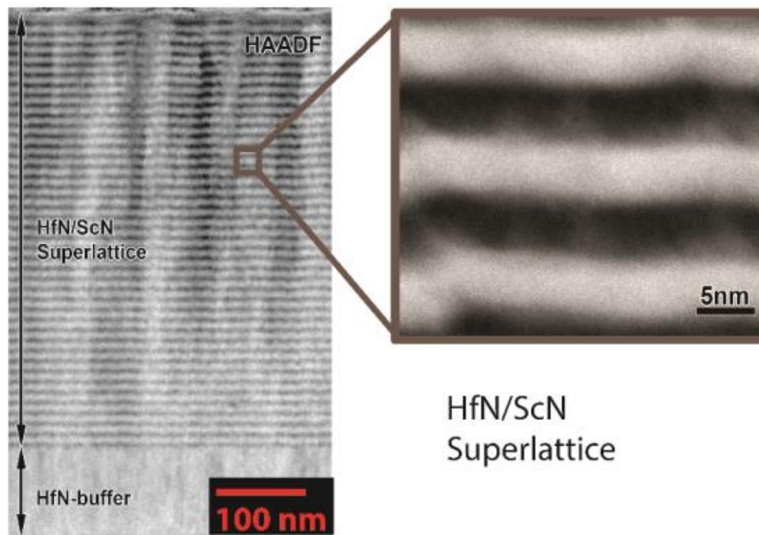

Figure 1.9: HfN/ScN superlattice with roughened interface.

Nanostructured bulk Mg_2Si

Advanced bulk materials have the best potential for scalability and thus are feasible for widespread use. Magnesium Silicide exhibits 'electron crystal, phonon glass' behavior in its Zintl phase, desired for high thermoelectric efficiency. In addition, its constituent materials are abundant and non-toxic. We specifically explored optimization of this material system through nanostructuring for conversion of waste exhaust heat in automobiles. Bismuth dopants are integrated into the light elemental framework typical of Zintl phase materials which maintains high charge carrier mobility and density, while the larger magnesium atoms scatter high energy phonons. Figure 1.10 illustrates the unit cell of the material. Silicon nanoparticles are incorporated to suppress mid to long wavelength phonon modes. High energy ball milling and spark plasma sintering are utilized for material synthesis of Mg_2Si with Si nanostructures. These techniques are similar to those already in use for Bi_2Te_3

commercial production. SEM images (Figure 1.10) show silicon aggregates form within the Mg_2Si framework; though, more distributed, smaller nanoparticles are ideal. Presently, the experimentally measured ZT is ~0.7 at 775 K, which is attractive, considering the limited temperature range of Bi_2Te_3. This material is also well-suited for thermoelectric power generation in the aforementioned stove application.

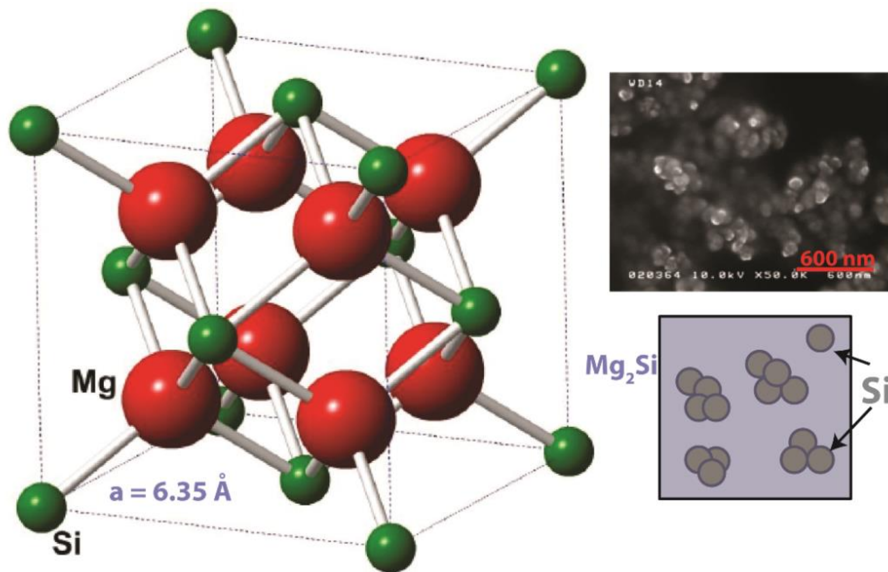

Figure 1.10: Mg_2Si unit cell for an 'advanced' bulk thermoelectric material. SEM image showing formed aggregates instead of the preferred nanoparticles.

Vanadium dioxide nanobeams

Strongly correlated materials share a unique feature where phase transitions result in significant changes in physical properties, making these materials of particular interest for their potential device applications beyond the scope of current semiconductor technologies. Such devices are inherently complicated in nature owing to strong coupling of the crystal lattice with charge, spin, and orbital degrees of freedom of electrons. The metal to insulator

transition (MIT) in VO_2 nanobeams, in particular, is subject to strong lattice coupling which brings about the unique one-dimensional alignment of metal-insulator (M-I) domains. Figure 1.11 shows the nanobeam in the domain coexisting state, along with the Peltier thermal images. Many studies have investigated the effects of stress on the MIT and hence the phase boundary, but few have directly examined the temperature profile across the metal-insulating interface. In this work, we utilize thermoreflectance microscopy to create two-dimensional temperature maps of single-crystalline VO_2 nanobeams under external bias in the phase coexisting regime. The incentive for this work is strictly scientific. These materials are investigated to reveal the underlying physics of the phase boundary; we directly observe highly localized alternating Peltier heating and cooling as well as concentrated Joule heating.

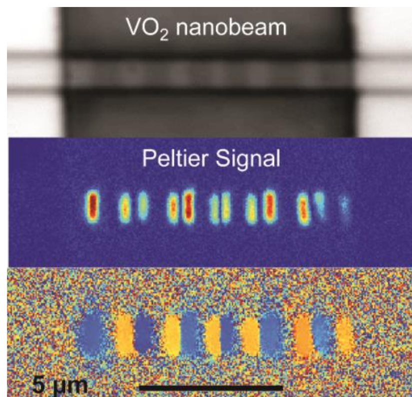

Figure 1.11: VO_2 nanobeam in the phase coexisting regime exhibiting periodic domain structure. Alternating Peltier cooling and heating signals occur at the interface between the metal and insulating phases in this material.

1.6 High temperature material characterization methodologies and scope of work

Optimization of novel thermoelectric materials is an iterative process: theories are given and implemented, measurements are performed whose results inform simulations, and theories are successively revised. Accurate characterization is a crucial part of this process and maintaining this precision in measurements subject to varying environmental conditions is essential to fundamentally understand material/device attributes in the operational range of interest. In many instances, new or alternative device functionality is revealed, or in some cases, performance-limiting defects. Examples of both of these outcomes have occurred over the course of this work and are discussed in this manuscript.

The work performed as part of this thesis is devoted to providing the tools necessary to identify and implement high efficiency materials for thermoelectric energy conversion which can impact the consumption of limited natural resources. The techniques described here are not bound to specific materials or devices, but can be generalized for any material system; however, some measurements impose specific requirements on device structures.

In-plane and cross-plane measurements

Chapter 2 is divided into the in-plane and cross-plane measurements commonly utilized in the characterization of thermoelectric materials. Regarding the in-plane measurements, we present a differential approach to determine the Seebeck coefficient and the van der Pauw method for electrical conductivity. The Seebeck coefficient is obtained by imposing a temperature gradient across the sample and measuring the resultant voltage and the temperature gradient with the same probes. S is simply the ratio of these values. The van

der Pauw technique is well established in semiconductor industry since it is immensely versatile when it comes to sample geometry restrictions. We discuss how these two measurements can be performed in a vacuum thermostat for high temperature characterization with one setup; thus, the power factor can be determined in a single measurement.

We introduce the 3ω measurement of cross-plane thermal conductivity and its extension for the cross-plane Seebeck coefficient in the second portion of chapter 2. The 3ω measurement is an electrical measurement of temperature in a heater line in response to AC electrical bias. Current or voltage excitation is applied at frequency 1ω and generates Joule heating in the heater line which spreads into the substrate at 2ω. Lock-in detection of the 3ω voltage across the heater line can determine the amplitude of the temperature oscillations. Thermal conductivity is the temperature response in the material bulk to electrical power dissipated in the heater line, as measured in the heater line. If the sample under test is thermoelectric in nature, then Joule heating creates a Seebeck voltage which also oscillates at 2ω. The magnitude of the Seebeck voltage divided by the 2ω temperature oscillation is the cross-plane Seebeck coefficient.

Thermoreflectance imaging microscopy

Thermoreflectance thermal imaging has proven to be a valuable tool for the thermometry of integrated circuits and other semiconductor/electronic devices, owing to its high spatial and temporal resolutions (~200 nm and 50 ns, respectively). This noncontact technique is based upon the detection of fluctuations in sample surface reflectivity ($\Delta R/R$) due to a variance in local surface temperature (ΔT). For most materials, the relationship is linear over a specified

temperature range. This dependency is quantified by the thermoreflectance coefficient, C_{TR}, which is normally on the order of 10^{-5} to 10^{-3} per (degree) K.

$$\frac{\Delta \mathrm{R}}{\mathrm{R}} = \left(\frac{1}{\mathrm{R}}\frac{\partial \mathrm{R}}{\partial T}\right)\Delta T = C_{TR}\Delta T.$$

If the C_{TR} is known, the absolute temperature change can be discerned. The coefficient is a sample composition and illumination wavelength dependent parameter, but is also strongly influenced by the measurement apparatus, especially the magnification and numerical aperture (NA) of the optics. It therefore must be calibrated for in each measurement.

Thermal imaging has been employed to create two-dimensional temperature profiles of device surfaces used for performance analysis of novel thermoelectric materials, reliability and failure point testing, and visualization of high-speed thermal transients.[29] It is especially constructive for the development and optimization of novel thermoelectric materials; Peltier and Joule temperature signatures are readily distinguished. However, CCD based thermal imaging at high ambient temperatures has not yet been realized. High temperature thermoreflectance thermal imaging enables the study of active devices at their intended temperatures of operation; and also provides real time device failure analysis upon temperature cycling.

Chapter 3 introduces the different approaches for thermoreflectance thermal imaging and describes the development and implementation of a high temperature thermoreflectance imaging apparatus. We present instances of high temperature thermal imaging of novel thermoelectric films which ascribes to the utility of the technique. Moreover, we report a

noninvasive method for thermoreflectance coefficient calibration ideally suited for in-chamber, and thus high temperature, employment.

In chapter 4, we utilize thermal imaging in conjunction with the transient Harman method at high temperature to quantify Peltier temperature and thus obtain cross-plane S. Thermal profiles are measured and used to diagnose device faults in an energy conversion device.

Furthermore, in chapter 5 we examine a study where high magnification imaging is used to analyze thermoelectric energy exchange and Joule heating at domain walls in vanadium dioxide nanobeams-revealing the stress response of correlated nanobeams. The small temperature signals associated with the M-I junctions (both spatially and in magnitude) warrant long averaging times of a very sensitive and volatile device. Strategies pertaining to successful imaging of such devices are discussed. In addition, we report that the relative thermoreflectance coefficients can readily distinguish between insulating states along the nanobeam.

Transient Harman technique

The methodology of the transient Harman method exploits the slower response time of thermally induced voltages to directly determine the cross-plane ZT of a thermoelectric device. In steady state, a voltage potential is developed across the sample comprised of electrical and thermal constituents. At device turn-off, the resistive component of the total voltage disappears instantaneously, while the generated Seebeck voltage will decay in accordance with thermal time constants. The material ZT is simply the ratio of these two voltages.

In practice, this measurement is difficult to implement in thin films; micro and nano-scale devices are subject to various electrical and thermal parasitic effects that can dominate overall performance. In chapter 4, we present an optimized design and specialized processing of experimental devices to mitigate these effects during the measurement of thermoelectric thin films. With this approach, we successfully employ the bipolar transient Harman method combined with thermoreflectance imaging to determine the individual cross-plane material properties (and ZT) for a microscale energy conversion device at elevated temperatures. This tactic eliminates discrepancies and potential device degradation from the multiple measurements necessary to obtain individual material parameters. Finite element method simulations are utilized to analyze surface current and temperature distributions over the device area to ascertain the three-dimensional current path. This is necessary to accomplish the accurate extraction of material properties from the thermal images, in spite of the detrimental impact of defective device processing.

High temperature considerations

The goal of this work is to facilitate the characterization of novel thermoelectric materials in their intended operational temperature range. All characterization techniques are presented in the context of their high temperature ease of use. Electrical and thermal degradation to the device under test is alleviated by the high vacuum environment; on the other hand, parasitic thermal gradients and thermal shunting are potentially intensified. General considerations for high temperature characterization are discussed in Chapter 6. We describe the fabrication of two custom thermostats, in addition to the respective measurement specifics.

Chapter 2 Characterization techniques for thermoelectric material and device properties

In this chapter, the detailed methodology of the standard measurement techniques for thermoelectric material characterization is presented. Each method requires specific measurement conditions for the extraction of an individual thermoelectric parameter, thus three measurements are necessary to construct the material figure of merit. This approach may introduce some discrepancies in the results; often material parameters vary among samples with different processing and film thicknesses, for example, the inclusion of buffer layers and growth substrate will contribute to the measured quantity. In addition, each high temperature run has the potential for device degradation, detrimental to subsequent measurements.

Here, we discuss techniques for combining individual measurements to reduce error introduced by repeated and/or dissimilar experiments. This approach is particularly useful in experiments with limited sample accessibility, such as in a vacuum cryostat. Since techniques are electrical in nature, only measurements with similar excitation bias (AC vs DC) and direction of applied current are amenable to consolidation. Simultaneous in-plane measurements of electrical conductivity and the Seebeck coefficient, and thus the power factor, are accomplished using the van der Pauw method with a differential Seebeck measurement, respectively. The 3ω technique, however, utilizes the frequency response to AC excitation of Joule heating in a heater line to determine cross-plane thermal conductivity of bulk and thin films. This method has been extended to measure the cross-plane Seebeck coefficient as well.

These experiments are designed and performed at high temperatures with careful consideration of the direct electrical probing of the samples. The thermoelectric devices examined in this section consist of both nanostructured thin films and bulk materials, and distinctions between the respective measurement configurations are identified. In the case of a distributed nanostructured system, such as embedded nanoparticles, the direction of measurement usually does not matter and any technique can be applied, though the orientation of the crystal lattice can play a role and should be taken into account. This is not true for superlattices and nanowire devices where measurements in the direction of nanostructuring (perpendicular to the superlattice and in the plane of the nanowire) are warranted.

2.1 In-plane measurements

Van der Pauw method for electrical conductivity

The van der Pauw (vdP) technique is a very useful approach to ascertain the in-plane electrical conductivity of a sample with arbitrary shape.[30] It is essentially a four probe measurement of voltage induced by an electrical current, the accuracy of which depends primarily on the uniformity of the sample under test. The sample must be of uniform thickness and quality; there should be no substantial holes or scratches on the sample surface. Thus, there is no geometry requirement other than the probe contacts must be much smaller than the sample dimensions and placed on the sample perimeter. Square or rectangular samples are conventionally used, though the most accurate sample configuration is the so-called clover leaf pattern, which affords the experimenter more leeway with the contact pad size. The injection current is forced through the central area of

the device and into ground of the adjacent pad; little current arrives at the areas where voltage is measured making this effectively an open-circuit voltage measurement. These two vdP configurations are displayed in Figure 2.1. Commonly, the four Ohmic contacts are formed using electrodes made from a smidgen of indium positioned at the perimeter, which is then heated above its melting point (~160 ° C). Metal electrodes can also be deposited and patterned by lithographic processing, thus providing more control over the contact area.

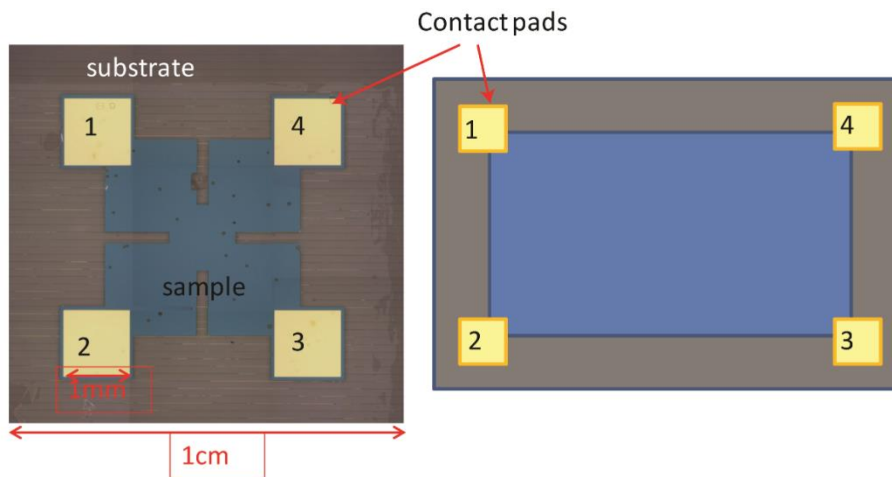

Figure 2.1: van der Pauw sample configurations. The left hand sample displays an optical image of the vdP clover leaf pattern.

Each measurement of electrical conductivity by the vdP method consists of two resistance measurements: R_{ver} and R_{hor}. For one direction of current, for example from contact 1 to 2 in Figure 2.1, the voltage is measured between contacts 3 and 4 to obtain the first resistance: $R_{12,34} = V_{34}/I_{12}$. To help ensure measurement precision, the contact sets are then switched in terms of applied current and measured voltage to obtain $R_{34,12} = V_{12}/I_{34}$. These two

resistances must be identical in accordance with the reciprocity theorem,[30] but the finite contact size and slight variance in probe positions may cause a discrepancy between them. The results are averaged to reduce these discrepancies in the determination of R_{ver}. R_{hor} is attained in a similar way. A current is sent from contact 1 to the other adjacent contact, 4, and the voltage between 2 and 3 is measured to gain $R_{14,23} = V_{23}/I_{14}$. And again, $R_{23,14} = V_{14}/I_{23}$ is acquired such that R_{hor} is the average of $R_{14,23}$ and $R_{23,14}$. Inserting these two resistances in the vdP formula, one can calculate the sheet resistance, R_S, of the sample by

$$1 = e^{-i\pi\frac{R_{ver}}{R_S}} + e^{-i\pi\frac{R_{hor}}{R_S}}. \tag{2.1.1}$$

This equation is solved iteratively until the calculated sheet resistance converges. The electrical conductivity of the sample is given as:

$$\frac{1}{\sigma} = R_S d \tag{2.1.2}$$

where d is the thickness of the film.

These formulae were derived assuming four infinitely small point-like contact pads at the sample perimeter. In reality, contact pad size is not negligible and is a significant source of error in the measurement, which will be on the order of the ratio of pad width divided by the distance between contact pads. Utilizing the clover leaf pattern overcomes these issues since the potential distribution is essentially uniform at the points of voltage measurement,

regardless of contact size (up to a point).The uncertainty in the sample thickness, *d*, can contribute substantial error in the measurement, as well.

When performing these measurements on thermoelectric devices in a vacuum environment at elevated temperature, it is advantageous to reverse the current polarity and/or measure the slope of several sampled voltages. This eliminates the contribution of parasitic Seebeck voltages and voltage offsets induced by thermal gradients that may be present due to non-isothermal conditions in the chamber. A total of eight measurements are made to obtain the two vdP resistances, R_{ver} and R_{hor}. However, the thermoelectric sample itself will also generate a Seebeck voltage. Peltier heating and cooling occurs at the interface between the sample and the contact pads, creating a temperature difference across the sample, as does Joule heating within the device. These effects cannot be avoided; consequently, the applied current magnitudes should be kept at a minimum.

Differential Seebeck coefficient measurement

In a thermoelectric material, a Seebeck voltage, V_S, is created between two points of unequal temperature in the sample. The Seebeck coefficient is simply the generated voltage per degree K temperature change (ΔT),

$$S = \frac{V_S}{\Delta T} \tag{2.1.3}$$

and for most thermoelectric materials is usually given in units of μV/K. Therefore, the determination of the Seebeck coefficient requires the measurement of two quantities: the applied temperature difference across the sample and the voltage generated by the temperature change at the same points of reference.

In-plane Seebeck measurement involves imposing a temperature difference across a sample whose length is much greater than its width. This will ensure one-dimensional heat flux in the sample. No current should be flowing through the sample; there is only the resultant net diffusion of charge carriers. We suspend the sample between two isothermal blocks (see Figure 2.2) which heat-sinks the two ends of the sample at specifically designated temperatures.[31] Ideally, the measurement is executed under steady-state conditions with the device under test in perfect thermal contact with the stage, such that the only thermal gradient is due to the temperature difference of the isothermal blocks. However, there exists a finite thermal resistance between the sample and the measurement stage, as well as possible influence from device inhomogeneity and externally imposed parasitic gradients. To improve the accuracy of the method, the temperature and resultant Seebeck voltage are measured at precisely the same locations of the device. ΔT is measured absolutely using a pair of type R (Pt/ 13 % Rh-Pt) thermocouples, while the voltage generated across the device is measured at each end utilizing a single thermocouple leg. In this case, we selected the platinum leg since this material has the smaller inherent Seebeck coefficient and is the industry standard.

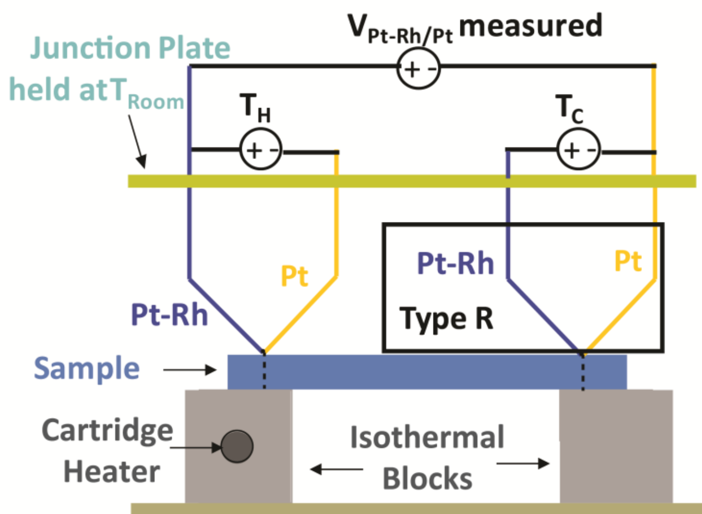

Figure 2.2: Schematic of the side view of a sample mounted for in-plane measurement depicting the circuit used for the differential Seebeck measurement.

The experiment proceeds as follows: the thermoelectric device is mounted onto the isothermal blocks using a small amount of thermal paste. Electrically and thermally conductive silver or platinum paste (depending on the temperature range of interest) is used to ensure good thermal contact between the thermocouple probe tips and the sample surface/contact pad. This also helps to improve the adherence of the probe tips to the sample, as thermal expansion in the measurement stage and the device under test can cause the probes to move and lose contact at higher temperatures. Small thermal gradients are applied along the length of the sample by supplying power to the individual heaters in the isothermal blocks. The thermal gradient is kept within 10 K or so of the temperature of interest; that is, in the linear response regime. Several data points of varying temperature differences are collected and the slope of V_S with respect to ΔT gives the Seebeck coefficient. The data for two thin film samples analyzed for prospective use in superlattice

material systems are given in Figure 2.3. The viewgraphs show six *ΔT*s are measured, but one hundred data points are taken at each *ΔT* for a total of six hundred collected data points. More detail about the measurement stage is found in Chapter 6.

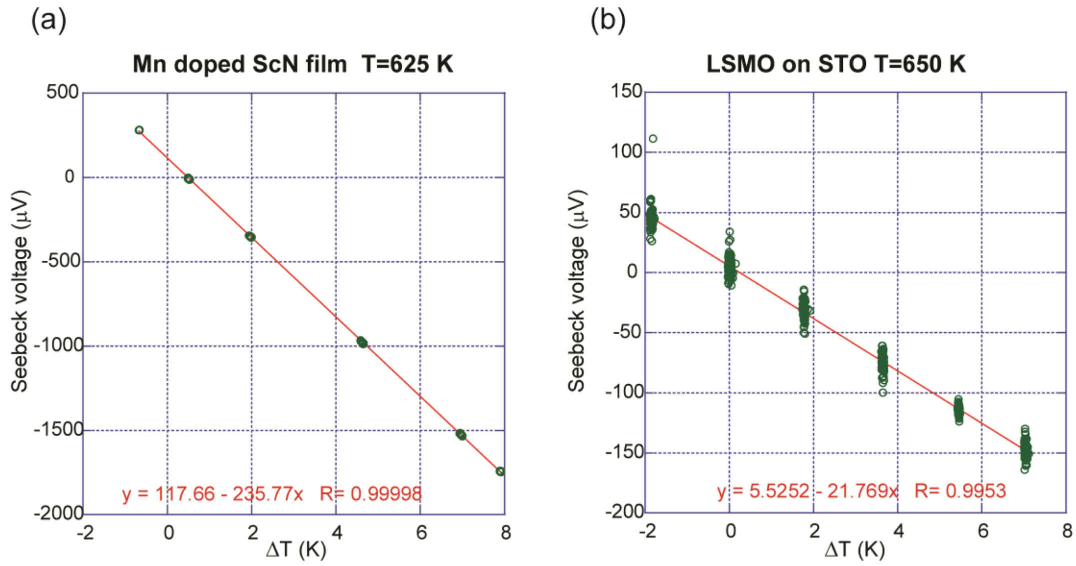

Figure 2.3: In-plane Seebeck coefficient measurement of thin film samples at approximately 650 K by the differential method. (a) The absolute Seebeck coefficient measurement of a Mn doped ScN film with 500 nm thickness. (b) Absolute Seebeck coefficient data collected for 400 nm thick $La_{0.67}Sr_{0.33}MnO_3$ film. In both cases, each data cluster is comprised of one hundred data points. Error in the voltage measurement of LSMO on STO is higher considering the smaller Seebeck coefficient of the material, though it only contributes ~2 % error to the calculated value of *S.*

The spread in each data cluster along with the linear fit quality establishes the error in this measurement. Spread along the y-axis is indicative of voltage fluctuations in the measurement apparatus, while spread in the temperature difference (x-axis) may point to non-ideal thermal resistances between the sample and the probes. Large clusters and/or a

poor linear fit may point to non-uniform heat flow suggesting poor probe and sample placement.

The effect of thermal resistance between the probe tip and sample surface is far greater than any electrical resistance at the interface, and thus impedes the accurate measurement of the Seebeck coefficient. The thermal heat flux, *Q*, relates the thermal resistance, R_{th}, between the thermocouple probe tip and the device to the temperature drop across the interface.

$$\Delta T_{interface} = Q * R_{th} \tag{2.1.4}$$

In addition to reducing the thermal resistance with the application of silver or platinum paste, we minimize *Q* by allowing the measurement apparatus to reach thermal equilibrium between measurements. We establish an adequate wait time after each temperature step before collecting data; typically, up to three minutes between Δ*T* measurements is allotted. Smaller thermocouple tips reduce the requisite wait time.

Finally, error estimates in *S* should include the calibration error of thermocouple probes used in the measurements. This will affect both measured quantities. Calibration error in the absolute temperature measurement for type R thermocouples is less than 1 K, at all temperatures sampled in this work.[32] As mentioned above, the Seebeck voltage is measured relative to the platinum thermocouple leg, which is the common reference material for relative Seebeck measurements. This approach contributes approximately -6 to -12 μV/K to the measurement of the Seebeck coefficient in the temperature range of the chamber, as calculated using thermocouple reference tables supplied by the

manufacturer.[32] For good thermoelectric materials, this is an error of less than 10 %. However, the absolute Seebeck coefficient is often required, especially for characterization of structures whose Seebeck coefficients are close to zero. For example, the in-plane *S* in a superlattice may be minimal or change sign at increased temperature, while the cross-plane *S* is significantly enhanced.[33] If the two electrodes are assumed to have equal parasitic Seebeck coefficient at a given base temperature, the actual Seebeck coefficient of the sample is obtained by subtracting this value; here, the measured voltage relative to both the Pt and Pt-Rh leads ($V_{meas,\ Pt/PtRh}$) is used to extract the absolute Seebeck voltage ($V_{S,ABS}$) of the material under test since the calibration information for the type R thermocouple is readily available. Figure 2.2 illustrates this probe configuration for measurement of the Seebeck coefficient. The inverse calibration polynomial takes the form:[34]

$$V_{TC} = \sum_{i=0}^{n} c_i T^i \qquad (2.1.5)$$

where *T* is the average temperature measured by the two thermocouples, V_{TC} is the output voltage of the type R thermocouple at temperature T, and c_i refers to the calibration coefficients. Thermocouple manufacturers usually give the calibration coefficients accurate to within a tenth of a degree. The Seebeck voltage of the thermocouple at the measurement temperature, relative to room temperature, is subtracted from the total measured voltage to give the absolute Seebeck voltage of the sample.

$$V_{S,ABS} = V_{meas,Pt/PtRh} + [V_{TC}(T_{AVG}) - V_{TC}(T_{Room})]. \qquad (2.1.6)$$

Total error can be as large as 10% and increases with ambient temperature.

Consolidation of in-plane measurements

Simultaneous measurements of the electrical conductivity and the Seebeck coefficient are accomplished by mounting a thermoelectric device with vdP geometry across the two heating blocks. It is crucial that the thermocouples are placed in good thermal contact with the measurement stage. For thin film samples, only four probes are necessary: we utilize two platinum electrical probes and two type R thermocouples. Electrical conductivity is measured as above using the two electrical probes and two identical legs of the thermocouples while the two heating blocks are maintained at the same ambient temperature. A temperature gradient is subsequently applied to the device under test and the generated voltage and temperature are measured by the two thermocouples. The criterion of one-dimensional heat flux is fulfilled simply by heating the bottom of the sample, since the thickness of the film is on the order of micrometers. A schematic of a thin film sample with vdP geometry mounted in this fashion is illustrated in Figure 2.4a. However, a caveat of the method is the presence of the growth substrate, whose material properties can dramatically affect the perceived parameters of the thin film. A thermally conductive, electrically insulating substrate is ideal, though many common substrates, including InP or Si, are electrically conductive or become so at high temperatures. In these cases, we remove the problematic growth substrate and transfer the thin film to a more ideal material, such as sapphire.[35] The temperature dependent Seebeck coefficient and electrical conductivity of a novel p-type thin film with differing doping and nanoparticle concentrations are displayed in Figure 2.4b and Figure 2.4c, respectively.

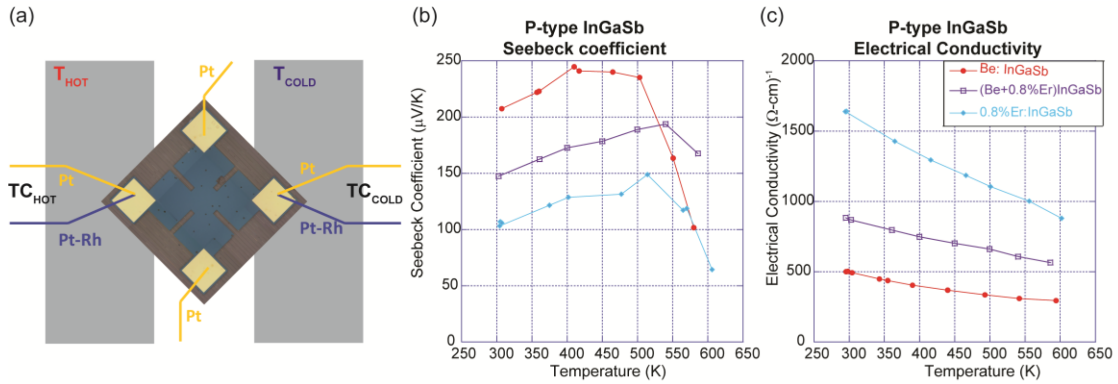

Figure 2.4: (a) A top down view of the sample stage for simultaneous measurements of electrical conductivity and Seebeck coefficient of a sample with clover leaf vdP geometry. Two electrical probes (in yellow, single lead) and two thermocouples (TC_{Hot}, TC_{Cold}) are used for measurements. (b) The high temperature behavior of the Seebeck coefficients shows substrate contributions around 550 K. (c) Electrical conductivities of the films are displayed. High temperature measurement results for the InGaSb thin film compare Be doping behavior to 0.8 % nanoparticle inclusion.

The approach taken for bulk samples in the experiments described in this work is slightly more complex. Van der Pauw geometry is still applicable and four electrical probes are positioned on the sample perimeter. However, the thermocouples cannot be utilized as electrical probes during the vdP measurement; six measurement probes including two thermocouples are used in total. Bulk materials have a finite thickness on the order of the device length and width, encouraging three-dimensional heat flow. To solve this, we heat sink the sample on three sides, leaving the surface open for electrical probing. A bulk sample mounted on this stage is depicted in Figure 6.1 in Chapter 6. The thermocouples are channeled through the measurement stage and measure temperature and Seebeck voltage at the center of the sample thickness. Thus, the thermocouples and device are at thermal equilibrium with their respective isothermal blocks and a one-dimensional thermal gradient is achieved. More information about the bulk measurement stage is offered in Chapter 6.

Hence, the Seebeck coefficient and electrical conductivity are determined using the same experimental setup under identical ambient conditions.

2.2 Cross-plane measurements

3ω method for measurement of thermal conductivity

The 3w methodology was introduced and developed by Cahill *et. al.* to quantify the frequency response of a thermal wave in a semi-infinite solid by utilizing a resistive metal line as both heater and thermometer. It has become the standard technique for measurement of thermal conductivity for bulk materials/substrates[36] and thin films[37,38], and is quite easily implemented for measurement in a vacuum thermostat. We employ the standard experimental procedure in this work, which was greatly improved by collaboration with Arun Majumdar's group at the University of California, Berkeley (currently at Stanford University). More information including a full derivation of the heat equation and in-depth uncertainty analysis can be found in references 39, 40.

Simply put, a sinusoidal current is applied to the heater line at frequency 1ω, inducing Joule heating in the sample at 2ω (since Joule heating is proportional to the square of the current). The resistance of the metal heater line changes linearly with temperature, therefore, the heater line also oscillates at frequency 2ω. By analyzing the circuit in terms of Ohm's law, it becomes evident that the detection of 3ω voltage fluctuation in the heater line will reveal information about the temperature oscillations; $V_{3\omega} = I_{\omega} * R_{2\omega}$.

The experimental circuit is illustrated in Figure 2.5. The small temperature dependence of the heater line resistance necessitates the use of lock-in detection of the 3ω voltage. Hence, a voltage source is used to bias the circuit, given as

$$V_{source} = V_0 \cos(\omega t),$$

and the current is thus:

$$I = \frac{V_0 \cos(\omega t)}{R_h + R_{ext} + R_{l-in}}. \tag{2.2.1}$$

The sum of the heater line resistance, R_h, the non-temperature dependent external resistance, R_{ext}, and the internal resistance of the lock-in amplifier, $R_{l\text{-}in}$, constitutes the total resistance (R_T) in the circuit. As mentioned previously, the resistance of the heater line varies with the 2ω fluctuation in temperature:

$$R_h = R_{h,0} + \frac{dR}{dT}\Delta T(2\omega) = R_{h,0}\left(1 + R_{h,0}\alpha\Delta T(2\omega)\right). \tag{2.2.2}$$

We define α as the temperature coefficient of the resistance of the metal line and $R_{h,0}$ is the initial resistance of the heater line without applied bias. Again, we determine the change in temperature of the heater line in terms of the applied voltage utilizing the thermal Ohm's law for Joule heating:

$$Q_{Joule} = I^2 R_h\,;$$

$$\Delta T(2\omega) \approx \frac{V_0^2 R_{h,0}}{\left(R_{T,0}\right)^2}\frac{R_{Th}\cos(2\omega t)}{2} = \Delta T_{2\omega}\cos(2\omega t) \tag{2.2.3}$$

where we have made the assumption that $R_h \approx R_{h,0}$. R_{Th} is the thermal resistance in the heater line at ω and $R_{T,0}$ is the initial total resistance in the circuit: $R_{T,0} = R_{h,0} + R_{ext} + R_{I\text{-}in}$. Note that this is only the 2ω component of the heat generated in the heater line, there is also a DC component. Combining the equations for $\Delta T_{2\omega}$ (2.2.3) and R_h (2.2.2) and inserting them into the equation for current (2.2.1), the voltage drop across the heater line (V_h) is obtained:

$$V_h = \frac{R_{h,0}V_0}{R_{T,0}}\left[\left(1 + \frac{\alpha\Delta T_{2\omega}}{2} - \frac{R_{h,0}\alpha\Delta T_{2\omega}}{2R_{T,0}} - \frac{R_{h,0}\alpha^2\Delta T_{2\omega}^2}{2R_{T,0}}\right)\cos(\omega t) + \left(\frac{\alpha\Delta T_{2\omega}}{2} - \frac{R_{h,0}\alpha\Delta T_{2\omega}}{2R_{T,0}} - \frac{R_{h,0}\alpha^2\Delta T_{2\omega}^2}{4R_{T,0}}\right)\cos(3\omega t) - \frac{R_{h,0}\alpha^2\Delta T_{2\omega}^2}{4R_{T,0}}\cos(5\omega t) + \cdots\right] \quad (2.2.4)$$

This calculation is valid assuming that $R_{h,0} << R_{T,0}$ and that the quantity $\alpha\Delta T_{2\omega} << 1$, in which case all higher order terms in α (including α^2)may be ignored. Thus, the voltage drop across the heater line is comprised of a 1ω term ($V_{1\omega,h}$) and a 3ω term ($V_{3\omega,h}$), as expected.

A similar analysis can be made for the voltage across the external load, V_{ext} which in this experiment is a potentiometer, as depicted in Figure 2.5.

$$V_{ext} = \frac{R_{ext}V_0}{R_{T,0}}\left[\left(1 - \frac{R_{h,0}\alpha\Delta T_{2\omega}}{2R_{T,0}}\right)\cos(\omega t) + \left(\frac{R_{h,0}\alpha\Delta T_{2\omega}}{2R_{T,0}}\right)\cos(3\omega t)\right] \quad (2.2.5)$$

Setting $R_{ext} = R_{h,0}$ and ignoring the higher order terms in V_h (equation 2.2.4) :

$$\left(V_{1\omega,h} - V_{1\omega,ext}\right) = \left(V_{3\omega,h} - V_{3\omega,ext}\right) = \frac{R_{h,0}V_0}{R_{T,0}}\frac{\alpha\Delta T_{2\omega}}{2} \approx V_{1\omega}\frac{\alpha\Delta T_{2\omega}}{2}. \quad (2.2.6)$$

Physically, the reason for the inclusion of the external resistor is to balance the 2nd order effect on current caused by heating in the heater line, due to our use of a non-ideal current source. The heater line itself acts as an additional voltage source in the circuit which must

be ‘dropped’ across a load; the differential measurement removes this background 3ω current. Hence, the difference in either the 1ω or 3ω components of the two voltages can be used to determine the magnitude of the temperature fluctuation at 2ω. It is commonplace to examine the 3ω voltages in the circuit since the voltage difference is so small it can easily be construed as error in a 1ω voltage measurement, although any phase difference between $V_{3\omega,h}$ and $V_{3\omega,ext}$ must also be taken into account.

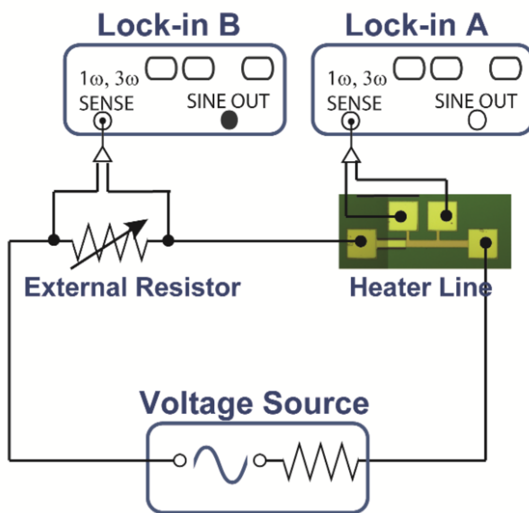

Figure 2.5: Experimental schematic/circuitry used for high temperature 3ω measurement.

The relationship between thermal conductivity and the temperature difference has been derived elsewhere[41,36] from the analytic solution to the transient heat equation. In the case of an isotropic, semi-infinite material the thermal conductivity, κ_{bulk}, is typically acquired either by measuring the $V_{3\omega}$ at many different frequencies of applied bias and/or by performing an applied voltage sweep while holding ω constant.

$$\kappa_{bulk} = \frac{-P}{2\pi L}\left(\frac{d(\Delta T)}{d(\ln(2\omega))}\right)^{-1} \quad \text{or} \quad \kappa_{bulk} = \frac{\alpha}{2\pi L R_{h,0}}\left(\frac{d(V_{3\omega,h} - V_{3\omega,ext})}{d\left({V_{1\omega}}^3\right)}\right)^{-1}. \qquad (2.2.7)$$

P is the power dissipated across a heater line of length *L*.

The measurement is valid for an infinitely narrow heater line on a semi-infinite substrate. In order to achieve these conditions, the penetration depth of the thermal wave, L_P, must be much greater than the width of the heater line though still contained within the material layer of interest. The appropriate frequencies are calculated from the thermal diffusivity, D_{Th}, of the material using:

$$L_p = \sqrt{\frac{2D_{Th}}{\omega}}. \qquad (2.2.8)$$

If the applied frequencies are constrained appropriately, $\Delta T_{2\omega}$ plotted as a function of ln(ω) is linear and κ_{bulk} is simply the slope of the line. This characteristic 3ω result is shown in Figure 2.6 for a metal heater line deposited on a 525 µm thick silicon substrate with a thermally grown 200 nm SiO_2 dielectric layer for electrical insulation. It can be shown that the presence of the dielectric layer adds a frequency independent term to $\Delta T_{2\omega}$; the slope of the line representative of a frequency sweep still only conveys the bulk material information. More details on this measurement are given below and the treatment with an additional film is presented in the next section.

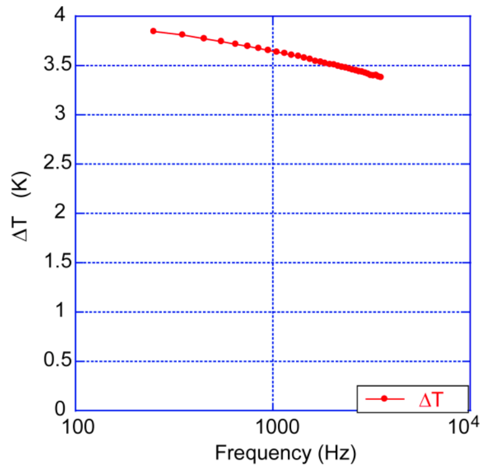

Figure 2.6: The characteristic 3ω curve for a simple case of a metal (gold) heater line deposited on a silicon substrate at 295 K. The thermal conductivity of silicon is determined to be 156 W/m-K, which matches well with reference values.[42,43]

The measurements reported in this work are taken under the following experimental conditions: the 3ω device is mounted in the vacuum thermostat on a large sample stage which functions as a thermal heat sink and varies the ambient temperature of the measurement. The circuitry is as depicted in Figure 2.5; a potentiometer is mounted in series with the heater line but external of the thermostat. Lock-in A is used to deliver a sinusoidal voltage and measure both the 1ω and 3ω responses of the heater line, while lock-in B is used to detect the 1ω and 3ω voltages across the external resistor for the differential measurement. Initially, the resistance of the heater line $R_{h,0}$ is measured in a four probe configuration where the currents applied to the circuit are kept small such that heating in the sample is negligible. The resistance of the potentiometer is set to match $R_{h,0}$. Since this method of resistance matching is not exact, we insert the average 1ω voltage ½($V_{1\omega,h}$ +

$V_{1\omega,ext}$) as $V_{1\omega}$ into the above equations. The difference between the 1ω voltage drops is potentially a large source of error in the measurement.

The use of the heater line as both heater and thermometer, and consequently the dependence of the heater electrical resistance with temperature, *dR/dT,* must be calibrated for each individual heater line over the temperature range of the experiment. This is accomplished by measuring the DC voltages from an applied current sweep across the heater line while slowly ramping the ambient temperature in the chamber. Again, the current amplitudes are kept small so as not to generate measurable heating in the sample. We measured α for three separate 300 µm x 24 µm heater lines with 100 nm thickness, each made of a different evaporated metal: gold, aluminum, and platinum. In all cases, the *dR/dT* values were linear with ambient temperature and are presented here for the respective metals: (5.5 ± 0.043) x 10^{-3}, (7.2 ± 0.037) x 10^{-3}, and (23 ± 0.66) x10^{-3} Ω/K below 550 K. These correspond to values for α much smaller than 1.

The thermal conductivity of the silicon sample is plotted with respect to ambient temperature in Figure 2.7. We used a 300 ms time constant with a 12 dB low pass filter and high reserve as the lock-in amplifier settings to stabilize the 3ω signals in the appropriate frequency range for this device. There were three dominant sources of error in this measurement: error in the resistance matching as mentioned above, error in the fit of κ as per equations 2.2.7, and error in the linear fit of α coefficient. Error in α became more significant at higher temperatures. The metal of the heater line began to anneal, around 500 K for gold and much later for platinum considering it is a much more inert material, as reflected in the error bars in the figure.

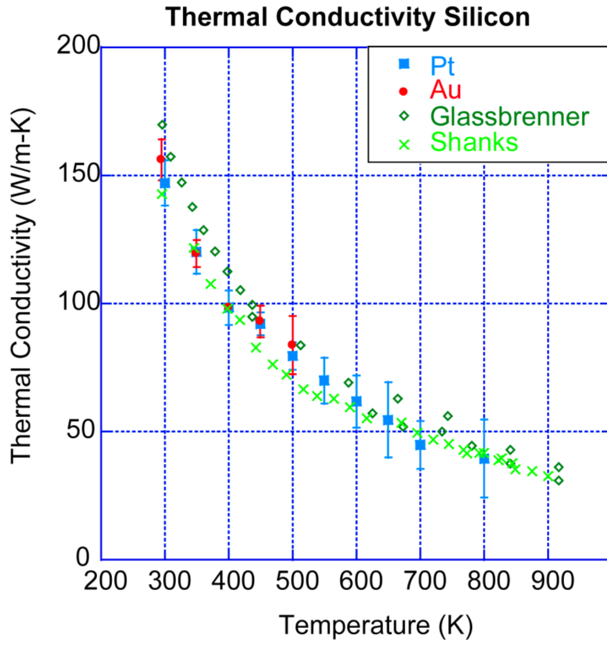

Figure 2.7: High temperature thermal conductivity of a silicon substrate, attained by 3ω measurement using various metal heater line compositions, plotted in comparison to the data from references 42 and 43.

Extension to measurement of the cross-plane Seebeck coefficient

The heat flux through an additional thin film layer with much lower thermal conductivity than the device substrate is one-dimensional and can be considered quasi-static in the thermal regime, as long as the penetration depth of the thermal wave extends far into the substrate. Refer to Figure 2.8a. The contribution of the frequency independent term of the thin film to $\Delta T_{2\omega}$ is apparent when relating the 3ω voltages generated from the temperature fluctuation to the thermal conductivities of sample structure:

$$\frac{d(V_{3\omega,h} - V_{3\omega,ext})}{d({V_{1\omega}}^3)} = \frac{\alpha}{2LR_{h,0}}\left(\frac{1}{\pi\kappa_{bulk}} + \frac{d_f}{w\kappa_f}\right) \tag{2.2.9}$$

where d_f and κ_f are the thickness and thermal conductivity of the film, respectively, and w refers to the width of the heater line. A so-called 'differential' approach is used to extract the temperature component of the film, thus requiring two separate measurements under identical experimental conditions. One measurement is performed on the device which includes the material of interest and determines the total 2ω temperature fluctuation, $\Delta T_{2\omega,Tot}$. Another measurement obtains the $\Delta T_{2\omega,ref}$ of a reference sample where only the thin film is absent. Thus, any difference in temperature between the two measurements is solely due to the temperature contribution of the film; $\Delta T_{2\omega,f} = \Delta T_{2\omega,Tot} - \Delta T_{2\omega,ref}$.This strategy neglects any effect of the thermal resistance of the interface between the film and substrate. The thermal conductivity of the film is calculated as:

$$\kappa_f = \frac{d_f}{Lw}\left({}^{\Delta T_{2\omega,Tot}}\!/_{P} - {}^{\Delta T_{2\omega,ref}}\!/_{P} \right)^{-1}. \quad (2.2.10)$$

The conventional 3ω technique was expanded upon by Yang *et al.*[44] and Zhang *et al.*[45] to measure the cross-plane Seebeck coefficient of a superlattice device. Joule heating propagating in the thermoelectric film creates a Seebeck voltage which also fluctuates at 2ω frequency and can be detected using the lock-in configuration already proposed. Thus, the 1ω, 2ω, and 3ω voltages are measured in turn for a 'total' device, that is, one with the thermoelectric film and other required layers, and a reference sample, where only the film is absent or much thinner. The primary complication to the original measurement scheme is that the Seebeck voltage must be measured across the film itself, necessitating the fabrication of additional electrodes without influence from the heat source. A schematic depicting the sample structure is presented in Figure 2.8a for a superlattice thin film device.

The Seebeck voltage electrodes are located at the interface of the insulating medium and the film and at the bottom surface of the film between the thermoelectric material and substrate. The Seebeck coefficient of the film (S_f) is given as:

$$S_f = \frac{\Delta V_{2\omega,Tot} - \Delta V_{2\omega,ref}}{\Delta T_{2\omega,Tot} - \Delta T_{2\omega,ref}}. \tag{2.2.11}$$

$\Delta V_{2\omega,Tot}$ and $\Delta V_{2\omega,ref}$ refer to the 2ω voltages measured over the 'total' and reference devices, respectively. We utilize a serpentine heater design deposited on the superlattice mesa to approximate one-dimensional heat flow through the thermoelectric film.

We report a representative measurement of an n-type thermoelectric superlattice consisting of 70 periods grown on *n*-InP substrate with InGaAs buffer layer, performed at University at California, Santa Cruz. Each period is comprised of 20 nm film of InGaAs with 0.3% ErAs inclusions and 10 nm $InGaAs_{0.6}InAlAs_{0.4}$ digital alloy. The measured 2ω Seebeck voltages relative to the reference sample are presented in Figure 2.8b. The 2ω Seebeck voltages decrease with frequency, anticipated by the dependency of the sample thermal impedance on the frequency of voltage oscillation.

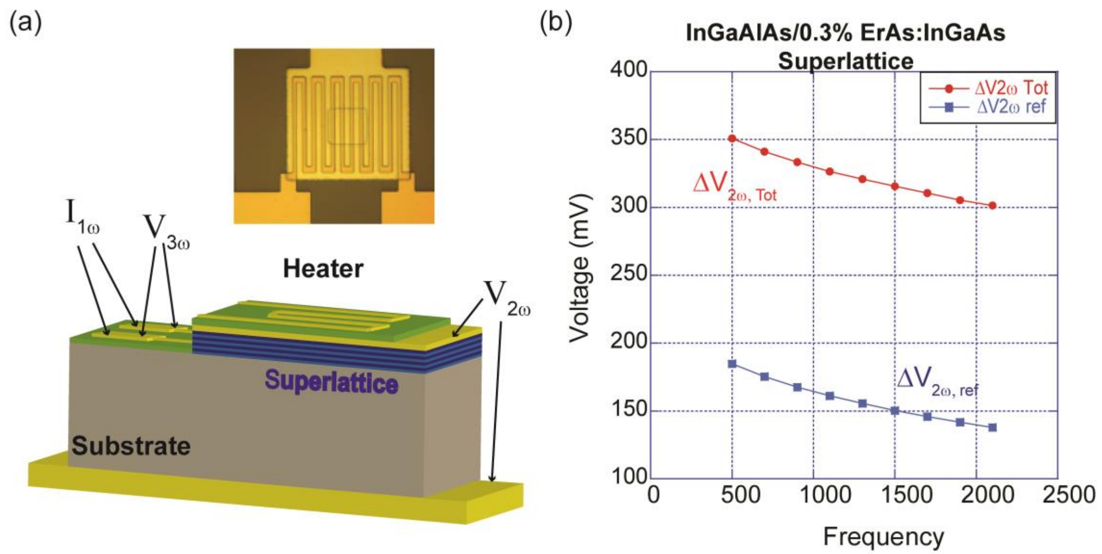

Figure 2.8 (a) Schematic of a superlattice device prepared for cross-plane Seebeck and thermal conductivity measurements. The upper image is a top-down view of the serpentine heater line. (b) The measured 2ω Seebeck voltages in a device and reference sample generated in the thermoelectric superlattice layer due to heating from the surface resistance heater, plotted as a function of frequency. The difference between the two curves is the actual 2ω voltage of the thermoelectric film.

Chapter 3 Thermoreflectance Thermal Imaging

Thermoreflectance microscopy is a versatile, noninvasive technique that generates two-dimensional temperature maps of active device surfaces. It has become especially valuable in thermoelectric material characterization with the adaptation of the conventional sinusoidal excitation method[46] to distinguish between the Peltier and Joule components in the total temperature signal. The latter oscillates at twice the frequency of the excitation current while the former manifests at the fundamental frequency. Consequently, it is immensely useful in determining the energy conversion efficiency of thermoelectric devices, diagnosing faults, and visualizing thermal parasitic effects.

Thermoelectric devices utilized for power generation, as primarily examined in this work, are designed for maximum conversion efficiency at elevated temperatures. Many of the complications accompanying the high temperature characterization of these devices can be readily identified in a surface temperature map. Unfortunately, there has not been extensive application of thermal imaging at temperatures above ambient; perhaps in part due to the unknown behavior of reflectivity dependence on temperature and the feasibility of optical measurements in a vacuum chamber. Wang *et al.* employed thermoreflectance mapping of cryogenic nanowires,[47] but did not take into account any change in the thermoreflectance coefficient with temperature. Much of the work reported in this thesis describes the development and the first ever implementation of thermoreflectance imaging at high temperatures to enable thermal profiling at specific temperatures of interest and thus elucidating underlying temperature-dependent device physics. In addition, this

application of the technique can provide real-time device failure analysis upon temperature cycling.

In this chapter, we present the different approaches utilized in this work for charge coupled device (CCD) based detection of the reflectivity variations and thus the temperature change in thermoelectric devices and the associated benefits of each method. The '4-bucket' method[46] is the generalized approach that can be extended for use on nonlinear (non-ohmic) devices. The '8-bucket' technique[48] provides real-time Peltier and Joule separation over the course of a single measurement. Transient thermoreflectance captures the temporal behavior of a device which is particularly interesting in thermoelectric samples considering the different time responses of the Peltier and Joule effects.[49] We then discuss the implementation of the experimental method in unique investigations that demonstrate the breadth of the technique. High temperature thermoreflectance is employed on thermoelectric thin films and a strategy is established for the requisite high temperature calibration of the thermoreflectance coefficient.

3.1 General Principle

The basic thermoreflectance experimental set up used for these measurements is as follows (Figure 3.1): Light is emitted from a narrowband LED to the beam splitter and is focused through a microscope objective on the device-under-test (DUT), which is held in a vacuum thermostat. A periodic voltage pulse is applied to the DUT to create an oscillating temperature field comprised of Peltier and Joule signals. The change in temperature relative to ambient is detected by the CCD camera as an alteration in the reflected light. The CCD is phase-locked with the reflected signal, operating at a selected integer multiple (n) frequency

of the applied bias. The captured images correspond to a 1/nth-period integral of the bias signal and are used to reconstruct a single excitation cycle. Averaging over many cycles improves the signal-to-noise ratio of this lock-in technique. The instrument settings differ depending on the thermoreflectance measurement approach used; measurement specifics are given in the following sections. In all cases, the basic thermoreflectance equation is used to obtain the temperature variation (ΔT) owing to the thermoelectric effects from the measured reflectivity change (ΔR):

$$|\Delta T_P| = \frac{|\Delta \mathrm{R}_P|}{C_{TR} \cdot \mathrm{R}_{DC}} \qquad |\Delta T_J| = \frac{|\Delta \mathrm{R}_J|}{C_{TR} \cdot \mathrm{R}_{DC}}. \tag{3.1.1}$$

The subscripts P and J respectively refer to Peltier and Joule signals, C_{TR} is the thermoreflectance coefficient, and R_{DC} is the baseline reflectivity.

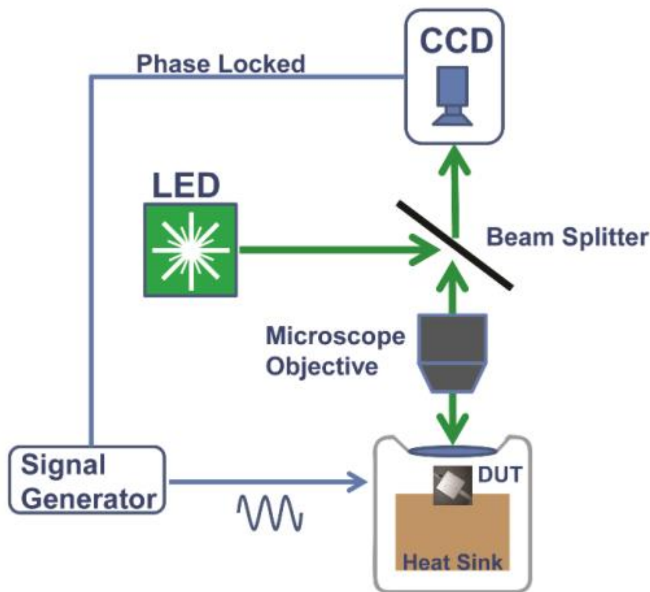

Figure 3.1: Basic experimental apparatus for high temperature thermoreflectance thermal imaging.

4-bucket approach to thermal imaging: homodyne method

The formulism used here is the extension of the conventional method introduced by Grauby *et al.* in 1999. We apply an offset sinusoidal current (I_{app}) with frequency ω to the DUT. The bias period is chosen to be much larger than the typical thermal response time of the device, such that the DUT is operating in the quasi-static regime. In this way, the detected reflectivity signal (R_{meas}) directly follows the temperature oscillation, with a relative phase difference ϕ:

$$I_{app} = \frac{I_0}{2} + \frac{I_0 \sin(\omega t)}{2}$$

$$\mathrm{R}_{meas} = \mathrm{R}_{DC} + \Delta\mathrm{R}\sin(\omega t + \phi). \qquad (3.1.2)$$

We select the offset such that the applied current varies from 0 to I_0.

The LED provides constant illumination for the duration of the experiment. The CCD is locked to the signal, *s(t)* at the first harmonic. The detected change in reflectivity can be reconstructed with four image bins (B_n) of similar phase, (hence the designation ‘4-bucket’):

$$B_n = \int_{(n-1)/4}^{n/4} s(t)dt \qquad n = 1 \dots 4 \qquad (3.1.3)$$

The change in reflectivity and relative phase are extracted as:

$$\frac{\Delta\mathrm{R}}{\mathrm{R}_{DC}} = \frac{2\pi}{\sqrt{2}} \frac{\sqrt{(B_1 - B_3)^2 + (B_2 - B_4)^2}}{B_1 + B_2 + B_3 + B_4} \qquad (3.1.4)$$

$$tan\phi = \frac{B_1 + B_2 - B_3 - B_4}{B_1 - B_2 - B_3 + B_4}. \tag{3.1.5}$$

The maximum frame rate of the DALSA CCD utilized in this work is 30 frames per second; accordingly we set ω = 2π·7.5 Hz. The specifications of this thermoreflectance measurement are exhibited in Figure 3.2a, in comparison with the other methods described in this chapter.

Bipolar measurements exploit the respective linear and quadratic current dependencies of the Peltier and Joule temperature fields; Joule is always heating and the Peltier response flips between cooling and heating modes with current polarity. Two measurements are therefore required to separate the two signals. In the case of reverse bias of a typical n-type thermoelectric material, the temperature oscillations (ΔT_R) and reflectivity (R_R) are given as:

$$\Delta T_R = \frac{T_{DC,R}}{2} + \frac{a}{2} I_0 \sin(\omega t + \phi_a) + \frac{b}{2} {I_0}^2 \sin(\omega t + \phi_b) + \frac{T_{2\omega,R}}{2}$$

$$\mathrm{R}_R = \mathrm{R}_{DC} + \Delta\mathrm{R}_P \sin(\omega t + \phi_P) + \Delta\mathrm{R}_J \sin(\omega t + \phi_J) + \mathrm{R}_{2\omega,R} \tag{3.1.6}$$

where the DC and 2ω terms are collected in the variables with the subscripts *DC* and *2ω*, respectively. *a* and *b* refer to constants that relate the linear (Peltier) and quadratic (Joule) dependencies of the temperature change on current, and ϕ represents their respective phase changes. The 2ω component disappears during signal processing and can be neglected. A similar treatment gives the forward bias expressions:

$$\Delta T_F = \frac{T_{DC,R}}{2} - \frac{a}{2} I_0 \sin(\omega t + \phi_a) + \frac{b}{2} {I_0}^2 \sin(\omega t + \phi_b)$$

$$\mathrm{R}_F = \mathrm{R}_{DC} - \Delta\mathrm{R}_P \sin(\omega t + \phi_P) + \Delta\mathrm{R}_J \sin(\omega t + \phi_J). \tag{3.1.7}$$

It follows that quarter-period Peltier and Joule signals, P_n and J_n, may be ascertained as:

$$P_n = \frac{\int_{(n-1)/4}^{n/4} \mathrm{R}_R dt - \int_{(n-1)/4}^{n/4} \mathrm{R}_F dt}{2}; J_n = \frac{\int_{(n-1)/4}^{n/4} \mathrm{R}_R dt + \int_{(n-1)/4}^{n/4} \mathrm{R}_F dt}{2} n = 1 \dots 4 \qquad (3.1.8)$$

where P_n and J_n may be substituted into the equations for the change in reflectivity (Equation 3.1.4) and relative phase (Equation 3.1.5) to reconstruct these values individually.

In many situations, the sinusoidal waveform used to bias the DUT is supplied by a voltage source such as a function generator. The excitation signal is then dependent on the voltage limitations of the source, its output impedance, and the resistance of the thermoelectric sample itself. If the DUT is not completely ohmic in nature or engenders substantial Joule heating, its nonlinear IV curve will result in the incomplete cancellation of terms upon subtraction of the bipolar signals and/or parasitic higher harmonic contributions. A method to avoid these complications is through the substitution of the sinusoidal bias for a square pulse, which in addition usually allows for higher voltage amplitudes than a function generator and thus potentially stronger signals. Refer to Figure 3.2b for an illustration depicting the required waveforms. This approach is only beneficial when the device turn-off time is considered instantaneous from the perspective of the CCD. In other words, there is no signal leakage between camera frames. The total reflectivity is simply the reflectance in the 'on' state minus the baseline reflectance (off).

$$\mathrm{R}_{R,ON} = \mathrm{R}_{DC} + \Delta\mathrm{R}_P + \Delta\mathrm{R}_J; \qquad \mathrm{R}_{R,OFF} = \mathrm{R}_{DC}$$

$$\mathrm{R}_{F,ON} = \mathrm{R}_{DC} - \Delta\mathrm{R}_P + \Delta\mathrm{R}_J; \qquad \mathrm{R}_{F,OFF} = \mathrm{R}_{DC} \qquad (3.1.9)$$

In keeping with the formulism of the 4-bucket technique, R_1, R_2 are considered 'on' while R_3, R_4 are taken to be 'off'. The calculation of the amplitude of the reflectivity oscillation is greatly simplified:

$$\frac{\Delta R_R}{R_{DC}} = \frac{R_{R1} + R_{R2} - R_{R3} - R_{R4}}{R_{R3} + R_{R4}}; \qquad \frac{\Delta R_F}{R_{DC}} = \frac{R_{F1} + R_{F2} - R_{F3} - R_{F4}}{R_{F3} + R_{F4}}. \quad (3.1.10)$$

The Peltier and Joule reflectivity signals are then:

$$\frac{\Delta R_P}{R_{DC}} = \frac{\Delta R_R - \Delta R_f}{2R_{DC}}; \qquad \frac{\Delta R_J}{R_{DC}} = \frac{\Delta R_R + \Delta R_f}{2R_{DC}} \quad (3.1.11)$$

The end result is as expected, the Joule signal is the average of the response at the two polarities while the Peltier signal is their difference. The 4-bucket method and the modified square pulse version are robust techniques for measurement of low frequency phenomena. The simple mathematical processing of the square pulse version maintains thermal signal polarity and displays heating and cooling in the resulting thermal image. However, there is no phase information using DC excitation. The downside of the techniques is the requisite two separate measurements. The small reflectivity signals commonly require long averaging times to improve the signal-to-noise ratio, which can be plagued by drift in the apparatus and optics, and/or slight movements of the sample. It is not unusual to average a single measurement for 30 to 60 minutes, or more, and then reverse polarity and average again. Any drifts between the two measurement runs will result in the incorrect extraction of the thermal fields.

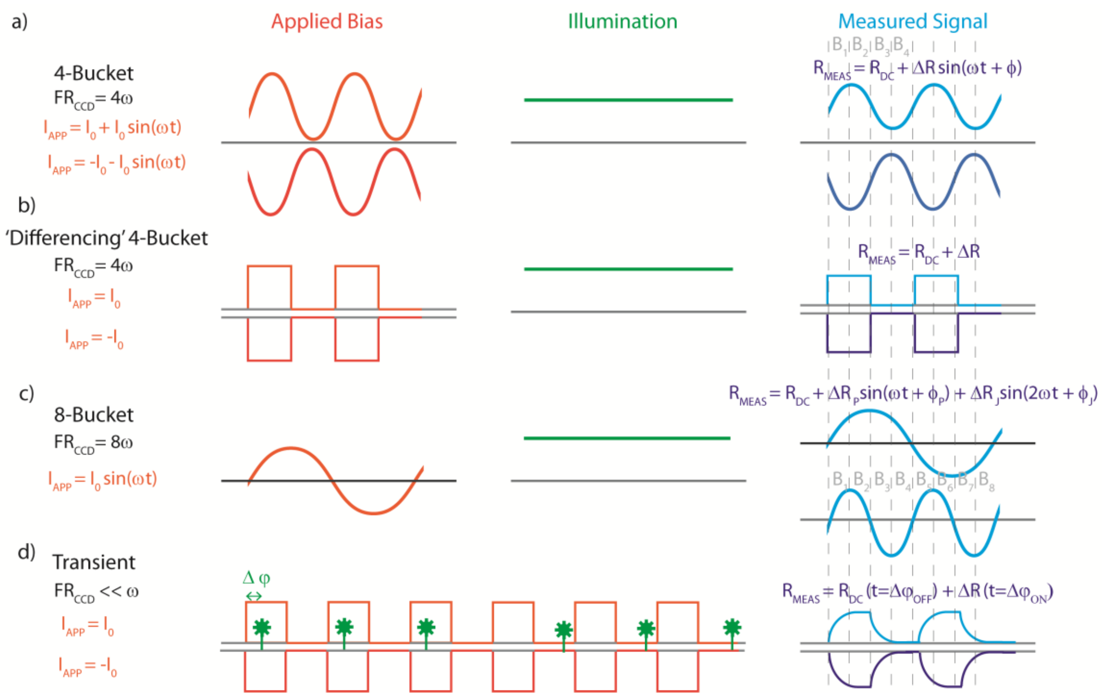

Figure 3.2: Schematic describing the principles of the different thermoreflectance methodologies.

8-bucket technique: simultaneous imaging of Peltier and Joule

The 8-bucket approach avoids these issues by utilizing non-offset sinusoidal excitation; thus a single waveform period is used to collect both forward and reverse polarity signals. Consequently, the Peltier and Joule thermal signals are processed in real-time, and can be viewed during signal averaging. 8-bucket thermal imaging similarly exploits current dependencies of the Peltier and Joule thermal signatures. These effects, however, manifest and are measured directly at the first and second harmonics of the bias signal, respectively, since there is no DC offset. The measured reflectivity signal still closely follows the temperature field, and is simply comprised of both Joule and Peltier components:

$$R_{meas} = R_{DC} + \Delta R_P \sin(\omega t + \phi_P) + \Delta R_J \sin\left(2\omega t + \phi_J\right) \quad (3.1.12)$$

The primary experimental differences in this method, as compared to the 4-bucket, is the application of a non-offset sinusoidal bias and the phase-locked CCD operates at eight times the frequency of the bias signal, n = 8. In this way, eight images are used to reconstruct a single excitation cycle, as shown in Figure 3.2c; for these experiments ω = 2π·3.75 Hz. The DUT is under constant illumination. We represent each eighth-period integral of the reflectivity oscillations with the notation B_n, where n=1…8. The respective reflectivity variations are:

$$\frac{|\Delta R_P|}{R_{DC}} = \frac{\pi}{\sqrt{2}\sqrt{2-\sqrt{2}}} \frac{\sqrt{(B_1 - B_5)^2 + (B_2 - B_6)^2 + (B_3 - B_7)^2 + (B_4 - B_8)^2}}{B_1 + B_2 + B_3 + B_4 + B_5 + B_6 + B_7 + B_8}$$

$$\frac{\left|\Delta R_J\right|}{R_{DC}} = \frac{2\pi}{\sqrt{2}} \frac{\sqrt{(B_1 + B_5 - B_3 - B_7)^2 + (B_2 + B_6 - B_4 - B_8)^2}}{B_1 + B_2 + B_3 + B_4 + B_5 + B_6 + B_7 + B_8} \quad (3.1.13)$$

The relative phase information (ϕ) for the respective temperature fields at each harmonic can be reconstructed as:

$$tan(\phi_P) = -\frac{B_1 + B_2 + B_3 + B_4 - B_5 - B_6 - B_7 - B_8}{B_1 + B_2 - B_3 - B_4 - B_5 - B_6 + B_7 + B_8}$$

$$tan\left(\phi_J\right) = -\frac{B_1 + B_2 - B_3 - B_4 + B_5 + B_6 - B_7 - B_8}{B_1 - B_2 - B_3 + B_4 - B_5 - B_6 - B_7 + B_8}. \quad (3.1.14)$$

The 8-bucket measurement scheme is ideal for characterization of thermoelectric materials, especially those that require long averaging times. The main drawback is the requirement of a perfect, non-offset sinusoidal source. Any presence of a DC bias, or measurement of a device with a strong Joule response, may introduce parasitic signals at 1ω and 3ω. We use a

function generator as a voltage source to drive a sinusoidal current through the measurement circuit. These types of devices (waveform generators), usually have limited output voltage amplitudes which may restrict the reflectivity signal strength.

Transient thermal imaging: pulsed boxcar averaging

The bandwidth of the methods described above is limited by the CCD accumulation frame rate; speeds of approximately 10 to 100 Hz are available. However, these rates are still considered within the steady state regime for thin film materials and microscale devices. Transient thermoreflectance methodology resolves the temporal behavior of thermoelectric devices.

In these experiments, two phase-locked square pulse trains with tunable delays are employed; one excites the DUT and the other flashes the illumination LED. This cycle is repeated over thousands of pulses in a single CCD frame, resulting in an accumulated snapshot of the device at a chosen time in the device excitation cycle. Comparing this 'on' frame to an 'off' reference frame, i.e. an additional snapshot taken during the device idle state, provides the temperature data. The full thermal transient can be captured by gradually advancing the phase delay (φ) between the two pulse trains. The bandwidth of this technique is determined by the duration of the illumination flash, enabling temporal resolutions down to 50 ns.

The experimental schematic is illustrated in Figure 3.2d. The CCD is run at a reduced frame rate, such that multiple device excitation cycles are captured; i.e. $\omega >>$ CCD frame rate. To avoid accumulated background heating of the DUT, the bias duty cycle is kept low, roughly 10 %. The small LED pulse widths should be 'on' with a minimum duty cycle of

approximately 1 %. Shorter power bursts may not be sustainable over multiple cycles and could damage the LED. The measurement at a minimum is run twice at a single bias: once to gain a specified snapshot of the active device, and again just before device turn-on in order to remove DC reflectivity term. This differential approach is closely related to the 4-bucket with square pulse modification. Bipolar measurements are necessary for Peltier and Joule signal extraction, after which the signal processing proceeds in exactly the same manner as previously described. Similarly, the total heating and cooling signatures are preserved in the mathematics and both are apparent in the temperature amplitude images. Again, there is no retrieval of phase information.

Implementation of this technique requires equipment capable of precision device and LED pulsing. The DUT is illuminated in very small bursts; consequently, significantly less light reaches the CCD than in the other methods. This degrades temperature and possibly spatial resolutions necessitating extensive averaging periods and higher applied biases. We utilize a pulsed voltage generator with less than 10 ns rise/fall times to achieve transient measurements of novel thermoelectric devices. Figure 3.3 exhibits a transient measurement of a 50 µm thick InGaAs energy conversion device with embedded ErAs nanoparticles (0.2 %). These thermal images show extreme current injection non-uniformity; in part due to a large processing defect near the current injection point and in part because of the highly elongated device design. The temporal images show that Joule heating takes time to reach the voltage sensing region at the far end of the mesa (RHS). At device turn-off, Peltier cooling disappears rapidly while the Joule signal is still traversing the device, finally decaying more than one millisecond later.

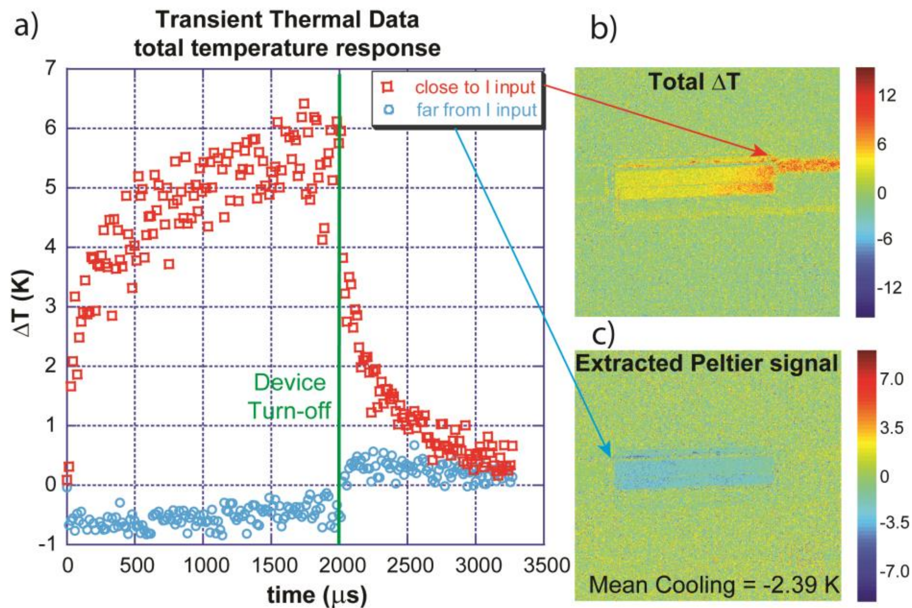

Figure 3.3: Transient thermoreflectance imaging of a 50 µm 0.2 % ErAs:InGaAs thermoelectric device. a) Comparison of transient data of the total temperature response in cooling mode at different locations on the device. Joule heating is shown to overwhelm Peltier cooling at varying times depending on the location along the length of the device. b) Thermoreflectance images taken with long phase delay of the total temperature response and c) extracted Peltier cooling. The data was taken in 15 µs steps.[50]

3.2 Applications of thermal mapping: Peltier and Joule surface thermal profiles for high temperature imaging

We developed high temperature thermal imaging as a tool to work in conjunction with the transient Harman method to quantify surface temperature of a thermoelectric device and thus enable the determination of the individual thermoelectric material properties in a single high temperature experiment. However, thermoreflectance imaging was instrumental throughout the optimization process of the experiment. With this technique, we were able to visualize the thermal and thus the electrical profiles of the thermoelectric devices and identify device and design flaws. A more detailed treatment is given in the chapter on the

transient Harman technique. Here, we present thermal images that depict instances of current injection non-uniformity (Figure 3.4) and three dimensional current spreading in the thermoelectric film.[51] In Figure 3.5, we demonstrate the utility of the 4-bucket/extended 4-bucket approach for acquisition of thermal images of larger devices. Each assisted with the optimization of the ZT Harman mask design.

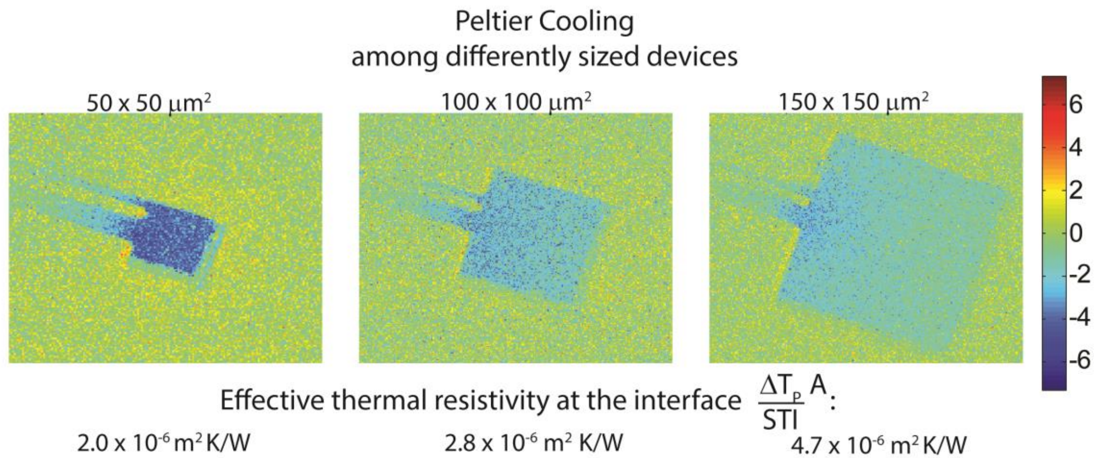

Figure 3.4: Comparison of thermal images of different device sizes in an early generation transient Harman device design. The thermoelectric device is a 50 µm thick InGaAlAs film with 0.6% ErAs nanoparticles randomly distributed. Total Peltier cooling does not follow the typical area dependence for 1-D heating in the film. Instead, the effective thermal resistivity (Peltier) that the heat source 'sees' varies with area, indicative of current spreading and an additional 1/√A dependency.

We apply a simplified fin model, in which heat propagates along a fin while being laterally evacuated through a coolant, to approximate the current distribution in the device contact pad. Ideally, current would spread uniformly in the contact pad and then flow one-dimensionally in the cross-plane direction. As the thermal images show, the Peltier thermal signal and thus the electrical current flows into the contact pad for a characteristic length,

L_C, before decaying exponentially into the layers beneath. We define L_C to in the contact pad accordingly:

$$L_C = \sqrt{\frac{\sigma_c d_c}{h_{eff}}} \tag{3.2.1}$$

where σ_c and d_c are the electrical conductivity and thickness of the fin, in this case the contact pad, respectively. h_{eff} is the effective 'current' transfer coefficient from the contact pad to the underlying device layers, analogous to heat flow between the cooling fin and the coolant medium; defined in this scenario as:

$$h_{eff} = \frac{1}{R_{eff} A_c}. \tag{3.2.2}$$

A_c is the contact area and R_{eff} is the effective electrical resistance the current 'sees' in the cross-plane direction. As the area of the device increases, the effective length should increase as well. Combining the two equations gives:

$$L_C = \sqrt{\frac{\sigma_c}{\sigma_{eff}}} d_{c.} \tag{3.2.3}$$

Thus, the problem of non-uniform current injection is governed by the ratio of the electrical conductivities of the contact pad and the effective device layers. The basic device structure, which determines σ_{eff}, is detailed in section 4.2 which includes a device schematic. For 50 µm 0.6 % ErAs:InGaAlAs depicted in Figure 3.4, an increase in metallization thickness of the contact, d_c in equation 3.2.3, from 2 µm to 6 µm served to increase the characteristic length and mitigate the issues illustrated in Figure 3.4.

However, even with an idealized case, it is difficult to achieve a reflectivity signal resolved above the background noise in the larger devices. To do so requires higher voltages to drive the circuit; consequently, we exploit the modified square pulse 4-bucket technique. Thermal images generated from both the 4-bucket method and the modified (differential) version of a 100 µm x 100 µm device with the most recent mask design are presented in Figure 3.5a,b. Figure 3.5c shows the corresponding temperature amplitudes plotted with respect to current, in order to compare the two techniques. The higher signal-to-noise ratio facilitated by the higher voltages reduces the necessary averaging time by a factor equal to the square of the ratio of the individual signals (for Peltier). In this example, an increase from 200 mA to 300 mA corresponds to a 3/2 increase in Peltier temperature magnitude which decreases the number of averaging cycles to 4/9 of the original cycling time needed to achieve the a given signal-to-noise ratio.

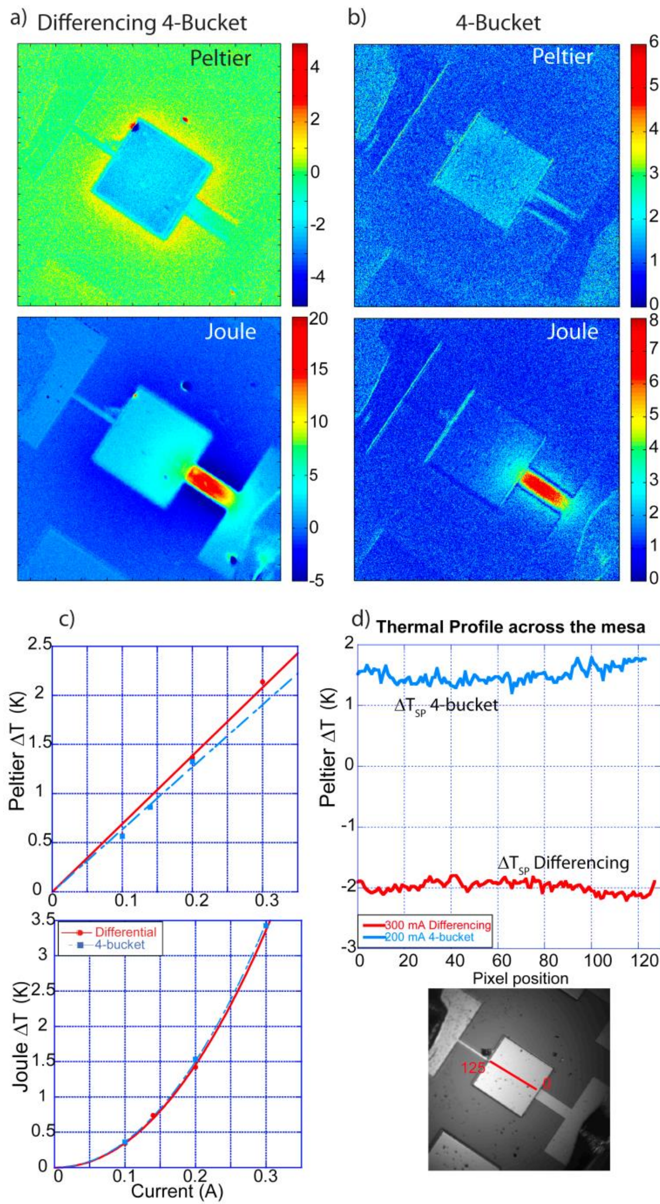

Figure 3.5: Thermal images portraying the functionality of the modified 4-bucket method, (a), compared with thermal images produced by the conventional 4-bucket approach, (b), of a 25 µm 0.2 % ErAs:InGaAs energy conversion device. The images in (a) are under 300 mA bias, while the images in (b) are taken at the function generator excitation limit, which corresponds to 200 mA in this experiment. Thermal phase images specify heating versus cooling in the 4-bucket approach. c) The absolute values of the amplitudes of the respective temperature signals of the two techniques. Linear and quadratic fittings of the Peltier and Joule signals, respectively, show that the two methods agree within 8 %. d) Cross-sectional thermal profiles of Peltier images indicating current spreads preferably toward the edges of the mesa.

Again, the thermal images exhibit non-uniform current injection into the thermoelectric film. However, in these devices it manifests as current crowding around the edges of the mesa, indicative of a high interface or film electrical resistance. Essentially, σ_{eff} is much too low. This effect is apparent in the Peltier images (Figure 3.5a,b), and is displayed as a cross sectional average displayed in Figure 3.5d. In depth diagnosis of these device imperfections is discussed in Chapter 4.

3.3 High temperature experimental calibration method

The information acquired in thermoreflectance experiments directly reveals relative temperature information across an active device surface. The absolute temperature change can be inferred, provided the C_{TR} has been calibrated for. However, the dependence of C_{TR} on temperature is difficult to predict; the reflectance of a sample is governed by the interplay of electronic bands and transitions, optical absorption, phonon/carrier interactions and light polarization, among other factors. Hence, C_{TR} may vary nonlinearly over a large temperature range. In this section, we describe a novel approach for C_{TR} calibration, ideally suited for measurements in a vacuum thermostat, and present the high temperature thermoreflectance coefficients for several metals commonly encountered in electronic devices. The effect of passivation on these metals is also examined. While the absolute values of the coefficient may vary with surface roughness and among experimental configurations, the temperature behavior provided here is directly applicable to other thermoreflectance investigations and is of general import.

Room temperature calibration measurements

The calibration process is essentially the converse procedure to the thermal imaging technique; the sample is externally modulated over a 'known' temperature range while thermal images of the passive device are recorded. It is relatively straightforward for room temperature measurements as long as the image magnification is relatively low so that surface expansion does not affect the image quality. In addition, the size of the sample in question should be of sufficient thermal mass to support surface temperature measurement by a micro-thermocouple, but still allows for responsive temperature cycling. In this

scenario, the DUT is usually mounted onto a Peltier cooling stage which is, in turn, mounted on a thermal heat sink. Thermal paste is applied to the DUT/stage interface to achieve best possible thermal contact. Similarly, the micro-thermocouple is adhered to the sample surface. If the specific DUT is too small to accommodate this then the temperature of the stage is measured and good thermal contact with the stage becomes crucial. Bipolar current is applied to the Peltier stage to provide both heating and cooling and the temperature of the stage plus DUT assembly is cycled quickly, ~0.1 to 10 Hz. The maximum temperature oscillation frequency is dictated by the thermal response times of the DUT and thermocouple; thus, smaller component geometries will thermalize much more quickly with the heating/cooling stage and afford the higher rate of temperature modulation. The reflectivity response is accumulated over many averaging cycles until a sufficiently small standard deviation of the signal is achieved and C_{TR} is obtained:

$$C_{TR} = \frac{\Delta \mathrm{R}}{\Delta T \cdot \mathrm{R}} \tag{3.3.1}$$

The measurement of $\Delta R/R$ could be accomplished with different excitation waveforms and varies between experiments. Commonly, a sinusoidal current is selected to drive the Peltier stage; thermal images and surface temperature can be simultaneously acquired over many points in the excitation cycle. The applied frequency must therefore be limited to the thermocouple temperature output. With this approach, it is also possible to utilize a fast Fourier transform to lock-into the reflectivity and temperature oscillations in the frequency domain. C_{TR} is then calculated as the slope of the two signals. This scheme can only run at very slow frequency (< 1 Hz), but offers higher resolution and is therefore useful for detection of small reflectivity fluctuations and is consequently best for samples with small

C_{TR}. A differential method employs a square voltage pulse excitation. In this implementation, the experimental apparatus is required to reach thermal equilibrium at the highest and lowest points in the temperature cycle and from this, $\Delta R/R$ and ΔT are calculated. Thus, a wait time is established after voltage turn-on and again at turn-off before data is recorded by the CCD. The basic calibration apparatus is shown in Figure 3.6.

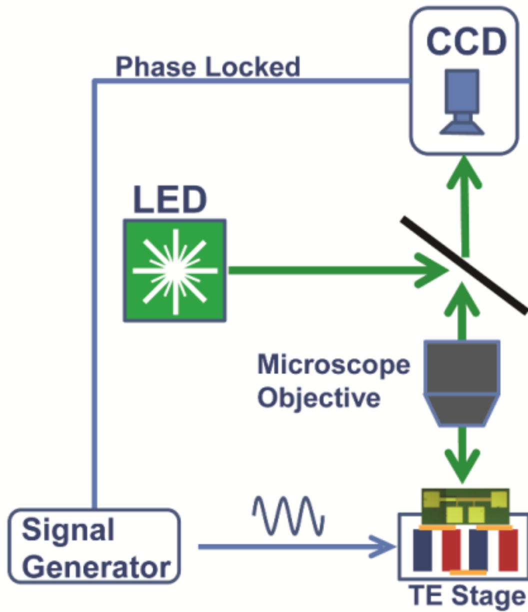

Figure 3.6: Schematic of the experimental set up for thermoreflectance coefficient calibration at room temperature.

The temperature magnitude must likewise be kept small in these measurements. This is not only because of the potential nonlinear behavior of C_{TR}, but has to do with minimizing thermal expansion in the direction of incident light. The linear shift in the cross-plane direction, Δd, is governed by the linear expansion coefficient (α_{TH}) of the layered device as:

$$\Delta d = \alpha_{TH} \Delta T d. \tag{3.3.2}$$

The overall thickness, *d*, of the calibration stage assembly, primarily the Peltier module, influences the extent of this effect. For small magnification objectives, <20x, and small temperature oscillation, thermal expansion will have a negligible impact. However, imaging microscopes with autofocusing capabilities are indispensable for higher magnification thermoreflectance.

High temperature calibration methodology

Error in thermoreflectance calibration is primarily determined by the accuracy of the temperature measurement of the sample surface. Thermocouples have the disadvantages of potentially causing damage to the sample, interfering with the optical line of sight, and may act as a thermal shunt if mounted on the sample surface. If positioned nearby, the thermocouple reading may not accurately reflect the temperature in the region of interest. All of these parasitic effects are exacerbated in a vacuum thermostat. Moreover, performing the thermoreflectance calibration methods as described above in the high temperature, high vacuum environment introduces further complexities into the measurement. Peltier modules have a limited operational temperature range, up to 450 K at best. The thermal capacitance of the sample stage/ambient heater in the chamber is large enough to be impractical for temperature modulation, but small enough to respond to thermal fluctuations imposed by an additional heater. Again, parasitic thermal signals and non-uniformity are intensified.

We developed a method that circumvents or mitigates most of these concerns and can be applied for electrically conductive surfaces.[52] The thermoreflectance coefficient is determined by combining the optical reflectivity imaging technique with the electrical 3ω

measurement of temperature, as they both have the same frequency response to temperature oscillations. The 3ω technique utilizes a small heater line with minimal thermal capacitance as both heater and thermometer, negating the need for a thermocouple. It is amenable for simultaneous thermal imaging with the 8-bucket method; only slight modification to the experimental circuit is required, as depicted in Figure 3.7.

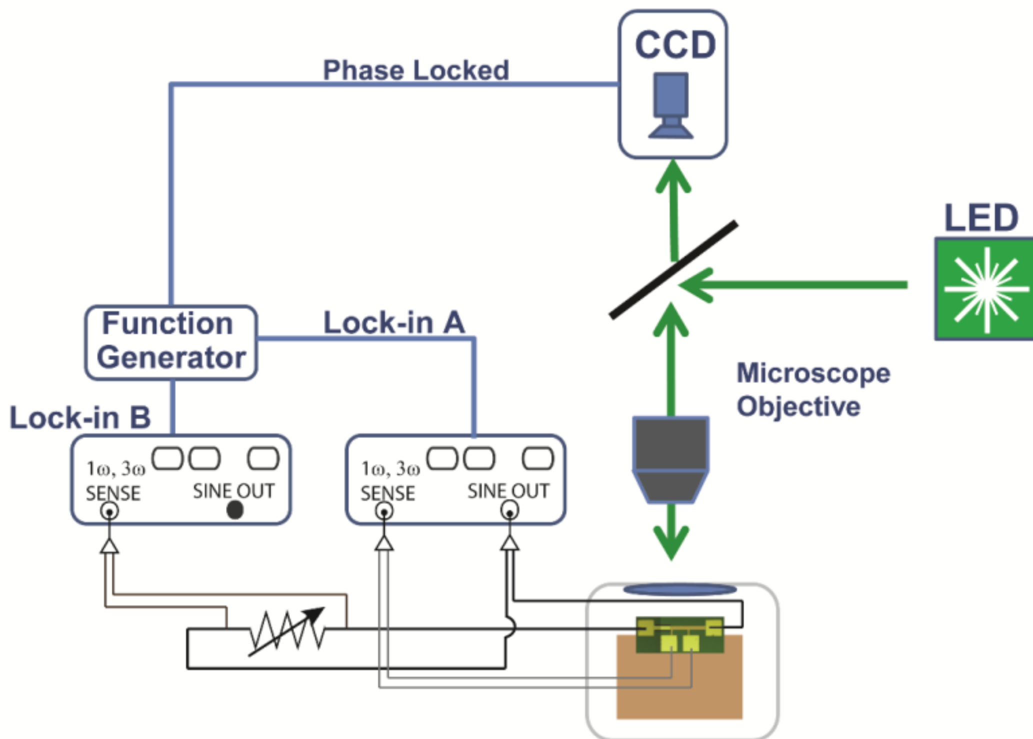

Figure 3.7: Experimental apparatus for thermoreflectance imaging with simultaneous 3ω measurement.

Three commonly employed metals are examined: gold, which is frequently used in III-V IC circuitry and material processing; platinum, for its robust and inert characteristics at high temperature; and aluminum, a common interconnect and transducer metal for time-domain

thermoreflectance measurements. The metals were individually evaporated with 100 nm thickness on a polished commercial silicon wafer with a 200 nm thick insulating oxide. Straight-line heaters 300 µm in length were patterned with four contact pads, in the typical 3ω configuration with multiple widths (8 µm and 24 µm). Finally, the surfaces of these micro-heaters were partially passivated with a SiN_x layer with 200 nm nominal thickness. Figure 3.8a shows an optical image of the sample surface, while Figure 3.8b exhibits the different sample layers.

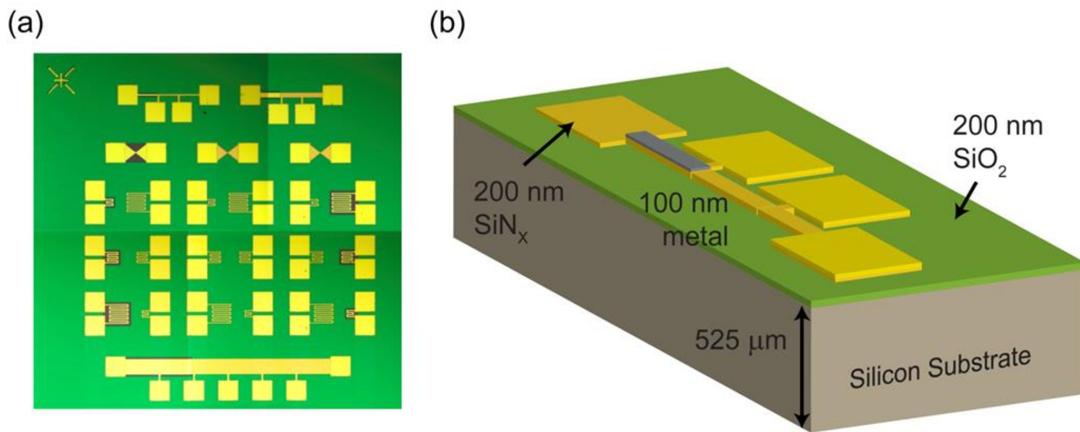

Figure 3.8: (a) Optical image of the sample with several heater designs for the different evaporated metals. (b) Diagram of the sample cross-section; the cross-plane thermal conductivity of this sample was measured to validate the use of the 3ω method and is presented in Section 2.2 of this manuscript.

The sample is mounted on the ambient heating stage inside the vacuum thermostat. We apply a non-offset sinusoidal voltage across the length of the heater at frequency ω = 2π·3.75 Hz, standard for 8-bucket thermoreflectance. As in the conventional 3ω measurement, the 1ω and 3ω voltage harmonics are detected by two lock-in amplifiers to determine $\Delta T_{2\omega}$ across the heater line relative to an external variable resistor; the function

generator is used to synchronize the lock-in clocks. The measurement proceeds as is customary for the two separate methods.

In the experiments for this work, oscillating voltage biases at various amplitudes were applied across the outer pads of the heater line, which roughly equated to current densities ranging from 30 to 50 mA/μm^2 in the gold and aluminum heater lines, and 20 to 30 mA/μm^2 in the platinum line. Both $\Delta T_{2\omega}$ and $\Delta R/R$ in all cases exhibited the expected quadratic behavior with respect to current (Figure 3.9). At each selected ambient temperature, measurements were performed after the thermostat attained thermal equilibrium, including measurements of the temperature coefficient of electrical resistance of the individual lines (α), as discussed in Section 2.2. However, the maximum temperature achievable for each sample varied as the devices displayed effects of degradation at elevated temperatures. The resistance of the heater line began to deviate from the expected linear trend with temperature at approximately 500 K for gold and aluminum, and above 700 K in the platinum heaters. The visual image became noticeably affected around 50 K higher. We believe this may be due to the metal annealing or incomplete photoresist residue removal during the lift off process. Optical images after device failure are presented in Figure 3.10.

One should note that the same 3ω analysis performed at higher frequencies (>500 Hz) can be used to extract the substrate thermal conductivity, as discussed in Chapter 2. Since the silicon thermal conductivity is known, this serves as further verification of the temperature calibration method. These results are shown in Figure 2.7.

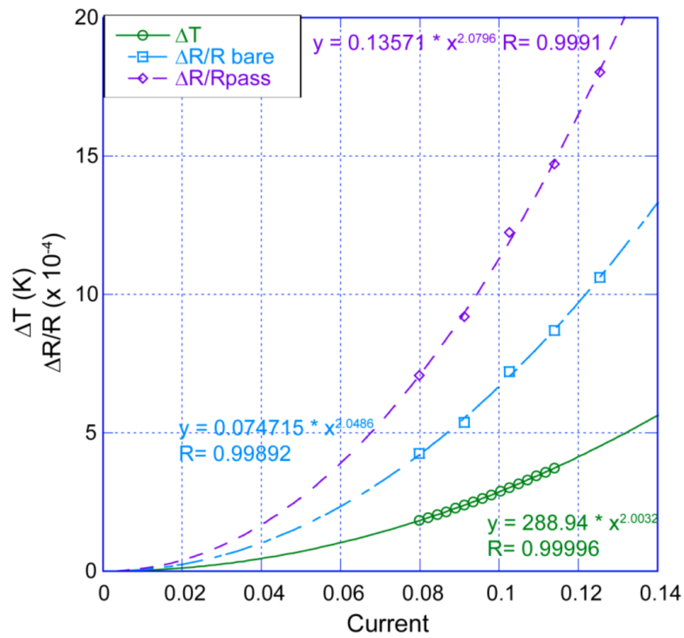

Figure 3.9: The acquired amplitude of the temperature oscillations and the relative reflectivity of a gold heater line with and without passivation, plotted with respect to the applied current. Both signals illustrate a quadratic dependence on current.

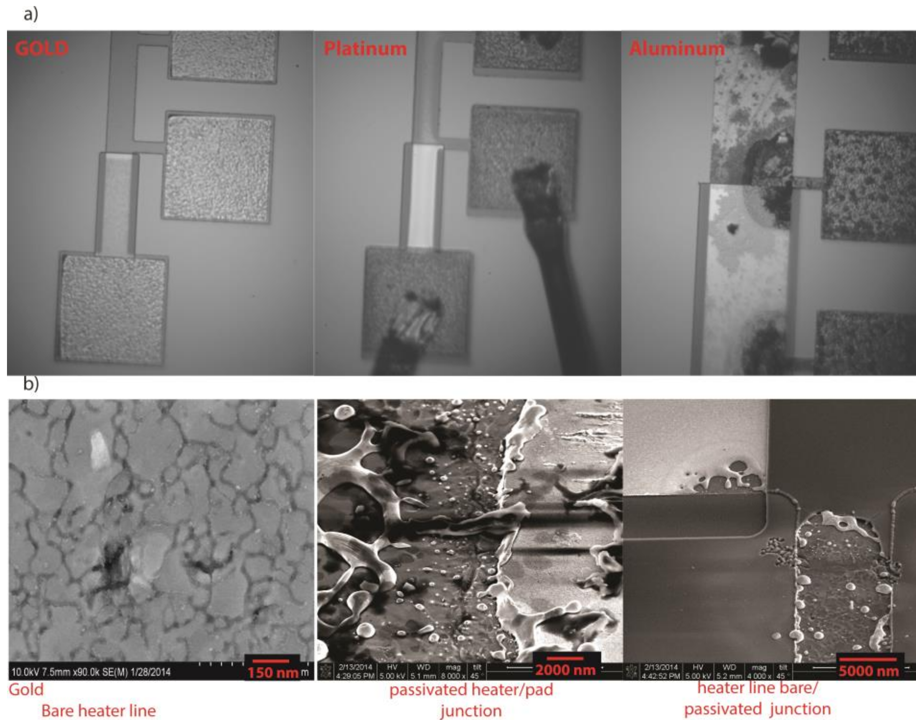

Figure 3.10: a) Optical greyscale images of the gold, aluminum and platinum heater lines in different areas on the same chip after experiencing temperatures above 800 K. These images were taken under 530 nm illumination. b) SEM images in different locations on the gold heater line.

For the optical portion of the experiment, we used a 20x objective with a 0.25 numerical aperture. The illumination wavelengths were selected near absorption peaks in the optical spectra for each metal to optimize their specific thermoreflectance response. Table 3.1 shows the wavelengths designated for each metal and their measured C_{TR} at room temperature. These results follow the expected spectral dependences for each metal, as found in literature. We plot this experimental data for the metals at the specific wavelengths examined in this work in comparison to spectral data given in references[53,54,55] in Figure 3.11.

Table 3.0.1: Summary of the at room temperature thermoreflectance coefficients obtained at the specific illumination wavelengths utilized in this work.

Room temperature C_{TR} of metal heater lines (10^{-4} K^{-1})				
Heater Line Metal	530 nm	470 nm	455 nm	780 nm
Gold	-2.36	2.59	1.35	-
Platinum	-0.58	-0.364	-	-
Aluminum	-	-	-	1.14

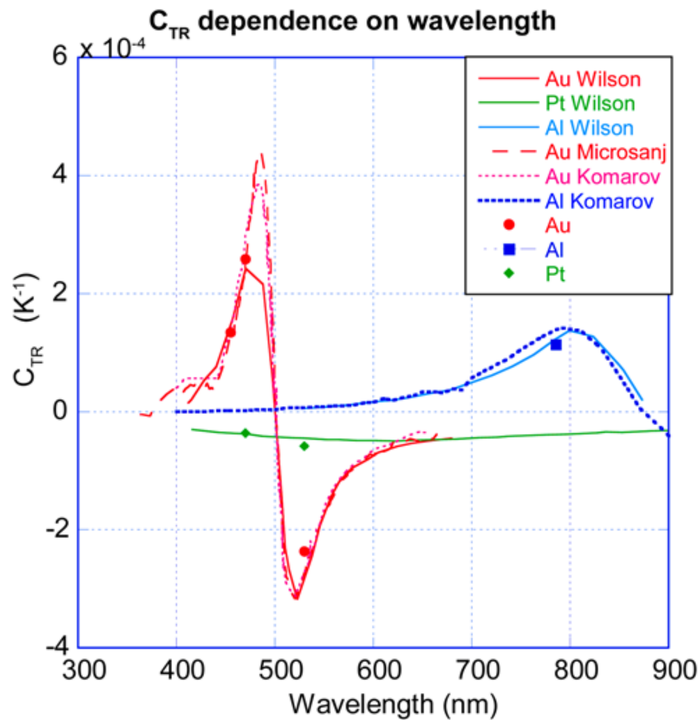

Figure 3.11: Experimentally measured C_{TR} for gold, aluminum and platinum displayed with respect to illumination wavelength. The spectral behavior of the coefficient is from literature, while the individual values are from this work.

Gold

For gold, we examine the behavior of C_{TR} under 455, 470, and 530 nm illumination from room temperature to 500K, above which, quality of the metal deteriorated substantially. We expect the temperature signal in the thermoreflectance images to be solely derived from Joule heating generated in the metal line; this is confirmed by examining the 1st harmonic signal in the Peltier image (Figure 3.12). The lack of signal demonstrates the reliability of the technique; parasitic thermal offsets were absent. From this point on, thermal images presented in this chapter exhibit the 2nd harmonic (Joule) signal only.

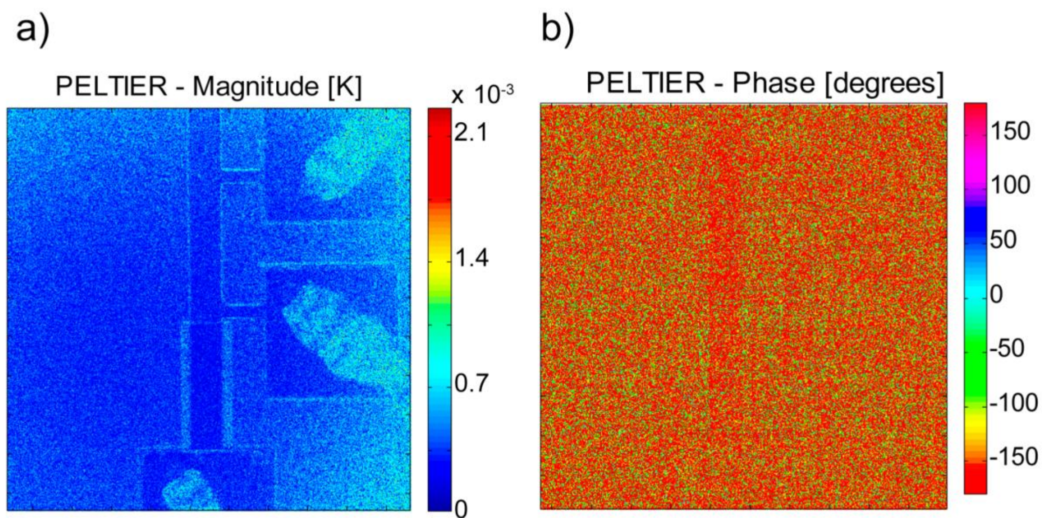

Figure 3.12: Peltier magnitude (a) and phase (b) images of the active gold heater line at room temperature. No 1st harmonic temperature signature is present in these images.

Thermal and optical images taken under the three different wavelengths at room temperature are presented in Figure 3.13. Figure 3.13b displays the magnitude of the relative reflectivity as a result of Joule heating generated in the heater line. The temperature is uniform along the heater line, except in areas near the current injection

pads. For the given ΔT, bare gold illuminated at 530 nm has the highest thermoreflectance response, followed by 470 nm and then 455 nm. The reflectivity signal is significantly enhanced in the passivated region at 530 nm, but is slightly diminished at 470 nm with almost no change for the 455 nm data, relative to bare Au. The relative phases of these signals are displayed in Figure 3.13c. Since no spurious harmonics are present and Joule is always 'heating', the change in phase indicates a change in sign of C_{TR}. Therefore, 530nm unpassivated Au has a negative C_{TR}; i.e. for a given increase in temperature, the relative reflectivity signal is dampened. Both 470 nm and 455 nm exhibit positive phase and thus a positive C_{TR}, as expected.

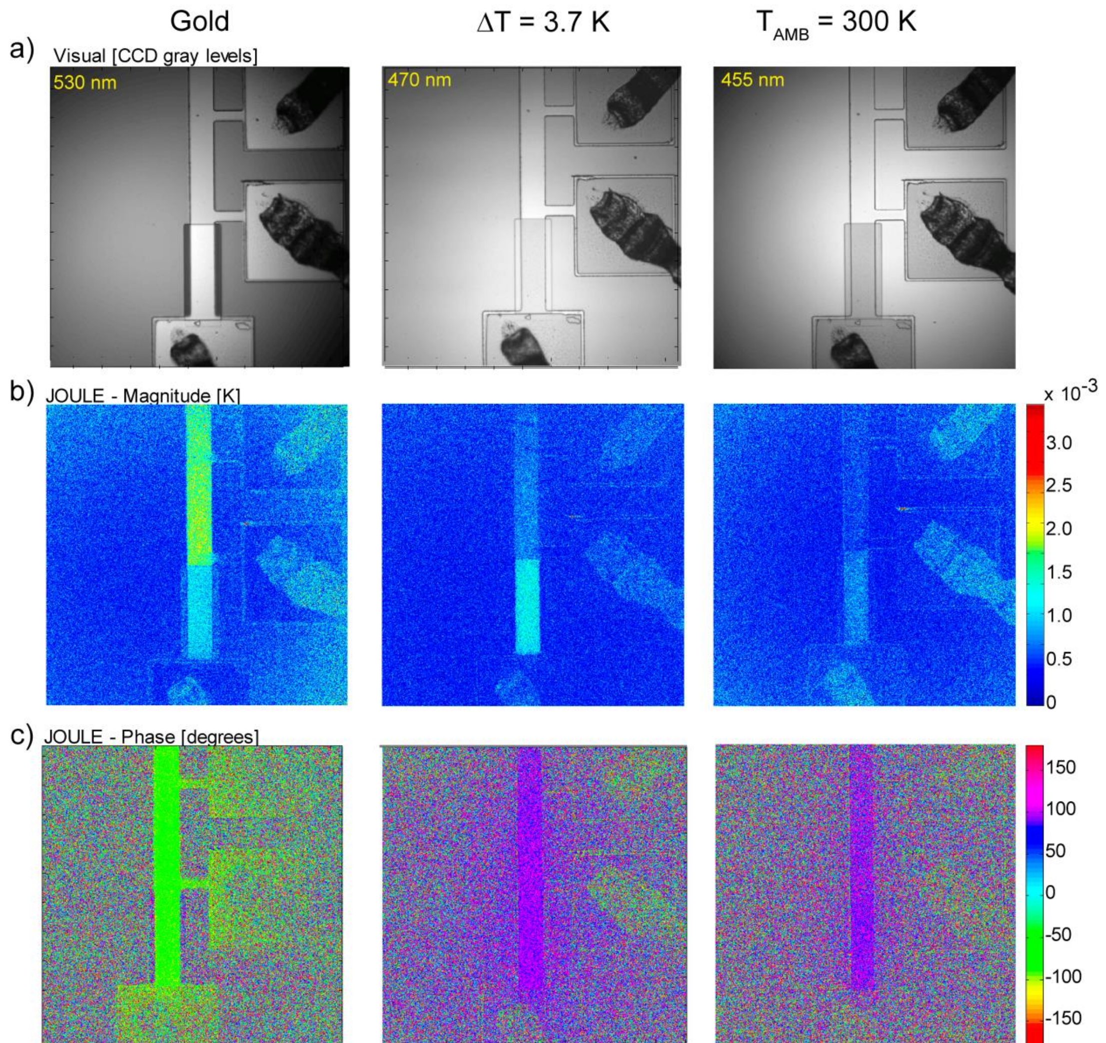

Figure 3.13: The change in the reflectivity of a gold heater line under 530 nm, 470 nm, and 455 nm illuminations, in response to temperature oscillations with amplitude 3.7 K. a) exhibits the optical images under the three wavelengths. b) and c) depict the magnitude and phase of *ΔR/R,* respectively.

The average $\Delta T_{2\omega}$ sensed in the 24 µm wide Au heater line generated from the maximum applied voltage varied from 3.7 K to 6.0 K over the temperature range. When normalized for current, both the amplitudes of the relative reflectivity and temperature modulations increased almost linearly with temperature (shown in Figure 3.14), though not at the same

rate. To determine C_{TR}, we simply divide the relative reflectivity signals by the calculated $\Delta T_{2\omega}$. The coefficients of thermoreflectance for both bare (Figure 3.15a) and passivated (Figure 3.15b) gold are plotted up to 500 K. There are distinct trends in the coefficient for each wavelength which are shown to be slightly altered by the presence of passivation. The total error in the measurement is calculated considering the dominant error sources: standard deviation in the average signal across the heater line in the reflectance images, the difference in the 1ω voltage drop across the heater line and external resistor, and the error in the linear fitting of α. Since the quality of the heater deteriorated at higher temperatures, error in both α and the resistances contributed significantly.

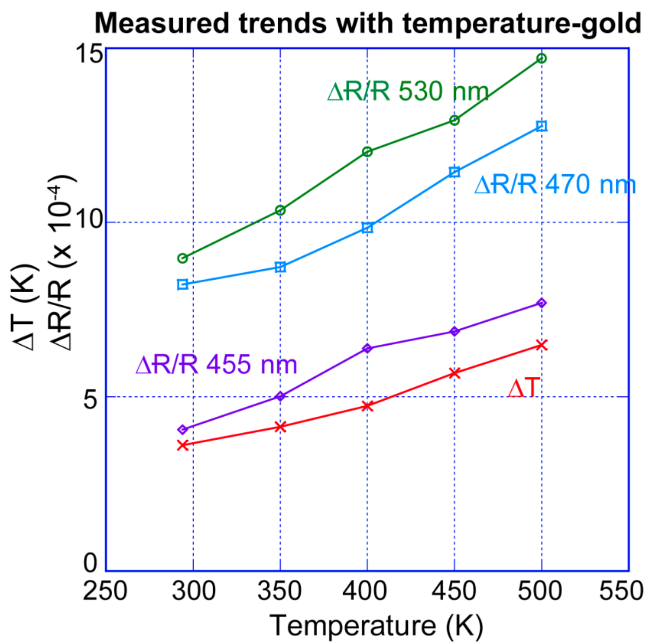

Figure 3.14: The temperature trends of *ΔR/R* measured by thermoreflectance imaging and $\Delta T_{2\omega}$ calculated by 3ω method.

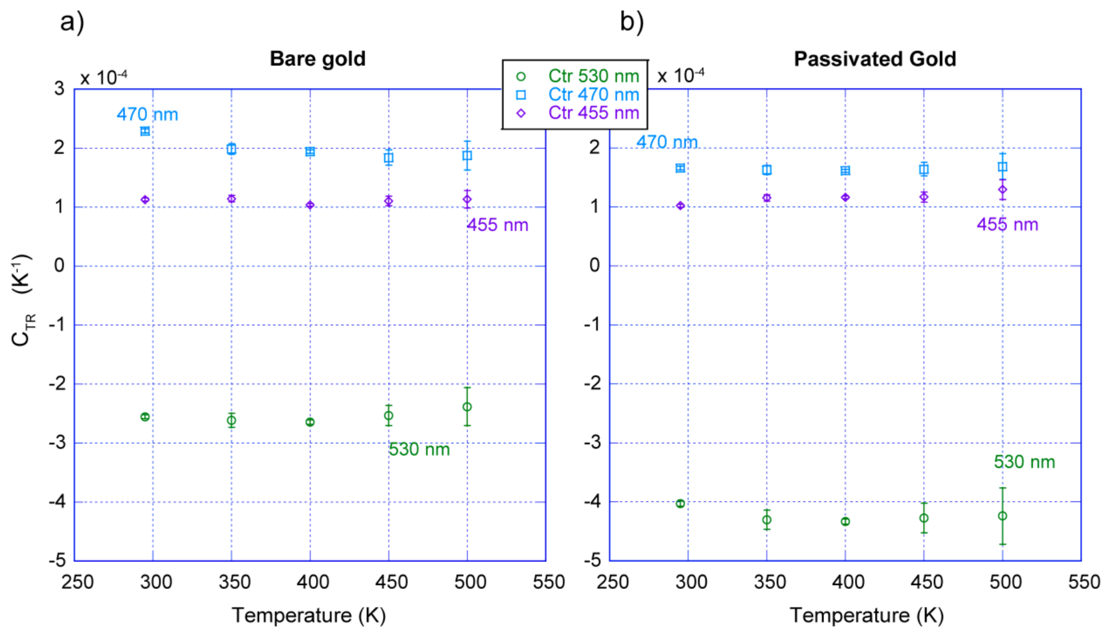

Figure 3.15: C_{TR} behavior with temperature for bare gold (a) and gold with a 200 nm thick layer of SiN_x (b). The maximum change in the coefficient is exhibited under 470 nm illumination; ~20 % over the temperature range, or approximately 0.20 x 10^{-4} per 100 K.

In gold, there is a direct transition from the upper states of the d-band to the Fermi level, with the band edge occurring near 520 nm.[56,57] This corresponds to structure in the spectrum of the imaginary component of the dielectric function affecting reflectance. Temperature effects on the band structure are dominated by those induced by thermal expansion of the crystal lattice, which serves to shift and broaden the absorption band edge.[56-58] These energy shifts can be considered linear for the small changes in lattice spacing experienced in this temperature range, so we assume an approximately linear shift of the reflectivity peak with temperature. However, for this particular transition in gold, temperature induced broadening of the Fermi distribution also plays an appreciable role. The change in the absorption peak in the dielectric spectrum of gold near 500 nm has been

shown in the literature to shift toward lower energies at rates ranging from 0.03 nm[56] to 0.12 nm[59] per K. Our measured C_{TR} for bare gold at 530 nm exhibits a maximum near 400 K. We roughly estimate the rate of shift with wavelength of the reflectivity peak to be ~0.1 nm/K based on the room temperature spectra maximum (or minimum, as it is negative), which is in reasonable agreement with the literature if we assume similar shifting and broadening. The C_{TR} determined for 470 nm and 455 nm show an initial decrease with temperature, consistent with a spectral shift to lower energies. The overall behavior of which are anticipated by the slope of the peak in the spectrum for the reflectance of Au (refer to Figure 3.18). This is a rough estimate of the expected shift in energy; values are influenced by strain experienced by the metal film as a result of coefficient of thermal expansion mismatch with the substrate, which will further influence band structure in dielectric spectra.

Platinum

The platinum heater line remained relatively stable for higher temperature measurements, compared to the other metals investigated. Figure 3.16 displays the thermoreflectance images at 470 nm and 530 nm taken at 700 K. The phase images show a negative reflectivity response of bare platinum to temperature modulation. However, the passivation effectively turned C_{TR} positive under 470 nm illumination, while enhancing the negative response of the 530 nm signal. This is consistent with the behavior of the gold heater line; passivation at 470 nm has a diminishing effect. The temperature dependent C_{TR} is plotted in Figure 3.17a for bare platinum and Figure 3.17b for platinum with passivation. Overall, the sensitivity of reflectivity increases with temperature.

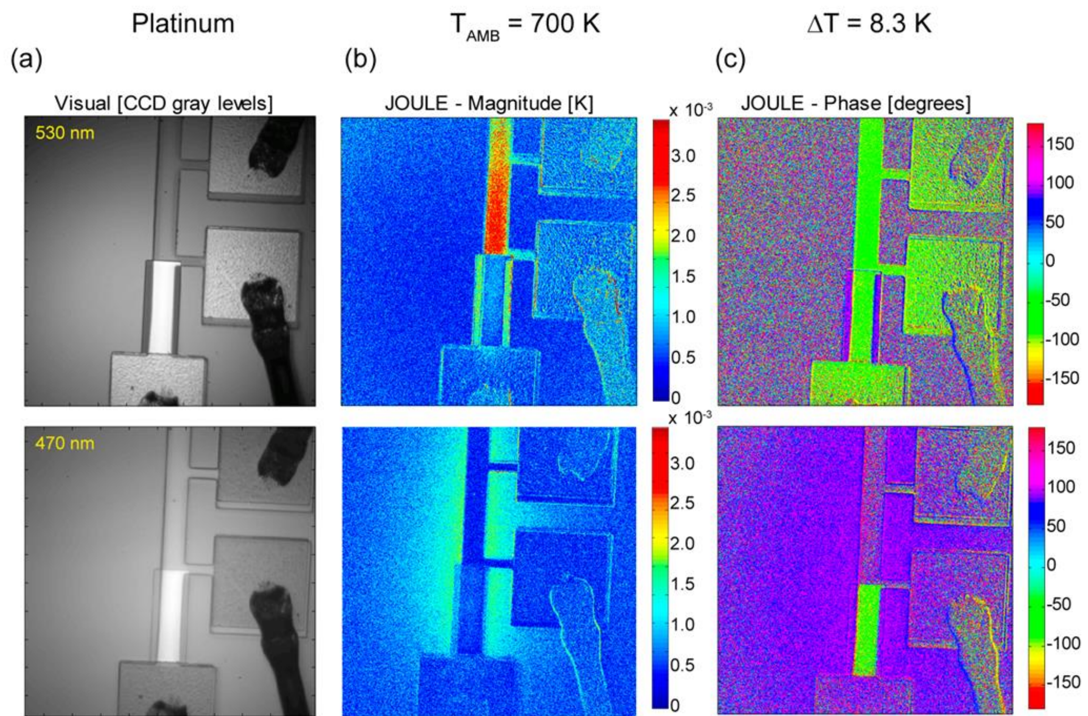

Figure 3.16: Thermal images of the platinum heater line at 700 K for $\Delta T_{2\omega}$ = 8.3 K. The phase images show that the sign of the thermoreflectance coefficient flips with passivation under 470 nm illumination.

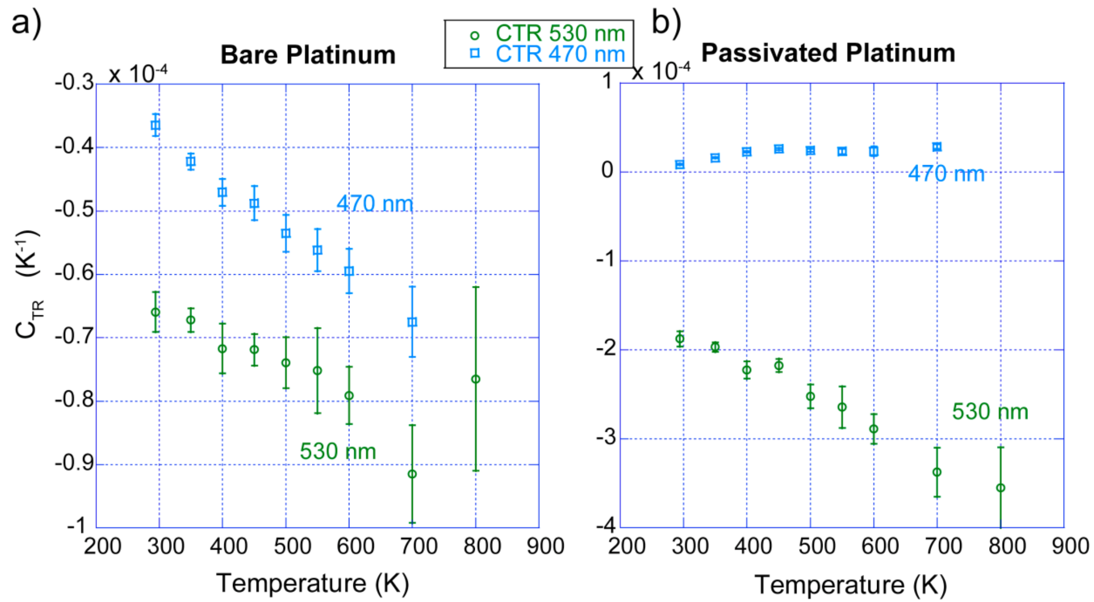

Figure 3.17: C_{TR} of bare platinum (a) and passivated platinum (b) up to 800 K. The larger error bars in the bare platinum data at the higher temperatures is due to material degradation with temperature.

Aluminum

There is a well-known interband transition near 800 nm illumination,[58] which corresponds to the only substantial absorption peak near the visible spectrum suitable for thermoreflectance imaging. In this study, we examined the aluminum heater line under 780 nm illumination, for applied biases similar to that of the gold heater line due to their comparable electrical resistivities. $\Delta T_{2\omega}$ also varied similarly for the maximum applied voltage; from 3.7 K at room temperature to 8.1 K at 600 K. The reflectivity response of aluminum is positive for both bare and passivated regions, corresponding to a positive C_{TR} which decreases over the temperature range (Figure 3.18). The passivation layer at this wavelength had the overall effect of decreasing the thermoreflectance response, more so with increasing temperatures. The C_{TR} values for bare and passivated aluminum heater line

are plotted in Figure 3.19. The temperature response of interband absorption in aluminum is characterized by broadening and shifting of the peak toward lower energy, largely induced by lattice volume dependence of the pseudopotential.[58,60] Such a shift would decrease the magnitude of C_{TR} (Figure 3.18).The higher rate of change in C_{TR} with temperature is attributed to the larger thermal expansion coefficient of aluminum relative to the other metals.

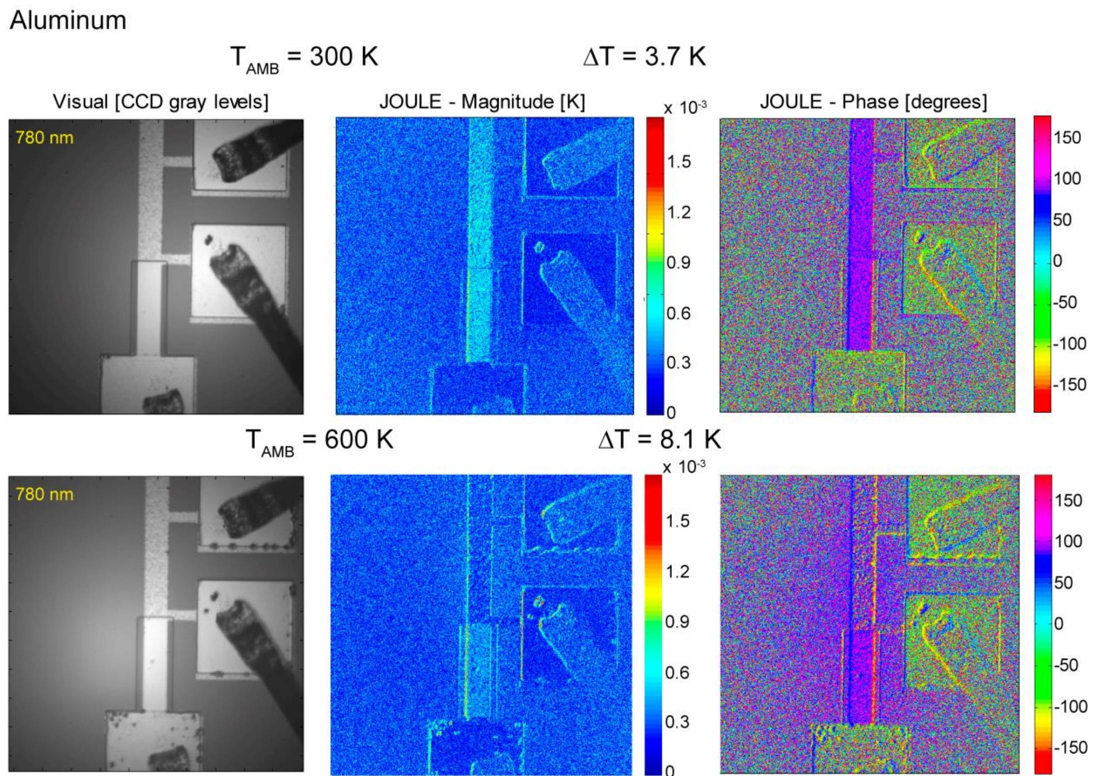

Figure 3.18: Comparison of the change in reflectivity due to Joule heating of 3.7 K at room temperature and 8.1 K at 600 K. Damage to the heater surface is apparent in the optical image at 600 K. In spite of more significant heating at 600 K, the thermoreflectance image exhibits a reduced reflectance as a result of the smaller C_{TR} at the higher temperature.

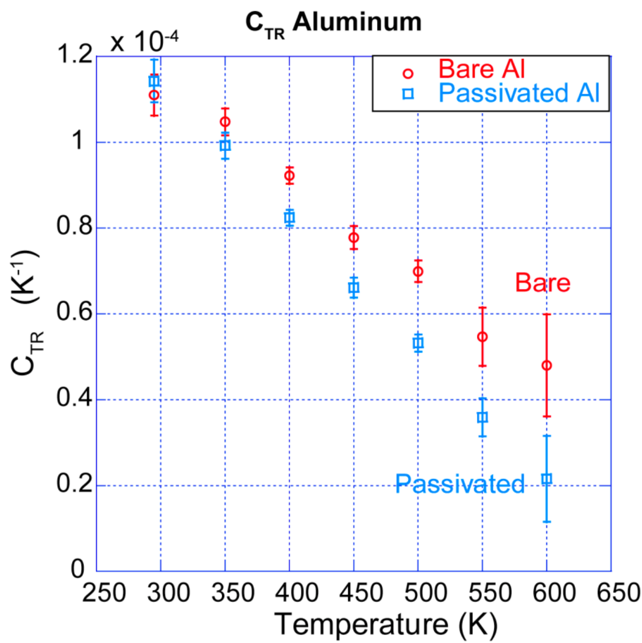

Figure 3.19: The trend of the coefficient of thermoreflectance for bare and passivated aluminum. C_{TR} shifts at a rate of about 0.22 x 10^{-4} per 100 K temperature change for bare aluminum, which is quite substantial considering the small values of C_{TR}.

Equations governing temperature dependence and the effect of passivation

Three main physical processes determine the optical properties of a material, namely electronic transitions, free carrier effects, and charge carrier-phonon interactions. These processes and their interactions are concisely represented in Figure 3.20 (adapted from reference [61]). Thermoreflectance microscopy measures the thermal behavior of these effects as they manifest in the response of the complex dielectric function, $\boldsymbol{\varepsilon}(E) = \varepsilon_1 - \boldsymbol{i}\, \varepsilon_2$, to an oscillating thermal field. ε_1 and ε_2 are the real and imaginary components, respectively. The dielectric constant is a function of energy, which implies an inherent dependence on the wavelength of incident light (E=hc/λ) and temperature of the material. Reflectivity measurements are generally associated with the complex index of refraction of a material,

$\mathbf{n}$=n- $\boldsymbol{i}$ k. The real component, n, describes the relative velocity of light in a material and the imaginary term, k, is the extinction coefficient and depicts absorption of light. Maxwell's equations give the relation between the dielectric constant and the complex index of refraction:

$$\boldsymbol{\varepsilon} = \boldsymbol{n}^2 = (n^2 - k^2) - \boldsymbol{i}2nk. \tag{3.3.1}$$

The amplitude of the reflected light, r, of normal incidence on a single surface is given as:

$$r_{0\mathrm{m}} = \frac{\boldsymbol{n_0} - \boldsymbol{n_\mathrm{m}}}{\boldsymbol{n_0} + \boldsymbol{n_\mathrm{m}}}, \tag{3.3.2}$$

where $\mathbf{n}_0$ is the complex index of refraction of the incident light (medium 0) and $\mathbf{n}_\mathrm{m}$ is the complex index of the reflecting material. In practice, incident light travels through a non-absorbing medium, such as air, and the imaginary part of $\mathbf{n}_0$ can be neglected. The measured reflectivity ($\mathrm{R} = r \cdot r^*$) for a single interface is then:

$$\mathrm{R}_{01} = \frac{(n_0 - n_m)^2 + k_m^2}{(n_0 + n_m)^2 + k_m^2}. \tag{3.3.3}$$

The thermoreflectance coefficient is the relative reflected intensity change resulting from a small temperature oscillation in the reflecting medium, and can be obtained from the temperature derivative of Equation 3.3.3 normalized for baseline reflectivity. Thus, in an optical system with a single interface $C_{TR,bare}$ is given as:

$$C_{TR,bare} = \frac{4n_0(n_m^2 - n_0^2 - k_m^2)\frac{\partial n_m}{\partial T} + 8n_0 n_m k_m \frac{\partial k_m}{\partial T}}{((n_0 + n_m)^2 + k_m^2)((n_0 - n_m)^2 + k_m^2)}. \tag{3.3.4}$$

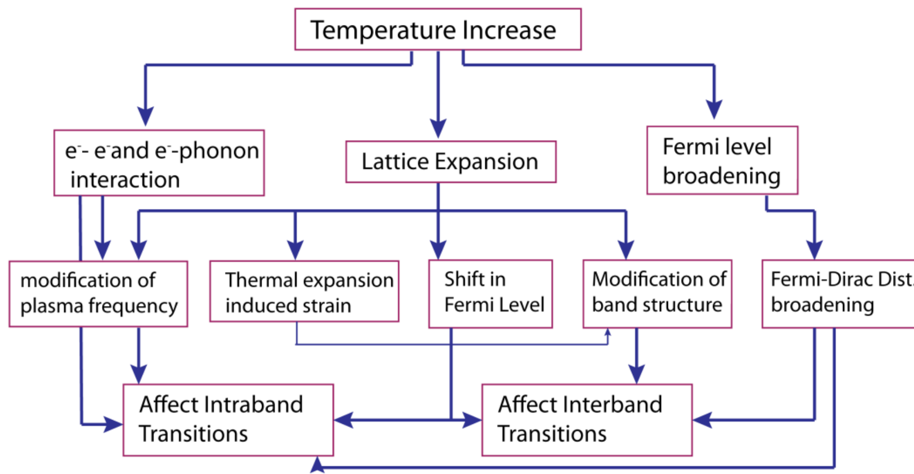

Figure 3.20: Schematic of the effect of a temperature increase on the physical processes in a bulk metal which can lead to modification of the optical properties. Image adapted from Ref. 61.

Studies have shown significant changes in the thermo-optic coefficients, $\frac{\partial n}{\partial T}, \frac{\partial k}{\partial T}$, of noble metals over the temperature range of this experiment, especially for transitions near the Fermi level.[62] These effects display as more pronounced dispersion compared to the influence of thermal expansion specific to the material under test, including sign changes in the thermo-optic coefficients. Each term in Equation 3.3.4 and the corresponding temperature dependencies must be empirically determined for individual material systems.

The addition of a transparent encapsulation layer complicates the analysis somewhat; in these measurements, incident light is reflected off both the air-to-film and film-to-metal interfaces. This becomes a three layer problem, where reflected light off the two interfaces constructively or destructively combines (due to phase changes) depending on the film layer thickness. If the passivation layer is of suitable thickness to be considered completely

transparent, the index of the film, n_f is real, as is the amplitude of reflection of light solely due to the air-to-film interface:

$$r_{0\mathrm{f}} = \frac{n_0 - n_\mathrm{f}}{n_0 + n_\mathrm{f}}. \tag{3.3.5}$$

The total amplitude of the reflected light, r_{Tot}, now has phase change and film contributions, in addition to r_{0m}, expressed as:

$$r_{\mathrm{Tot}} = \frac{r_{0\mathrm{f}} + r_{\mathrm{fm}} e^{-i2\beta}}{1 + r_{0\mathrm{f}}\, r_{\mathrm{fm}} e^{-i2\beta}}, \tag{3.3.6}$$

where r_{fm} represents the reflected amplitude off the film-metal interface. The term β governs the phase change of the reflected light at the sample surface: $\beta = 2\pi n_f d_f/\lambda$, where d_f is the passivation layer thickness and λ is the wavelength of incident light. The total intensity of reflected light for the three layer system, R_{Tot}, is thus:

$$\mathrm{R}_{\mathrm{Tot}} = r_{Tot} r_{Tot}^{*} = \frac{g_f^2 + g_m^2 + h_m^2 + 2g_f g_m \cos[2\beta] + 2g_f h_m \sin[2\beta]}{1 + g_f^2 g_m^2 + g_f^2 h_m^2 + 2g_f g_m \cos[2\beta] + 2g_f h_m \sin[2\beta]} \tag{3.3.7}$$

$$g_f = \frac{n_0^2 - n_f^2}{(n_0 + n_f)^2}; \qquad g_m = \frac{n_f^2 - n_m^2 - k_m^2}{(n_f + n_m)^2 + k_m^2}; \qquad h_m = \frac{2n_f k_m}{(n_f + n_m)^2 + k_m^2};$$

The terms g_f, g_m, and h_m are introduced following reference[63] to reduce the complexity of the expression. The cyclic nature of the trigonometric terms indicates the expected oscillation in reflectivity with respect to passivation layer thickness. Figure 3.21 displays the calculated changes in total reflectivity due to variations in the passivation layer thickness for the experimental devices (Au, Al, and Pt) used for thermoreflectance coefficient calibration measurements. Room temperature optical data is taken from the literature.[64,65] The grey

line depicts the thickness of the SiNx layer of the samples: d_f = 200 nm.

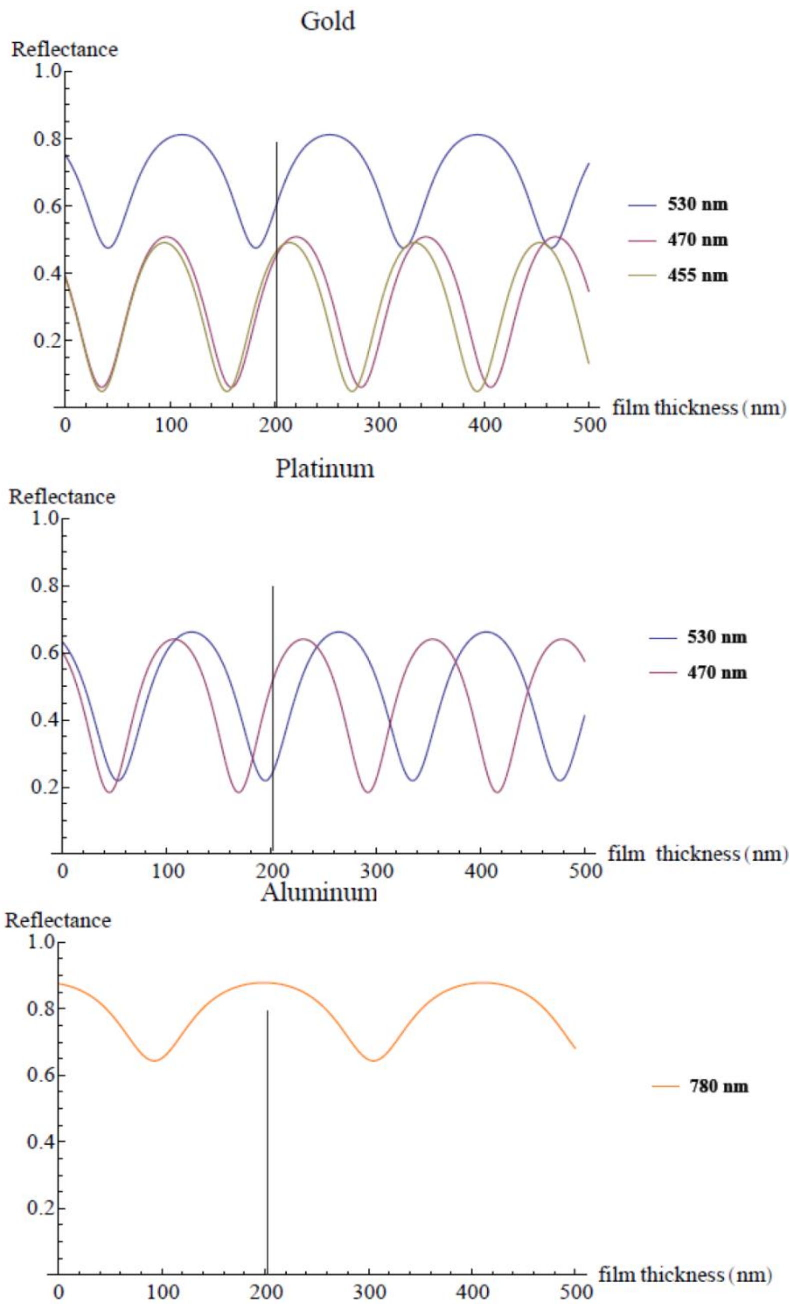

Figure 3.21: The reflectivity of light of the different measurement wavelengths plotted as a function of passivation layer thickness. The grey line indicates the actual measured SiN_x thickness.

However, it is difficult to predict the effect of the addition of the passivation layer on C_{TR} from these viewgraphs, other than it too will have a cyclic dependence on the layer thickness. By definition, the coefficient of thermoreflectance quantifies the effective thermo-optic behavior of a material system and is therefore governed by the individual material coefficients constituting the layered sample: $\frac{\partial n_f}{\partial T}, \frac{\partial n_m}{\partial T}, \frac{\partial k_m}{\partial T}$. As mentioned previously, these coefficients are only available phenomenologically from spectral data acquired at various ambient temperatures.

Assuming a slight temperature dependence of the SiNx film with a linear expansion coefficient of 3.27 E-6 and that the linearized thermo-optic coefficients are valid for small temperature changes, we determine the local $\frac{\partial n_m}{\partial T}, \frac{\partial k_m}{\partial T}$ values for the metals using the reflectance data measured at the various ambient temperatures of this experiment. Thus, the influence of the passivation layer on the thermoreflectance coefficient can be calculated using the above equations and is shown in Figure 3.22 for gold and platinum at room temperature. Again, the grey line represents the actual SiNx layer thickness. $\frac{\partial n_f}{\partial T}$ was found to be on the order of 10^{-5} for SiNx, which is reasonable compared to literature.[64,66] However, in the calculations over the temperature range, we used an effective $\frac{\partial n_f}{\partial T}$ that incorporates a contribution of the thermostat viewport. This had the overall effect of slightly reducing the temperature dependence of the index of refraction of SiN_x. The calculated room temperature thermo-optic coefficients match quite well with data from reference 53. Figures 3.21 and 3.22 demonstrate that the reflectance signal and thus the C_{TR} of a material

may be optimized through selective deposition of passivation thicknesses, or by utilizing incident illumination coincident with a maximum.

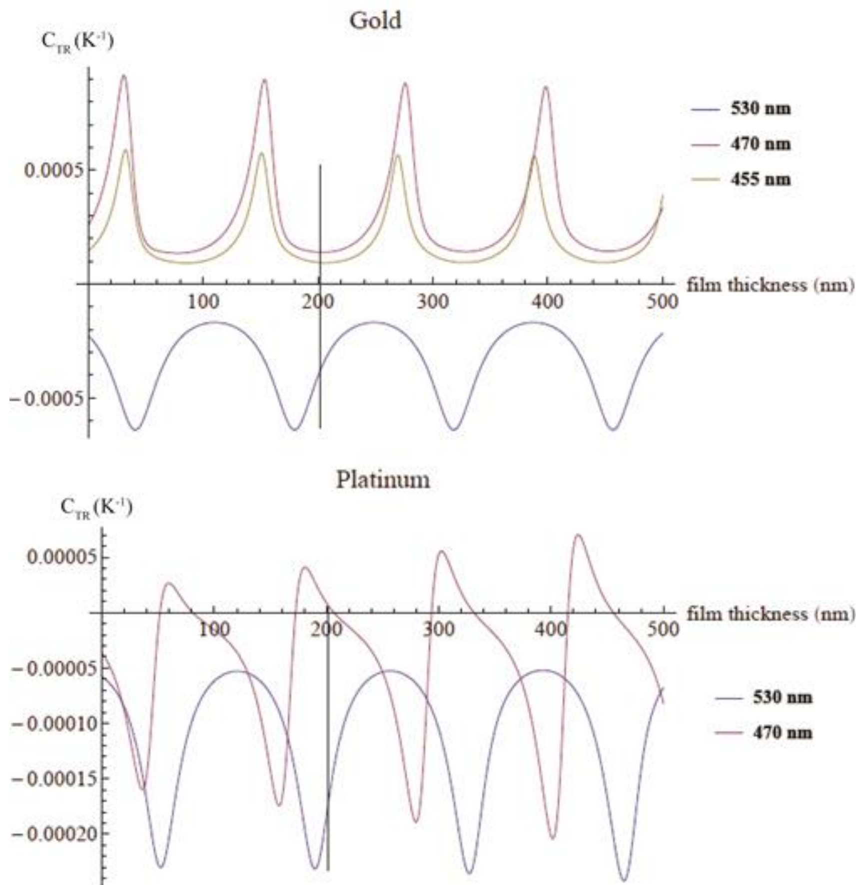

Figure 3.22: The thermoreflectance coefficients of platinum and gold under different illumination wavelengths plotted with respect to the passivation layer thickness. This is accurate near room temperature. The vertical line indicates the nominal thickness of the SiN_x layer of the experimental devices.

Chapter 4 Transient Harman technique for direct measurement of the cross-plane figure of merit of thin films at high temperatures

The transient Harman method[67,68] is a simple approach used to obtain the cross-plane ZT of a thermoelectric material in a single measurement; thus, its high temperature implementation is desirable to reduce error accumulation in ZT associated with three separate measurements. The technique is based on the detection of the ratio of resistive and Seebeck voltages created by electrically induced heating in the time domain. Not only does it necessitate high temporal resolution, it also requires rigorous coincidence of the thermal and electrical flow paths in the device to attain a high degree of measurement accuracy. The conventional transient Harman technique has been successfully employed in bulk material systems,[69] however, these criteria are difficult to achieve in thin film devices. Both electrical and thermal profiles lose uniformity at the sample surface and within the film itself due to its decreased aspect ratio, while thermal transients are very fast (~10 ns to 1 ms) and difficult to resolve above measurement noise. These effects are further exacerbated by contributions from spurious thermal signals, including interface Joule heating as well as thermal leakage through probe leads, both of which are substantial relative to thermal signature of a film at the micrometer scale. Similarly, the electrical measurement can become convoluted. Parasitic electrical resistances, i.e. substrate and contact resistances, are on the order of or greater than the actual device resistance and thus constitute a larger proportion of the measured voltage. Analytical modeling and thermal mapping of the electrical and thermal distributions in a transient Harman experimental

device have shown the detrimental impact of these effects[70,71,72,73,74] and help identify an approach to minimize them; though, little work has been published applying transient measurements to thin films.[73-75] Previously, Singh *et al*.[73] demonstrated the first thin film transient Harman measurement of ZT at room temperature.

In this chapter, we show how the transient Harman technique utilized in conjunction with thermoreflectance imaging can not only extract the individual material parameters and ZT of a thin-film energy conversion device, but also quantify parasitic effects. Furthermore, the optimization of experimental devices designed to mitigate the influence of parasitic signals during the measurement is discussed. The results of the high temperature characterization of 25 μm thick InGaAs thin film with embedded ErAs (0.2 %) nanoparticles are presented.

4.1 Theory and measurement requirements

The technique is simply a measurement of the voltage response of a thermoelectric material to a square-pulse bias. The slower response time of the thermally induced voltages is exploited to distinguish between Seebeck (V_S) and resistive voltages (V_R).[67] A bipolar measurement is required to extract the Peltier (V_{SP}) and Joule (V_{SJ}) components of the Seebeck voltage since the Peltier signal flips sign with current polarity, while Joule is always heating.[68] Therefore, ZT is obtained in one direct measurement: $ZT=V_{SP}/V_R$.

The total heat (Q) transported per unit time in a thermoelectric device in response to an applied bias is:

$$Q = STI - ½I^2R - \mathrm{K}\Delta T \tag{4.1.1}$$

where I is the applied current and K is the thermal conductance. In this equation, heat and current flow are taken with reference to the cold side of the thermoelectric device and hence T is the temperature at the cold side. The total voltage (V_T) developed across the device is the sum of the electrical voltage drop and the Seebeck potential generated from the temperature difference:

$$V_T = V_S + V_R = S\Delta T + IR \tag{4.1.2}$$

under steady state conditions. Accordingly, Q = 0 and ΔT can be determined from Equation 4.1.1:

$$V_S = V_{SP} - V_{SJ} = \frac{S^2TI}{\mathrm{K}} - \frac{SI^2R}{2\mathrm{K}}. \tag{4.1.3}$$

Thus, ZT is calculated as:

$$ZT = \frac{V_{SP}}{V_R} = \frac{S^2T}{\kappa\rho}. \tag{4.1.4}$$

With an additional measurement of the temperature gradient generated by Peltier heating or cooling (ΔT_{SP}) at the thermoelectric film/contact interface, the cross-plane S and κ are obtained. σ is calculated simply from the measured resistive voltage provided that the geometry of the sample is known and can be considered one-dimensional.

$$S = \frac{V_{SP}}{\Delta T_{SP}};\ \kappa = \frac{STI}{\Delta T_{SP}}\frac{d}{A};\quad \sigma = \frac{1}{R}\frac{d}{A}; \tag{4.1.5}$$

These conductivity equations assume 1D current flow through a cross-sectional area A for a distance d.

The cross-plane ZT determined in this manner is only accurate if the heat flux across the device is identical to the electrical current profile; specifically, all spurious electrically and thermally generated voltages are eliminated. To accomplish this, the following experimental conditions must hold:

- Adiabatic heat transfer within the thermoelectric device
- Electrical measurements are made in the quasi-static thermal regime
- The average temperature of the device must not change significantly; the assumed Seebeck coefficient is constant during heating and cooling phases.
- Current must be applied uniformly across the device contacts to avoid a 'distributed' Seebeck voltage effect.
- Spurious electrical resistances are eliminated through a four-wire measurement.

As mentioned previously, these last two requirements are especially difficult to achieve in thin film devices.

4.2 Optimization of device design

Specialized processing and device lead geometries can diminish the impact of electrical and thermal parasitic effects and improve the accuracy of the transient Harman measurement enabling the extraction of the cross-plane ZT of thin film thermoelectric materials.[76] To accomplish this, we have employed the finite element method (FEM) and analytical modeling together with thermoreflectance imaging to visualize thermal and electrical paths in thin film samples over multiple generations of metallization geometries and packaging configurations (see Figures 3.3 and 3.4 for older generation geometries).[72,733] Realistically,

both electrical and thermal spreading will occur in the different device layers and must be accounted for. Accordingly, the assumed material conductivities given in equation 4.1.5 are over-simplified; both electrical and thermal conductivity would not only present with a 1/A dependency, but would include an additional $1/\sqrt{A}$ term accounting for spreading resistance in the device.[77]

Finite element simulations considered the three-dimensional heat and electrical current flow throughout the device and included additional parasitic sources: heat generation and conduction in the metal leads, as well as problematic electrical and thermal series resistances. A schematic of the most recent device design is given in Figure 4.1a, and is described in detail in this chapter.

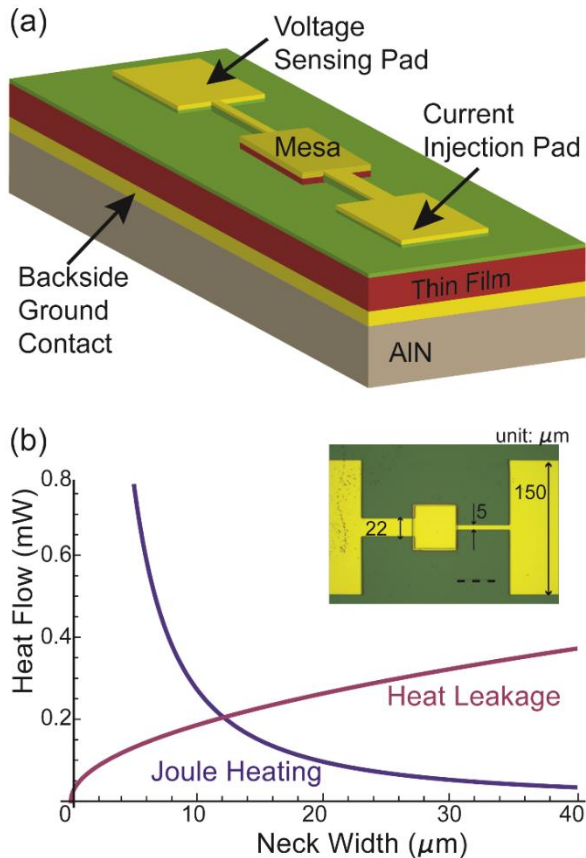

Figure 4.1: (a) Schematic of improved device design for thin-film transient Harman measurement. (b) Trade-off between heat leakage through the current injection lead and heat flow into the device due to Joule heating dissipated in the injection neck of a 25 µm thick 0.2 % ErAs: InGaAs film, plotted as a function of current injection neck width. The inset shows a magnified optical image of the 50x50 μm^2 device examined; the neck width is 22 µm and the thickness of the metal lead is 0.5 µm.

In this design, electric current is delivered to the sample mesa through a long metal lead (gold), which is electrically isolated from the thermoelectric film by a thin layer of SiO_2 (green). Electrical and thermal transport occurs in the cross-plane direction through the thermoelectric material (red) to a backside electrical ground contact and thermal heat sink (gold and brown). Separate electrodes are utilized for applied current and voltage sensing in

order to reduce probe coupling and remove contributions from lead resistances in the voltage measurement. The voltage sensing electrode can then be connected to the device mesa with a much thinner lead, which practically eliminates heat and electrical current flow to the contact. Thus, an open-circuit voltage measurement is ensured. Contact resistance, however, is still present in this design. Ideally, the film thickness is maximized such that the voltage drop across the film is a relatively large fraction of the total measured voltage.

The use of metal leads to deliver electrical current serves to maintain thermal isolation of the device, but can exacerbate injection non-uniformity in the mesa. The magnitude of this effect is governed by the metallization thickness and the lead geometry and its corresponding electrical/thermal properties. A very thin lead width would minimize heat leakage via conduction into the mesa (due to Joule heating from probes and leads) and away from the top contact (i.e. loss of Peltier cooling). However, Joule heating generated in the lead itself is substantially greater for a thin neck design and will have greater impact on heating non-uniformity. Thus, the optimized lead geometry is a trade-off between heat leakage and the influence of Joule heating generation. Figure 4.1b plots the two effects versus current injection lead (neck) width, determined by analytical modeling as described in Wang *et al*.[78] for 25 µm 0.2%ErAs:InGaAs. Thermal leakage from the current injection neck into the mesa is given by:

$$Q_{neck,mesa} = I^2 \rho_{neck} \sqrt{\frac{\kappa_{neck}}{w_{neck}^2 d_{neck} h_{eff}}} - \Delta T_{SP} \sqrt{w_{neck}^2 d_{neck} h_{eff}}. \qquad (4.2.1)$$

In this form, the first term on the right hand side of the equation accounts for Joule heating generated in the neck, while the second term represents Peltier heat conduction away from

the mesa due to the temperature differential. All subscripts labeled 'neck' refer to material parameters and geometries of the current injection lead. h_{eff} is the effective heat transfer coefficient of the material system; this term incorporates heating generated in the neck which flows through an electrically insulating layer into the film (designated by the subscripts SiO_2 and *film*, respectively).

$$h_{eff} = \left\{ \frac{w_{neck}}{2\kappa_{film}} \left[\frac{2d_{film}}{w_{film}} + \frac{2}{\pi^3 \left(\frac{w_{neck}}{w_{film}}\right)^2} \sum_{n=1}^{\infty} \frac{\sin^2\left(n\pi \frac{w_{neck}}{w_{film}}\right)}{n^3} \tanh\left(n\pi \frac{2d_{film}}{w_{film}}\right) \right] + \frac{d_{SiO2}}{\kappa_{SiO2}} \right\}^{-1} \quad (4.2.2)$$

The optimal neck width is calculated by minimizing the sum of these two parasitic effects; for this device it is 21.5 µm. The inset of Figure 4.1b shows a magnified optical image of the processed thin film with the mask dimensions. The above analysis shows that these deleterious effects can be minimized, though not fully eliminated. To avoid further influence on the voltage measurement, the voltage sensing area is located on the opposite side of the sample mesa, as in the figure.

This device design was realized on the 25 µm thick nanostructured InGaAs film, grown via molecular beam epitaxy by collaborators at UC Santa Barbara. Erbium was co-deposited during the growth of the semiconductor matrix, forming semi-metallic nanoinclusions with an atomic percentage of 0.2 %. 250 nm thick highly-doped InGaAs buffer and cap layers were additionally grown on either side of the film to improve the ohmic contact between the film and the metallization layers. To eliminate the effect of the growth substrate, the sample was flip-chip bonded to a Au-coated AlN plate and the growth substrate was subsequently etched away. The 5 µm thick Au layer is used as the backside electrical ground contact. The collaborators used standard photolithographic techniques to deposit and

pattern the mesa contacts with 0.5 μm thickness. Subsequently, a 300 nm SiO_2 insulation layer was deposited with mesa areas exposed to enable fabrication of the side electrodes.

Thermal images were used to assess electro-thermal simulation results and confirm the necessary metallization thicknesses with mesa/contact areas ranging from 50 μm × 50 μm to 150 μm × 150 μm, while also determining the quality of the device processing. Section 3.2 describes some of these analyses, and Figure 3.5 exhibits thermal images of a 100 μm × 100 μm sample. Unfortunately, these devices displayed significant flaking and current crowding within the contact pad, indicative of poor device adhesion/bonding.

4.3 Measurement Details and Results

Measurements of fast thermoelectric transients and thermoreflectance imaging are performed in the optical thermostat under high vacuum (~10^{-6} mbar). The sample is mounted with good thermal contact to the high-speed measurement stage, which thermally sinks the sample and also acts as ambient heater. Heat sinking is important to maintain small ΔTs so there is no appreciable change in thermoelectric properties between heating and cooling cycles. The entire apparatus is capable of 100 ns temporal resolution, necessary for transient detection of thin or thermally diffusive samples. More information about the chamber specifics and the high-speed circuitry is presented in Chapter 6.

Application of the transient Harman technique

We obtained the total voltage responses of the 0.2 % ErAs: InGaAs devices to a bipolar square current pulsed at 500 Hz with a 50 % duty cycle.[76] This ensured that the maximum temperature difference was achieved across the device for a given applied current, thus the generated Seebeck voltage was saturated. The current amplitudes varied from 60 mA to 300

mA, depending on device size. The total magnitude of the measured pulse was recorded to determine V_R, in addition to a highly resolved 'zoom-in' on the thermal decay for each polarity (Figure 4.2). The smallest mesa area, 50 µm × 50 µm, displayed the most uniform current/temperature distribution among the device mesa sizes examined in this experiment; the devices with larger mesa sizes exhibited nonuniformity representative of a large parasitic series resistance. Furthermore, the 50 µm × 50 µm had the highest current density, and consequently, the best signal to noise ratio. Therefore, the results for the 50 µm × 50 µm sized devices are presented and analyzed in this chapter.

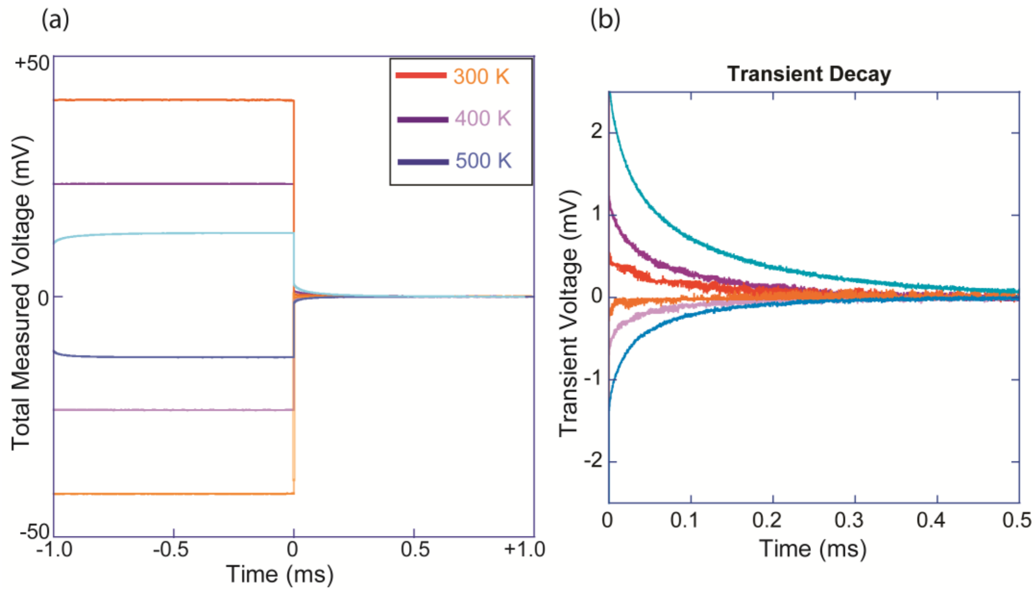

Figure 4.2: The measured voltage response of the thermoelectric energy conversion device to 100 mA bipolar excitation at select ambient temperatures. The positive and negative measured voltages are plotted such that time t =0 is taken as the device turn-off time. The resistive voltage decreases with increasing temperature, while the amplitude of the transient signal is strengthened.

The total voltages for both polarities are presented in Figure 4.2a at select ambient temperatures. The amplitudes of the waveforms are comprised of the resistive, Peltier and Joule voltages, as:

$$V_T(+I) = V_R + V_{SP} + V_{SJ}$$

$$V_T(-I) = -V_R - V_{SP} + V_{SJ} \tag{4.3.1}$$

where *+I* and *–I* represent positive and negative current bias, respectively. Figure 4.2b shows a better view of the voltage transients. The transient signal is expected to match the form of a superposition of exponentials, with each term governed by a thermal time constant associated with the heat capacity of the thermoelectric device. The amplitude of the total Seebeck voltage for each polarity is calculated by fitting the transient signal with a bi-exponential equation of the form:

$$V_S(t) = A + Be^{-t/\tau_1} + Ce^{-t/\tau_2} \tag{4.3.2}$$

where τ_1 is the dominant time constant of 1D heat diffusion from the sample surface to the backside of the film and can be expressed by[79]

$$\tau_1 = \frac{4}{\pi^2}\frac{d^2}{D_{Th}}. \tag{4.3.3}$$

d is the film thickness and the thermal diffusivity D_{Th} relates the thermal conductivity and the volumetric heat capacity C_h of the film, $D_{Th}=\kappa/C_h$. The second significant thermal time constant τ_2 accounts for heat spreading within the film, the AlN layer, and the packaging. The magnitude of the transient signal at device turn-off, time $t=0^+$, is taken as the sum of the coefficients of equation 4.3.2: *A+B+C*.

V_{SP}, V_{SJ}, and thus V_R are extracted using the following equations:

$$V_{SP} = ½[V_S(+I) - V_S(-I)]$$

$$V_{SJ} = ½[V_S(+I) + V_S(-I)] \quad (4.3.4)$$

To reduce measurement error, V_R is calculated as the average value determined from both the positive and negative polarity pulses.

The measured Seebeck voltage transients for various applied currents at room temperature are depicted in Figure 4.3 for one of the 50 µm × 50 µm devices. The insets display the extracted V_{SP} and V_{SJ} amplitudes plotted versus applied current. The Peltier component of the transient voltage exhibits a linear increase with current (Figure 4.3a), while the Joule component shows quadratic dependence on current (Figure 4.3b), as expected. The proper dependencies with applied bias demonstrate the accurate transient resolution of the measurement for the specific current range and temperature.

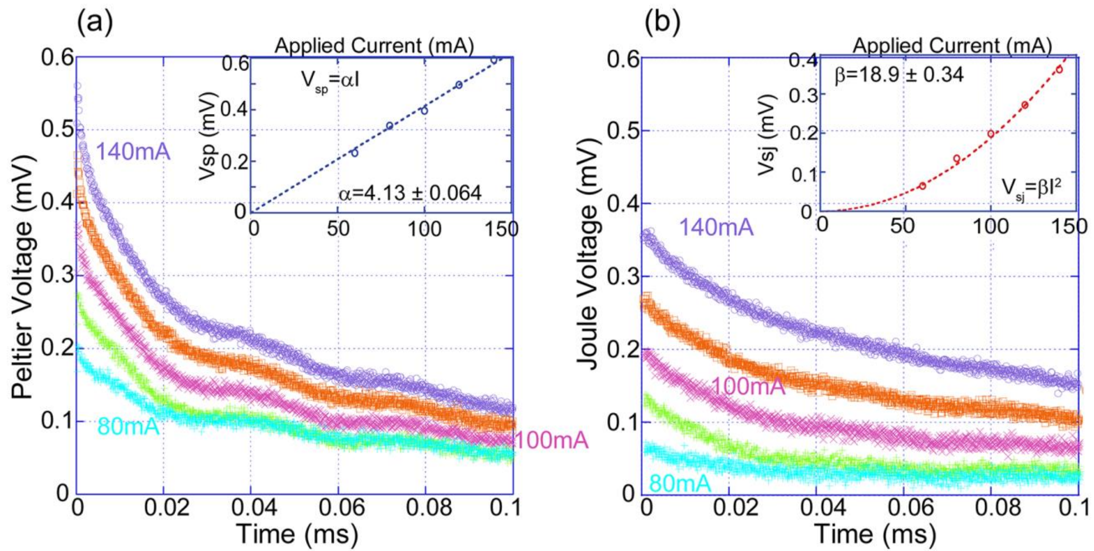

Figure 4.3: The Peltier (a) and Joule (b) transient Seebeck voltages taken at various applied biases at room temperature for a 50 µm × 50 µm device. The insets display the total amplitude of the transient voltage signal plotted against input current. α, β are fitting parameters.

Thermoreflectance imaging

In order to determine the cross-plane Seebeck coefficient and κ from the transient data, the temperature change due to the Peltier effect, $\Delta T_{SP,}$ at the device/contact interface must be known. We employed thermoreflectance imaging of the active device to achieve this end. A narrowband green LED (λ ≈ 530nm) was used for sample illumination through a microscope objective with 10x or 20x magnification and the reflectivity was monitored with the thermal imaging set up described in Chapter 3. Green illumination was selected due to the relatively strong C_{TR} for Au at this wavelength. We calibrated C_{TR} in the measurement apparatus at room temperature, and determined C_{TR}= (2.26 ± 0.05) × 10^{-4} /K for these devices.

To obtain thermal images, we utilized both the 4-bucket and the differencing method (square-pulse 4-bucket) with the thermoelectric device pulsed at the same current amplitudes as in the transient Harman measurement. An analogous procedure was used to distinguish between the Peltier (ΔT_{SP}) and Joule (ΔT_{SJ}) components of the thermal signals from the total measured temperature across the mesa (ΔT_T), as discussed in the previous chapter:

$$\Delta T_{SP} = \tfrac{1}{2}[\Delta T_T(+I) - \Delta T_T(-I)]$$

$$\Delta T_{SJ} = \tfrac{1}{2}[\Delta T_T(+I) + \Delta T_T(-I)]. \qquad (4.3.5)$$

Figure 4.4 shows the optical and thermal images of the same 50 µm × 50 µm active device biased with 100 mA at 300 K, separated into Peltier and Joule components, as before. The relative phases of these surface temperature fields depict the Peltier signal as 180° out of phase with the Joule signal, indicating that the sample was cooling at this reference polarity, while Joule was always heating. The Peltier temperature distribution across the sample is fairly uniform, varying by ~9 % across 50 µm; this is a consequence of the improved device design and the resultant current injection uniformity. The Peltier image also exhibits minimal thermal leakage into the current electrode, though some activity is still apparent in the phase image. Phase information in general is quite sensitive to small variations in the thermal distribution across the sample and thus reveals slight reflectivity changes. Joule activity for the most part is dominant in the current injection neck region, with some leakage visible into the mesa region. The uniform phase over the sample indicates the presence of Joule heating in areas where current is flowing, as expected. The magnitudes of the Peltier and Joule temperature signals are plotted versus applied bias at room temperature in Figure 4.4. Again, they exhibit the respective linear and quadratic dependencies.

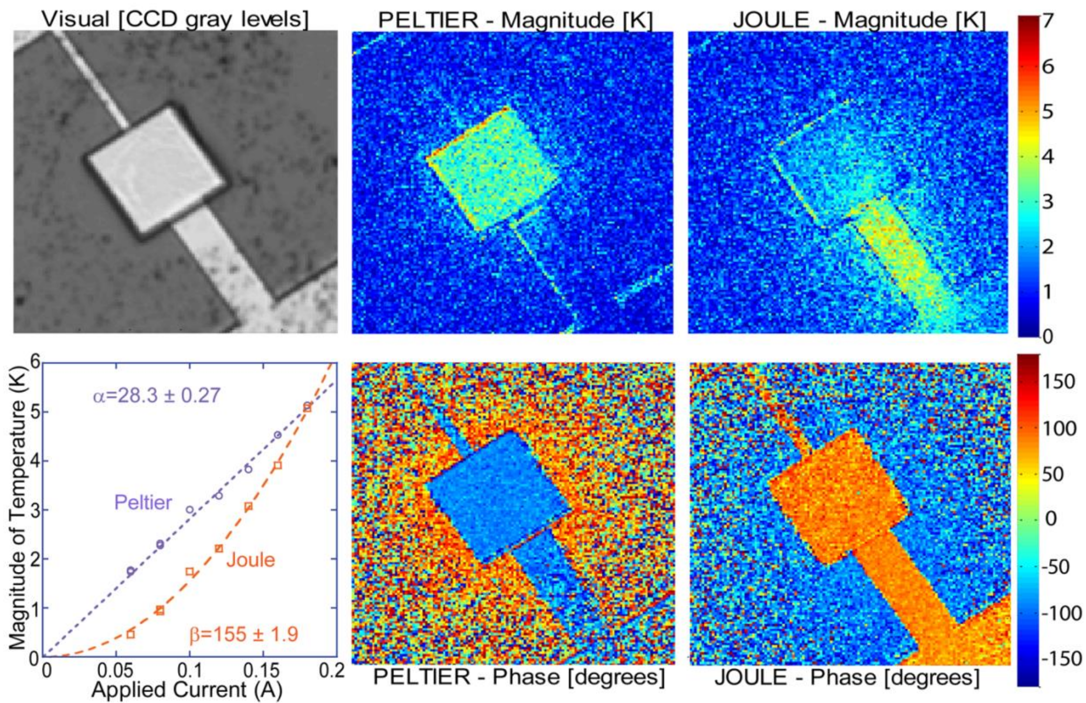

Figure 4.4: Thermoreflectance imaging of the 50 µm × 50 µm device at room temperature taken at 100 mA bias, separated into Peltier and Joule components. Color bars show the absolute temperature/phase difference from ambient. α, β are fitting parameters for the Peltier and Joule temperature amplitudes (respectively) with current.

High temperature experimental results and cross-plane Seebeck

Transient voltage and temperature measurements of the energy conversion devices fabricated with 0.2 % ErAs:InGaAs thin films were performed at discrete temperature steps of 50 K from room temperature up to 550 K. According to the analysis of the previous chapter, the thermoreflectance coefficient of gold is only expected to vary by 10 - 15 % over this temperature range. However, sample degradation occurred at 500 K invalidating the calibration results at this temperature range.

The Peltier and Joule transient voltages (Figure 4.5) and thermal images (Figure 4.6) are presented at various ambient temperatures under a constant applied bias of 100 mA. The insets of Figure 4.5 show the respective Seebeck voltage signal amplitudes as a function of temperature; V_{SP} increased more rapidly than V_{SJ} with increasing temperature as anticipated by the additional temperature dependence in the V_{SP} term shown in equation 4.1.3. A similar trend was evident when comparing ΔT_{SP} with ΔT_{SJ} over the measurement temperature range, as shown in Figure 4.6b. Thus, the potential for higher energy conversion efficiency increases with temperature for this device. For brevity, Peltier and Joule thermoreflectance images at select ambient temperatures are displayed in Figure 4.6, together with the average ΔT_{SP} and ΔT_{SJ} plotted versus ambient temperature. Both the Peltier and Joule signals became more substantial at elevated temperatures, resulting in increased thermal leakage through the current electrode neck. Joule heating in this region also intensified due to increasing Au resistivity with temperature. Both effects worsened temperature non-uniformity in the device, which is especially apparent at ambient temperatures around 500 K and above. Moreover, the sample surface itself had an altered visual appearance at these temperatures. The assumed C_{TR} in the thermal images (-2.11×10^{-4} / K) at 500 K does not account for sample roughening and darkening, clearly visible in Figure 4.7. At these temperatures, it seems that the Au in the contact mesa unexpectedly began to diffuse into the film and slightly darkened the mesa surface, thus changing the thermoreflectance coefficient and yielding the large error bars shown in figure 4.6. This is probably due to a poor diffusion barrier between the metal and semiconductor film.

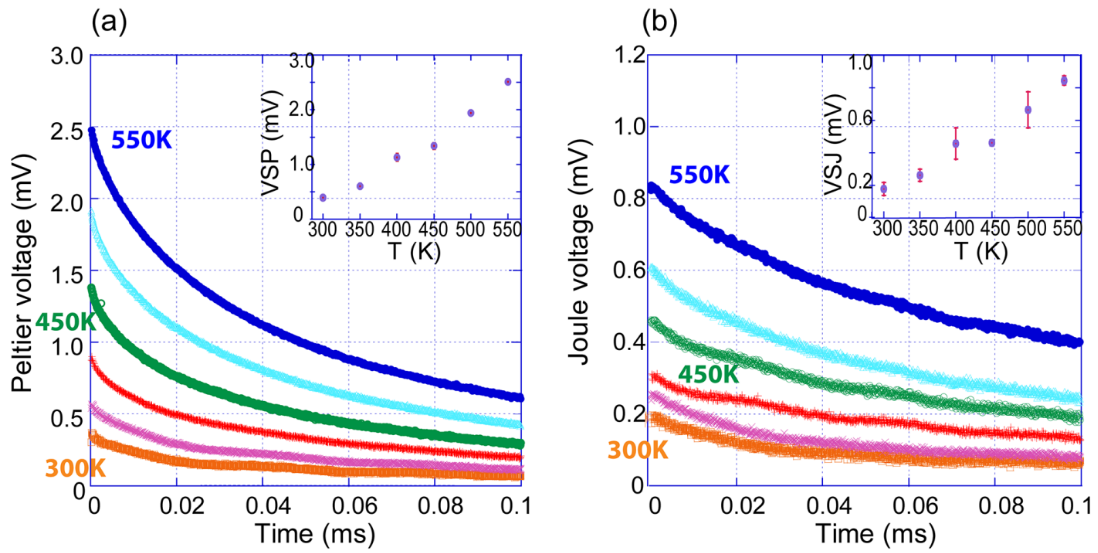

Figure 4.5: Transient Seebeck voltages under ~100 mA excitation at different ambient temperatures, from room temperature to 550 K with 50 K temperature steps. (a) Peltier component of the Seebeck voltage. (b) Joule component of the Seebeck voltage. The insets show the amplitudes of the respective voltage transients plotted versus ambient temperature.

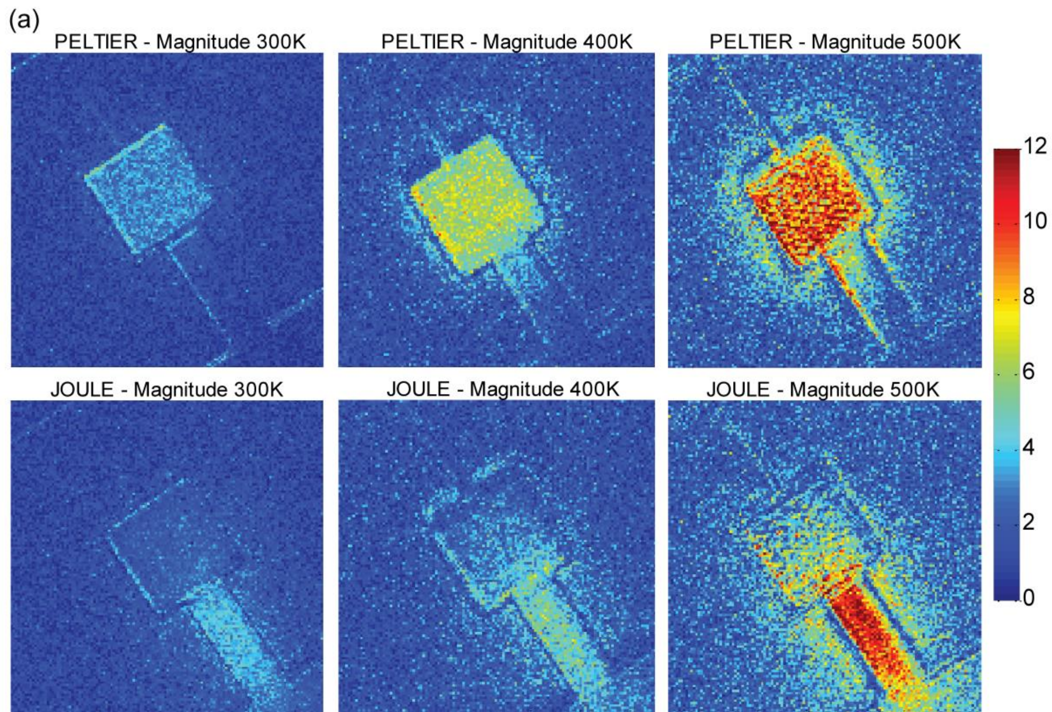

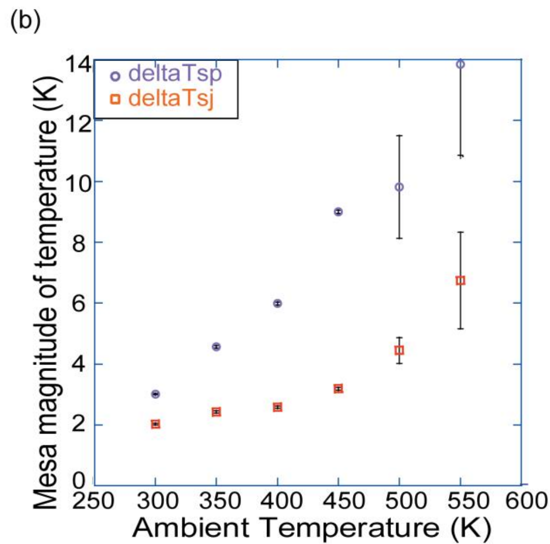

Figure 4.6: (a) Peltier and Joule thermoreflectance images of the device at varying ambient temperatures: 300 K, 400 K, and 500 K. Color bar represents absolute temperature difference from ambient. (b) Peltier and Joule temperature signals plotted versus ambient temperature; these values are averaged over the mesa. The large error bars at ≥ 500 K are due to sample surface degradation affecting the assumed thermoreflectance coefficient of the device at the higher temperature.

The cross-plane Seebeck coefficient of the thermoelectric device can be calculated by dividing the two values depicted in Figures 4.5 and 4.6 at each measurement temperature, which matches very well with independent in-plane measurements. The experimental cross-plane Seebeck coefficient is plotted in Figure 4.8 alongside in-plane results for a 2 µm thick 0.2 % ErAs:InGaAs thin film measured using a temperature differential technique at UC Santa Barbara. The total error in the measurement was calculated by accounting for the dominant error sources: error in fitting the amplitude of the transient voltage, standard deviation of the average temperature distribution across the sample as depicted in the thermal images, as well as error in the assumed value of the coefficient of thermoreflectance. Additional smaller sources of error were considered, including applied voltage fluctuations and variations in temperature readings. The large error bars at 500 K and 550 K come from the change in the appearance of the sample surface and its impact on the assumed value of C_{TR}.

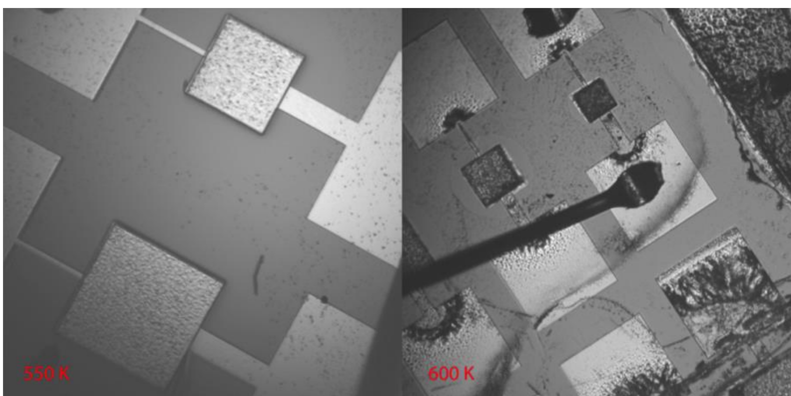

Figure 4.7: Optical images of the device depicting surface degradation effects after experiencing 550K and 600 K ambient temperature.

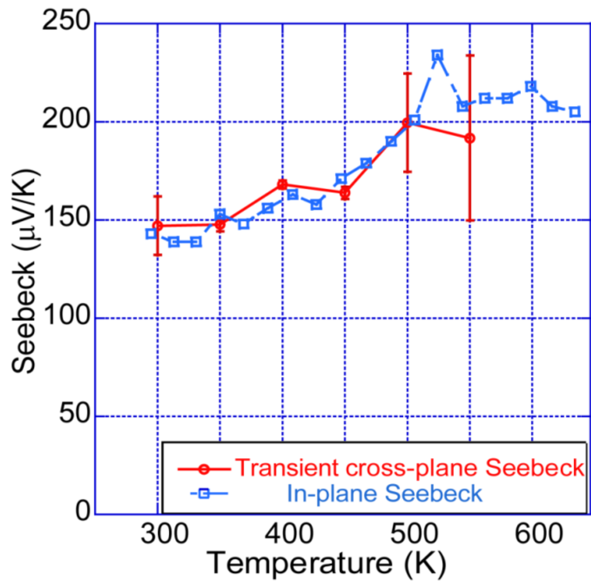

Figure 4.8: Comparison of the measured Seebeck coefficient calculated in the cross-plane direction using the transient Harman technique in conjunction with thermoreflectance imaging on a 25 µm thick 0.2 % ErAs:InGaAs film (red, closed circles) to that of a 2 µm thin-film measured in the in-plane direction (blue, open squares).

4.4 Finite Element Modelling

For these particular devices, the directly measured ZT was unexpectedly low in comparison to the ZT of 2 µm thick 0.2 % ErAs:InGaAs thin film acquired from three separate in-plane (and cross-plane 3ω) measurements. Since the values of the Seebeck voltages were reasonable, the main discrepancy is in the measured resistive voltages of the device, which were 5 to 10 times higher than anticipated and varied with the location of ground on the device. Furthermore, we observed an abnormally high degree of non-uniformity in the thermoreflectance images of the larger mesa areas (Figure 3.5). These images display

current crowding along the contact pad edges, corresponding to a high electrical resistance 'seen' from the perspective of the electrical current in the contact pad, in agreement with the resistive voltage measurement.

My collaborator, Amirkoushyar Ziabari used the 3D finite element modeling software, ANSYS, to study the electrical and thermal paths in order to explain this aberrant behavior. The simulation utilizes the coupled heat and electric field equations in a thermoelectric material:[80]

$$q = ST \cdot J - \kappa \cdot \nabla T$$

$$J = \sigma \cdot (\mathrm{F} - S \cdot \nabla T) \tag{4.4.1}$$

where q is the heat flux inside the medium, J is the electric current density through the device, and T is the absolute temperature. These equations couple the two equations governing the rate of heat flow and electric current continuity in the material, given as:

$$C_h \frac{\partial T}{\partial t} + \nabla \cdot q = p_{Source}$$

$$\nabla \cdot \left(J + \frac{\partial \varepsilon \mathrm{F}}{\partial t} \right) = 0. \tag{4.4.2}$$

ε is the permittivity of a thermoelectric material and F is the electric field. The volumetric power density, p_{Source} , is comprised of a term representing the generated Joule heating, J^2/σ, and a second term characterizing the rate of heating/cooling from the Seebeck effect, per unit volume: $J \cdot (S \nabla T)$. The substitution of the thermoelectric field equations into the

second set gives a coupled system of equations that is solved iteratively until convergence of the voltage and temperature distributions at steady state is achieved.

From the simulation results, we found that the 5 µm gold backside ground layer should only contribute a small factor, on the order of a mΩ, to the total resistive voltage measurement. This would certainly not be apparent when moving the location of the ground probe. The only scenario that reproduced the measured high resistive voltages and thermal profiles was in which the backside ground contact was removed from the analysis; that is, the current flows in the in-plane direction through the semiconductor film to a top-side grounding probe rather than the backside ground contact. This result suggests a significant interfacial contact resistance between the film and the backside ground pad likely caused by issues during processing of the devices. Both electrical resistance measurements as well as thermal images on devices of various mesa sizes are consistent with the assumption that current flows in the thermoelectric film only. The intended current path through the device is illustrated in Figure 4.9a, alongside the actual path taken by the current (Figure 4.9b) resulting in high electrical resistance.

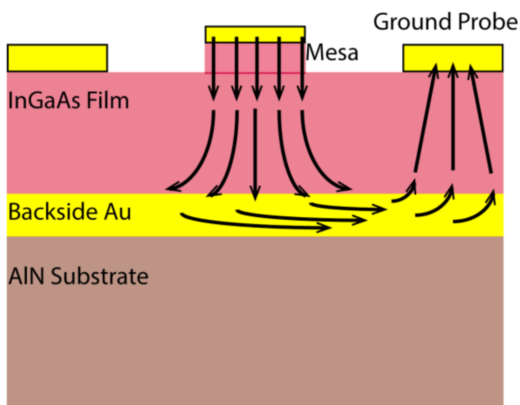

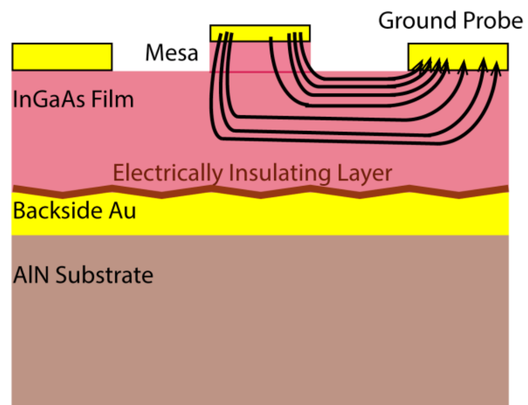

Figure 4.9 (a) Schematic depicting the correct current path, and the actual current path in the device (b) as determined by FEM analysis.

With the new understanding of the electrical and thermal paths through the device, the accurate material properties of the device at room temperature can be extracted. First, we ran the ANSYS simulation iteratively for different electrical conductivity values using the measured Seebeck as input, and adjusted the thermal conductivity of the film to achieve the best fit of the Peltier signal with the experimental results. The difference between the simulated Joule heating and the measured Joule data was used to extract the specific contact resistivity of the contact pad on the mesa, yielding the actual electrical resistivity of the nanostructured semiconductor material: which are 2.0×10^{-6} Ω-cm^2 and 11.5×10^{-4} Ω-cm, respectively. The (topside) electrical ground pad is sufficiently large such that its contact resistance can be neglected. These values were consistent for the different mesa areas measured. The simulated and measured thermoreflectance images in forward bias are presented side by side for a 50 µm × 50 µm device in Figure 4.10. In order to determine the high temperature thermal conductivity, we kept both the electrical conductivity and electrical contact resistivity constant throughout the temperature range. This is a reasonable assumption as the electrical conductivity of the film is expected to vary by ~ 3 % over the temperature range, based on in-plane van der Pauw measurements of the 2 µm film. Then, the measured Seebeck values at elevated temperature were input into ANSYS and the thermal conductivity was iteratively varied to achieve the best fit for both the Peltier and Joule (forward and reverse) profiles simultaneously. The simulated thermal profiles are plotted with the experimental data up to 450 K in Figure 4.11. The values

obtained for material parameters of 0.2 % ErAs:InGaAs film at 300 K and 450 K are summarized in Table 4.1. The simulation results for different device sizes are in good agreement.

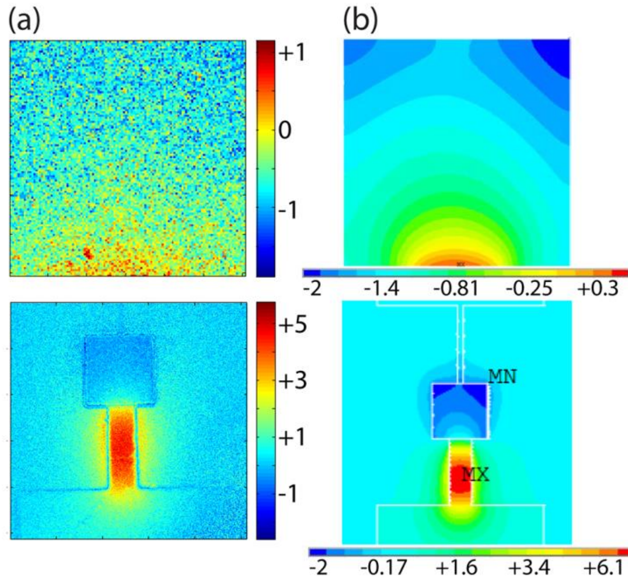

Figure 4.10: Direct comparison of the measured thermoreflectance images (a) and the finite element modeling results (b) for a 50 µm × 50 µm device under 90 mA bias in cooling mode. The top figures display a zoomed-in view of the mesa only, while the bottom set shows the device with leads. Color bars represent change in temperature (K) relative to ambient.

Using the material parameters which reflect the actual current path in the devices, the room temperature ZT is calculated as 0.114 and is 0.345 at 450 K, which are respectively 14 % and about 9 % lower than that determined by three separate measurements of the individual properties on 2 µm 0.2 % ErAs:InGaAs thin film. This is primarily due to the larger thermal conductivity determined in this work for these devices than that measured using the 3ω technique on the 2 µm film. This discrepancy may a result of variations in sample growth conditions during the long-time growth of the 25 µm film (2 µm per hour). In addition, a 25

μm film may very well have different material properties than that of a 2 μm film due to the possible additional contribution of long mean-free-path phonons.

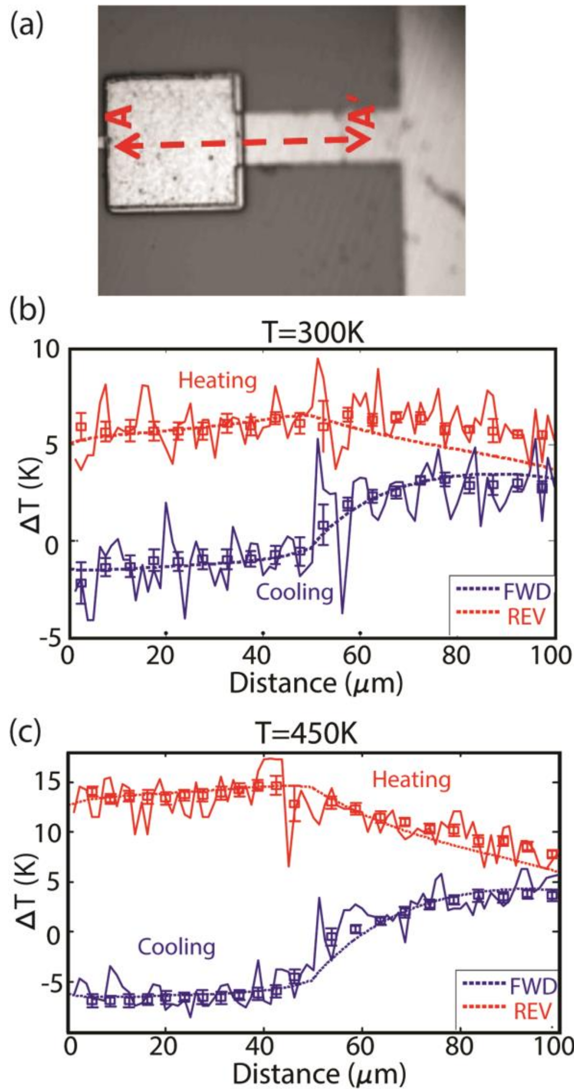

Figure 4.11: Comparison of the thermal profiles between simulation (dashed lines) and thermoreflectance experiment (open squares) in forward and reverse bias (cooling and heating modes). (a) Optical image of the 50 μm × 50 μm experimental device modeled by ANSYS 3D finite element simulation. Thermal profiles and simulation results at room temperature (b) and 450 K (c). The thermal profiles displayed are the measured ΔT averaged over a box that sweeps the cross-section from A (0 μm) to A' (100 μm) (squares with error bars). Solid lines are the raw data over the 100 μm cross-section.

Table 4.1. Summary of the 25 µm 0.2 % ErAs:InGaAs material parameters in the cross-plane direction determined by either direct measurement or through FEM simulation compared alongside the reported in-plane and 3ω values of a 2 µm thin-film of the same composition.

Data Source	Seebeck Coefficient (µV/K)		Electrical Conductivity $(\Omega\text{-cm})^{-1}$		Thermal Conductivity (W/m-K)[b]		ZT	
	300 K	450 K	300 K	450 K	300 K	450 K	300 K	450 K
Independent measurement data [a]	-143	-171	872	842	4.0	2.9	0.13	0.38
Transient ZT/FEM extraction [c]	-148	-168	870	870	5.0	3.2	0.11	0.35

[a] data taken on 2 µm 0.2 % ErAs:InGaAs thin film
[b] data from cross-plane thermal conductivity measurements on 2 µm sample using 3ω technique
[c] Seebeck data directly from transient ZT cross-plane measurements

Chapter 5 High magnification imaging of vanadium dioxide nanobeams

The spatial resolution of thermoreflectance microscopy is governed by the optics used to detect the reflected signal; however, it is fundamentally constrained by the diffraction limit to around 200 nm with visible light. We apply the technique at the edge of this limit to capture thermal images of the M-I heterostructures in single-crystalline VO_2 nanobeams (NBs). Thus far, electrical measurements of the thermoelectric properties of VO_2 NBs have been conducted over the length of the device,[81,82] determining effective material properties with indirect information about the domain interface. With thermal imaging, we directly observe highly localized Peltier cooling/heating and Joule heating at the M-I boundary, which acts as a thermal point source. In addition, an observed change in polarity of thermoreflectance coefficient can differentiate between the two available insulating phases. These experiments provide insight into the native M-I heterostructures of VO_2 NBs and elucidate the underlying impact of stress.

5.1 VO_2 material background information

VO_2 is an extensively studied correlated material; it undergoes a highly stable high-temperature metal to low-temperature insulator transition (MIT) at $T_{MIT\text{-}Bulk}$ ~ 340 K.[83] The electronic phase transition is accompanied by a structural transition in which a metallic rutile phase (M_R) converts to a semiconducting monoclinic phase (I_M),[84] resulting in ~ 1 % expansion of the lattice along the tetragonal *c*-axis (C_R).[85,86] The metallic and insulating phases of VO_2 can be readily distinguished visually; they exhibit quite different reflective

intensities and coloring . See Figure 5.1a. However, multiple monoclinic lattice structures (I_{M1}, I_{M2}) are available for the insulating phase, which are almost optically identical and have very similar free energies,[87] adding to the complexity of the material system. The more resistive I_{M2} phase has a lattice constant ~ 0.6 % longer[85] along C_R than I_{M1} and can act as an intermediate state between I_{M1} and M_R. It is generally associated with higher tensile strains.[88,89,90,91,92] Raman spectrographic analysis can be used to determine the state of the physical domains, as shown in Figure 5.1b.[92,93,94] Though it is generally believed that the MIT is induced by the symmetric splitting of the t_{2g} band comprised of 3d vanadium states[95] (Figure 5.1c), the physical nature of the M-I wall is still poorly understood despite its promising electrical and thermal applications.

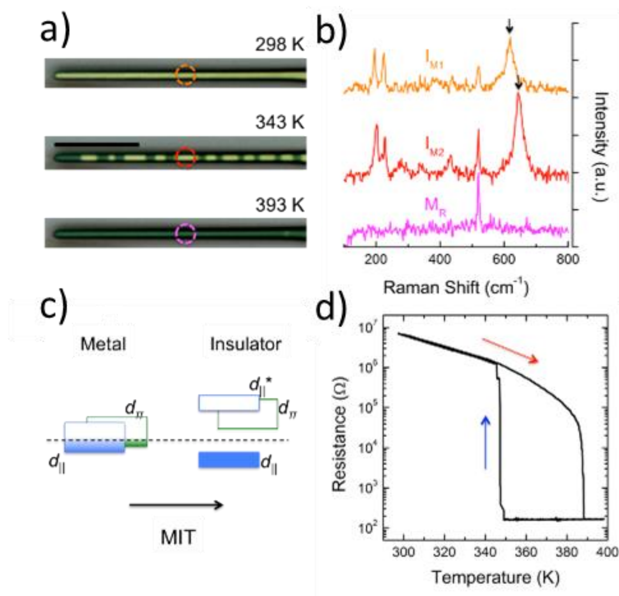

Figure 5.1: Metal-insulator heterostructures along an individual VO_2 nanobeam. a) Optical images of a typical VO_2 NB upon heating from room temperature (I_{M1}) through coexisting domains (M_R and I_{M2}) to a fully metal M_R state. Scale bar represents 10 µm. b) The physical domains are identified by Raman spectroscopy. c) Band diagram for M and I_M phases. d) Heating and cooling electrical resistance as a function of temperature for NB_{type1}.

One-dimensionally aligned metal-insulator (M-I) domain configurations, as displayed in the figure, can be attained either by substrate-induced uniaxial strain[96,97,98] or transitional metal doping in a single-crystalline VO_2 nanobeam (NB).[99] In the former case, M_R domains appear gradually upon heating, shifting T_{MIT} in a manner dependent upon the nature of external stress. Tensile strain along C_R would drive the material system toward the I_M phase, increasing the temperature where the insulating domains subsist. Likewise, compressive strain would drive the NBs toward a metallic state, which decreases the temperature where metallic domains are formed. Given a strong adhesive interaction with the substrate, I_{M2} phase (with longer lattice constant along C_R) becomes thermodynamically stable and the alternating M-I heterostructures are spontaneously organized (Figure 5.1a). This substrate-mediated MIT leads to a gradual decrease in electrical resistance until VO_2 NB becomes fully metallic around ~ 390 K (Figure 5.1d).

5.2 Measurement Specifics

We investigate the electro-thermal activities at M-I walls by utilizing 8-bucket thermoreflectance to create thermal maps of VO_2 NBs grown on SiO_2/Si substrates in the M-I coexisting regime.[100] These VO_2 NBs are naturally bonded to the substrate and experience uniaxial tensile strain along C_R (oriented as the NB long axis) as a result of high temperature growth and thermal expansion mismatch between the NB and the substrate upon cooling.

The NB substrate was mounted with a thin layer of thermal paste onto a Peltier heater for ambient temperature control. A narrowband green LED (λ ~ 530 nm) was used to illuminate the VO_2 NBs through a microscope objective with 250x magnification. We selected green illumination since the C_{TR} for the contact material (Au) is well known at this wavelength. The thermal images produced during this experiment assume a uniform C_{TR} of -2×10^{-4} K^{-1}.

We utilized the 8-bucket approach due to the inherent difficulty in stabilizing and lack of repeatability of the domain wall configurations; these measurements are susceptible to variation inflicted by tiny fluctuations of the experimental conditions in the M-I coexisting state. Bias current amplitudes were limited to ~15 μA such that the NB domains would not be displaced by electro-thermal effects[101] during measurement averaging, the excitation period of which is approximately 5 orders of magnitude longer than the typical thermal response times for devices this size. We employed the minimum possible current bias that induced a measureable signal while remaining in the linear regime of the I-V curve for the NB. The optical images were continuously monitored during the measurement to ensure the stable configuration of M-I heterostructures along the NBs. We confirmed that the resultant reflectivity signals represent actual thermal fluctuations and not movement at the domain boundaries by inspection of the phase images. The thermal signals at the interfaces are uniform over a larger width than expected for edge effects from movement not observed optically and exhibit point source-like behavior with continuous activity into the nearby substrate.

5.3 Measurement results: periodic domain organization

Several NB devices were examined in this manner, and it became apparent that each NB could be categorized into one of two observed trends, which depended on the strength of the attachment to the substrate (hence built-in strain): the first type exhibited periodic domain configuration and had a smooth decrease in resistance with temperature, as described in Figure 5.1. The second type of NB displayed few and irregular domain formation, accompanied by a distinct jump in electrical resistance around T_{MIT}. For clarity, representative examples of each category, designated NB_{type1} and $NB_{type2,}$ respectively, are presented for analysis.

We first discuss results for a VO_2 NB (type 1) which exhibited the typical periodic domain configuration; Raman spectra of this device is displayed in Figure 5.1b and established this that device was in the M_R-I_{M2} phase coexisting state. Thermal images of the NB taken at 355 K under an applied 10 μA sinusoidal current are presented in Figure 5.2. These images were averaged for ~ 500 cycles. As discussed, periodic domains are indicative of homogenous substrate adhesion and are clearly observed in the optical image depicted in Figure 5.2a,b (greyscale image); this domain configuration remained stationary for the duration of the thermoreflectance measurement. Figures 5.2c,e display the temperature magnitudes of the Peltier and Joule signals, respectively. Both signals originate in the interface regions between metal and insulator domains which behave as thermal point sources. In these optical experiments, the exact location and width of the signal may not be fully resolvable due to the diffraction limit. We expect to see Peltier heating or cooling at the M-I junction given the presence of an energy barrier.[102,81] On the other hand, Joule heating is also

concentrated at the M-I junction indicative of a significant resistance of the domain wall (R_{DW}) between the metallic and insulating domains. For the specific current amplitude depicted in these figures, Joule heating is stronger than the magnitude of Peltier and is consequently better resolved; the average ratio of the Joule magnitude to that of Peltier (J/P) is ~ 1.75. It is interesting to note that while R_{DW} plays a minor role from an electrical standpoint (relative to the overall NB resistance), it dominates the local thermal behavior of the NB. Thermal imaging reveals that the associated resistance is also comprised in a very small region, leading to power densities at the M-I junction that are much higher than that along the length of the NB. Highly localized Joule heating may also be attributed to the band offset between M and I domains through the possible introduction of an associated depletion region. The formation of a Schottky barrier or another similar energy filter at the junction could explain both thermal signatures; the depletion width is estimated to extend ~ 20 nm into the insulating domain. However, the exact nature of the junction is still unknown.

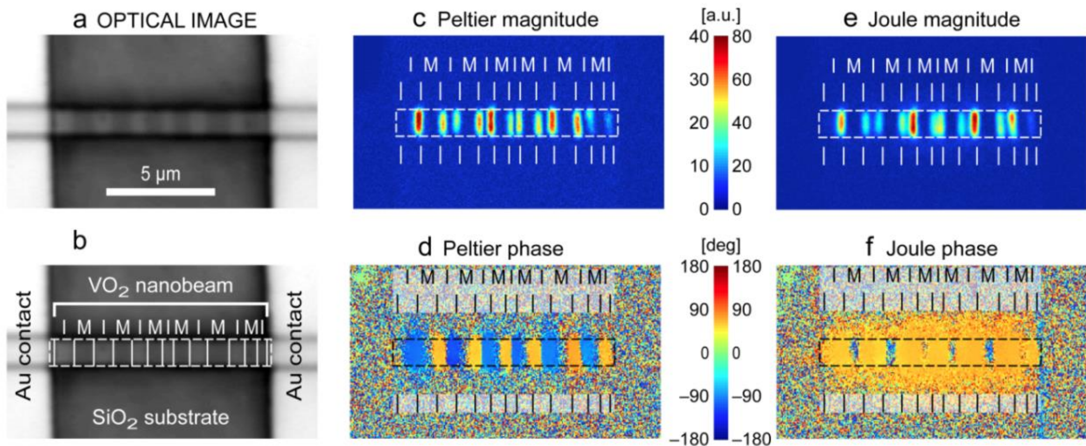

Figure 5.2 Thermoreflectance thermal images of NB_{type1}taken at 355K with 10μA applied current, after 500 cycles averaging. a),b) Optical images of the nanobeam and 'map'

(greyscale). c), d) Peltier temperature magnitude and phase images, respectively. e), f) Joule temperature magnitude and phase images. While both Peltier and Joule signals are localized at the interfaces, phase images show very different dynamics of how alternating Peltier cooling and heating in nearby interfaces exchange energy mainly through the nanobeam. Conversely, there is no cancellation in the Joule activity and Joule heating propagates into the substrate.

The information garnered from the thermal phase signatures can be much more revealing as thermal phase is quite sensitive to small variations in the thermal distribution across the sample. Since the NBs are probed in the quasi-steady state, the thermal phases are uniform. Thus, the deviations in the phase image are due to bipolar behavior (cooling instead of heating) or sign changes in the C_{TR} and expose the underlying physical properties. The Peltier phase image (Figure 5.2d) depicts both heating and cooling localized at the M-I interfaces: when one interface is heating (under forward bias), the neighboring interface is clearly cooling (under reverse bias) denoted by the 180° phase shift. As expected, the Joule signal (Figure 5.2f) does not exhibit this phase shift and is always heating. Cross-sections of the optical response, averaged over the width of the NB, are displayed in Figure 5.3. Asymmetry in the adjacent peaks corresponding to neighboring M-I interfaces may expose a slight asymmetry in signal magnitude between forward and reverse bias, conceivably signifying diode-like behavior.

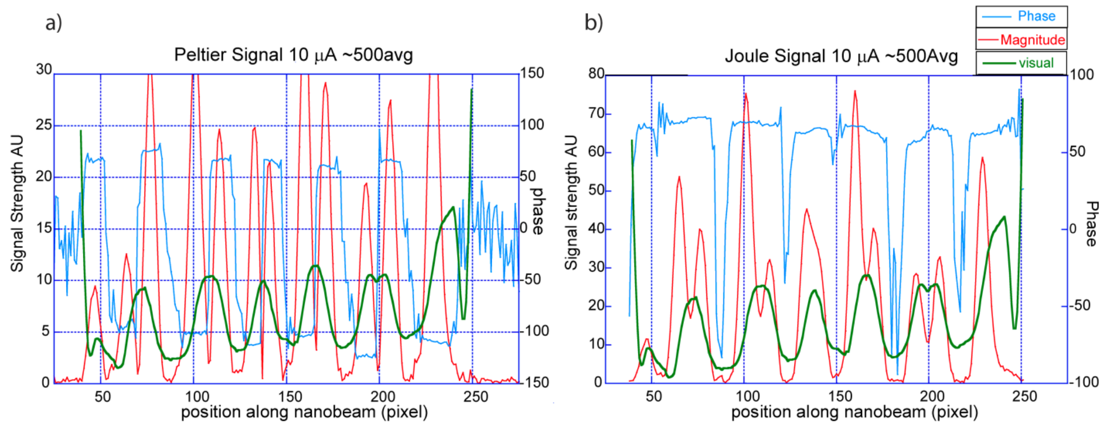

Figure 5.3: The Peltier a) and Joule b) thermal signals plotted with respect to location along NB_{type1}. The magnitude of the temperature response is shown in red and the thermal phase in blue; the visual image (baseline reflectance) is depicted in green. These signals are averaged across the width of the NB.

While the Peltier signal is seemingly concentrated inside the insulating region, we expect the actual thermal activity to present equally in the metal region (neglecting the small effect of a depletion region). We attribute the apparent lack of thermal signal over the metallic state to a small thermoreflectance coefficient, as the images are based on a uniform C_{TR} calibrated for Au only. Phase-shifted Joule activity is evident in the metal regions of the NB and into the substrate due to its stronger signal, but is not visible in the magnitude images. To explain this result, the C_{TR} of the metal phase must be of opposite sign and significantly smaller in magnitude than that of the insulating state. It is evident in Figure 5.2f that the supporting substrate of the sample also functions as a heat sink for Joule heating. The signal spreads outward uniformly from its peak at the domain walls, demonstrating good thermal contact between the NB and the substrate. The lack of Peltier substrate activity is not simply because of its lesser signal magnitude. Heating and cooling signals at nearby domain walls

are mainly coupled through the nanobeam with little leakage into the substrate; this interaction diminishes the overall Peltier magnitude in this device.

5.4 Measurement results: irregular domain configuration

The apparent total strain (and thus domain pattern) differed between samples due to non-uniform substrate adhesion, variations in growth temperature (~50° C,) and stress induced by the end-to-end clamping by the contacts. In this context, NBs with non-periodic M-I domain pattern would display quite different temperature-dependent behavior, as is shown in Figure 5.4 for a sample (NB_{type2}) held at 348 K. Current was applied across the two consecutive segments of the NB depicted in Figure 5.4a,f; referred to from this point on as the right hand side (RHS) segment and the left hand side (LHS) segment. Irregular domain patterns nucleated from the side contacts beginning at 328 K, a much lower ambient temperature relative to NB_{type1} and considering $T_{MIT\text{-}Bulk}$. The domain walls in both segments were initially at a ~50° angle relative to the NB long axis. The configuration and angled walls of the domains in this NB may indicate non-uniform stress distribution along the length and width of the NB,[90,97,98] suggesting weak substrate interaction and/or clamping strain from the Au contacts.

The experimental conditions were similar to those of the previously described NB; the applied current ranged from 5 μA to 10 μA, as this was the minimum necessary to resolve the Peltier signal. After one measurement run at 8 μA bias, the domain configuration on the RHS changed from M-I-M with angled domain walls (Figure5.4a-e) to M-I with a single vertical wall (Figure 5.4f-j), most likely due to excessive Joule heating at the interface. The new domain configuration was stable for all subsequent measurements.

The magnitude of Peltier temperature in the RHS segment was very similar to that of uniformly clamped NB (Figure 5.2c), however, Joule heating was substantially greater: J/P_{RHS} ~ 7 and J/P_{LHS} ~ 5 for the same current bias applied for NB_{type1} (10 μA). Such significant Joule heating, especially apparent on the RHS, could drive the insulating domain to another state (from I_{M1} to I_{M2}). It is also clear in the images that this device does not dissipate Joule heating into the substrate as well as NB_{type1}, suggesting weaker adhesion. This highly localized electro-thermal activity at the junction is responsible for M-I domain wall propagation along the VO_2 NBs at high currents (well above those used during the measurement), as demonstrated in suspended $W_xV_{1-x}O_2$ NBs.[101] The resultant domain oscillation could be controlled and sustained with the addition of a parallel capacitor by repeating the charging and discharging process.

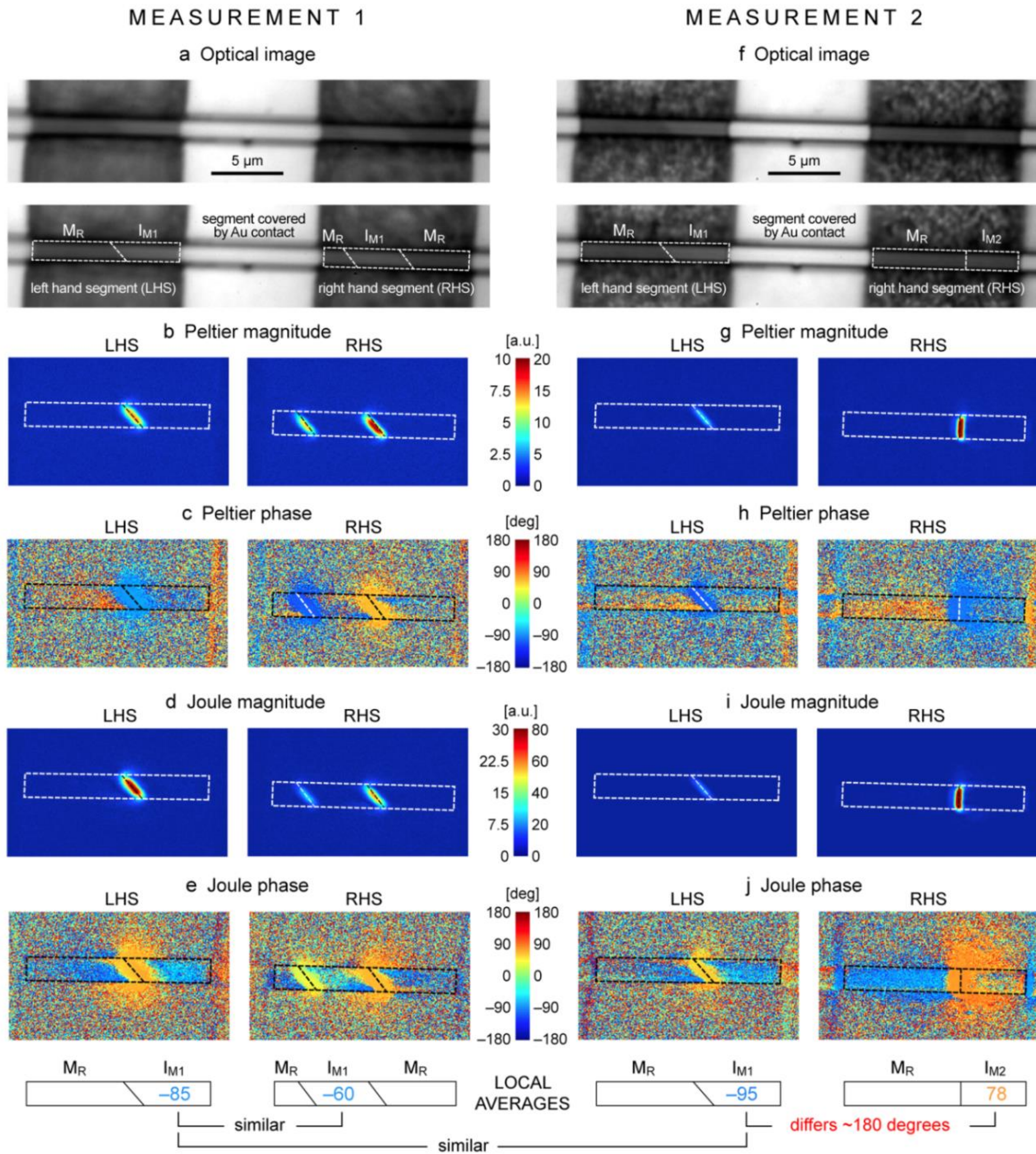

Figure 5.4: Thermal images of non-periodic nanobeam (NB_{type2}) at 348K with 8μA current excitation, averaged for 500 cycles. Two NB segments and the adjoining electrode region are active. a-e) Initial thermoreflectance measurement images of NB_{type2} before the RHS segment changed from M-I-M to M-I domain configuration. f-j) Thermal images for the same current bias taken after the RHS segment stabilized. Both Joule and Peltier phase images show heat is exchanged non-uniformly with the substrate. Also note the change in thermal phase in the RHS segment in the Joule images, which is an indication of a drastically altered thermoreflectance coefficient for the two insulating states.

The phase images of both Peltier (Figure 5.4c,h) and Joule (Figure 5.4e,j) confirm the premise that the signals occur at the domain junction, displaying the spreading pattern characteristic of a thermal point source along the NB and into the substrate. The relative signal strengths along the NB length show heat diffuses preferentially in the metal region of the RHS segment, possibly owing to its higher thermal conductivity.[103] Joule activity along the Au-covered-NB region acts as a reference for C_{TR}; this is known to be negative for Au at this illumination wavelength. Given this reference C_{TR} and the expected uniformity of Joule phase activity, we gain valuable insight about C_{TR} of the other regions. C_{TR} of the metal domains is always positive while the C_{TR} of the insulator domain on the RHS segment of measurement 2 is negative (Figure 5.4j RHS), similar to the scenario presented for NB_{type1} in Figure 5.2. However, the insulating state in the LHS segment during the same measurement run is roughly 180° out-of-phase from the aforementioned insulator domains, implying a positive C_{TR} (Figure 5.4j LHS). We postulate that this difference in sign of C_{TR} between the two insulating states distinguishes the two monoclinic phases of VO_2; that is, the reflectivity dependencies on a temperature variation of the two monoclinic states display opposing behaviors. Thus, the RHS segment was initially in the same state as the LHS segment; the insulator domain on the RHS during measurement 1 (Figure 5.4e) is roughly 180° phase shifted from the I_M domain in the RHS during measurement 2 (Figure 5.4j) for the same excitation bias. For clarity, the average phase values of the NB regions associated with this analysis are presented below the phase images in Figure 5.4e, j. The significant change in the thermoreflectance properties between the two insulating phases could be related to the

difference in reflective signatures of the two monoclinic phases under polarized light.[88,94,104] Further thermoreflectance measurements using a polarized light source could illuminate the underlying mechanism of the C_{TR} polarity change.

5.5 Discussion

Examination of the electrical resistance trends with respect to ambient temperature of the two NBs further supports this conclusion. Refer to Figure 5.5. The total resistances were obtained using a two-probe measurement of the voltage drop across the device contacts; the contact resistance was determined to be negligible by comparing four-probe and two-probe measurement results. NB_{type1} shows the expected steady decrease in resistance before becoming fully metallic. In contrast, NB_{type2} exhibits a large jump in resistance at 335 K, coinciding with the appearance of the first metal domain. This implies that either R_{DW} is quite large, ~300 kΩ, or that I_{M1} converted to the more resistive I_{M2} insulating state, similar to the behavior observed by Kasirga *et al*. (91). Both NBs display the expected Arrhenius behavior for a non-degenerately doped semiconductor before the metal domains emerge, $R_I(T) = R_{I,0}e^{E_a/k_BT}$. However, NB_{type2} has a markedly lower overall resistance despite similar sample geometries, and presumably equivalent electrical resistivities. Thus, the two NBs have quite dissimilar activation energy: E_a (NB_{type1}) = 0.30 eV, E_a(NB_{type2}) = 0.11 eV. Both values are within the range reported in literature: 0.08 to 0.36 eV.[102,104,105,106] The lower activation energy suggests NB_{type2} to be more highly doped. When the domains coexist, the total resistance R_T of the NB is comprised of four factors:

$$R_T(T) = x(T)R_{I_M}(T) + [1 - x(T)]R_M(T) + R_C + R_{DW}$$

where *x(T)* is the length fraction of the NB in the I_M state at a given ambient temperature, R_{IM} and R_M are the expected insulating and metal resistances, respectively. The contact resistance, R_C, can be ignored in this analysis. We used this equation and the extrapolated Arrhenius fitting at multiple ambient temperatures to determine R_{DW} of the more uniform NB (NB_{type1}), which we found to be 39 ± 7 kΩ. This value is in agreement with the figure put forth in Wei et al.[105]

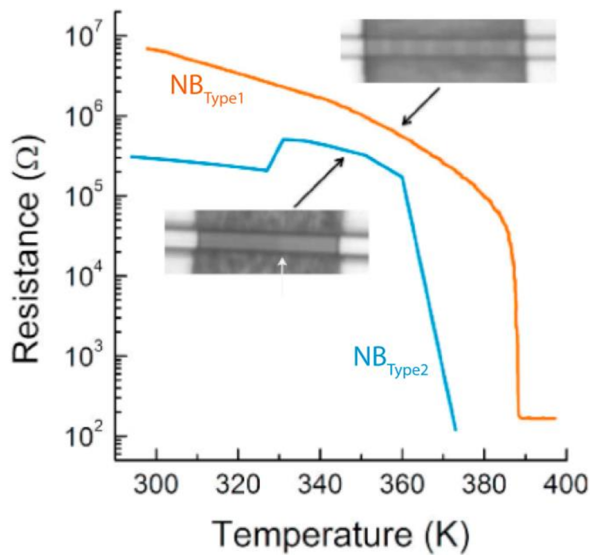

Figure 5.5: Resistance as a function of ambient temperature comparison of the two NBs. NB_{type2} exhibits a jump in resistance coincident with the emergence of metallic domains due to the conversion from I_{M1} to I_{M2} and the additional resistance of the domain walls.

As a result of this analysis, collaborators at UCBerkeley and Pennsylvania State University assessed the likelihood that domain wall orientation could correspond to the adjacent monoclininc domain type. They calculated the most favorable domain wall orientations through analysis of the elastic energy of the M_R/I_{M1} and M_R/I_{M2} junctions, based on Khachaturyan's microelasticity theory.[107] They show that the preferred angle of the domain

wall is the one that would minimize the total elastic energy of the interface[108]; accordingly, M_R/I_{M1} will favor an acute angle of 56° with the NB top surface while M_R/I_{M2} may display an 89° or 33° acute angle (Figure 5.6). These analytic results are consistent with the experimentally identified monoclinic states: the M_R/I_{M1} domain wall exhibits an angle of 48-52° and M_R/I_{M2} presents as a 90° interface (Figures 5.2 and 5.4). More details on the applied model and calculations of domain wall configurations can be found in references 100 and 108.

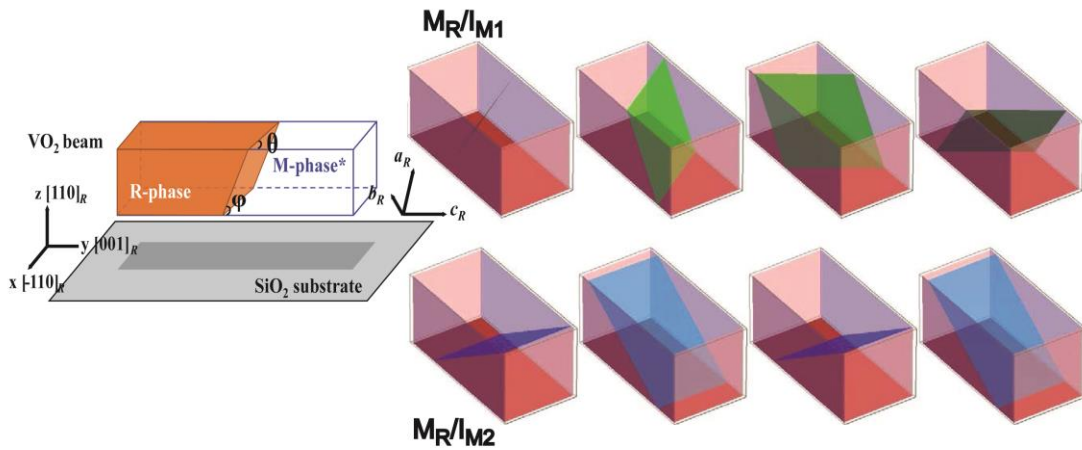

Figure 5.6: 3-D plots of preferred domain wall orientations: θ=56˚ for M_R/I_{M1} (green) and θ=89˚ for M_R/I_{M2} (blue). These domain walls exhibit reduced area, minimizing total elastic energy for the interface and are thus considered favorable.

The jump in resistance, sign change of the C_{TR}, and transformation of the interface angle of NB_{type2} denote the change in monoclinic crystal structure in the M-I coexisting state. $T_{MIT\text{-}type2}$ is a lower temperature than $T_{MIT\text{-}Bulk}$, indicating compressive strain driving the NB to the phases with smaller lattice constants (M_R, I_{M1}). The irregular domain patterns in addition to strong Joule activity at the M-I interface suggest poor substrate bonding, which would

reduce tensile stress felt by the NB upon cooling from the high growth temperature (~ 1000 °C). Thus, NB_{type2} was initially in the I_{M1} state. At elevated temperatures, the appearance of metal domains alleviates compressive strain while inducing tensile strain in the adjacent insulating domain. The induced strain, accompanied by intense Joule heating in the RHS segment generated by the current applied during the measurement, stimulated the conversion from I_{M1} phase to I_{M2}.

VO_2 NBs with good substrate adhesion would experience tensile strain at the temperatures used in this experiment. Homogenous periodicity and uniform thermal signal in the substrate demonstrate uniaxial tensile strain in NB_{type1} along the NB long axis, fixing the insulating domain to the I_{M2} phase with a longer lattice constant. The higher overall resistance and the persistence of I_M domains with vertical interfaces to 390 K, well above $T_{MIT\text{-}Bulk}$, further support this assertion. The polarity of the C_{TR} of the I_M phase in $NB_{type1}$is negative and is therefore I_{M2}, a conclusion confirmed by Raman spectroscopy.

There are several caveats worth calling attention to in this measurement, some of which have been already mentioned. Careful observation of the NBs during data accumulation was required because any variation in the optical signal negates the benefits introduced by averaging; the configurations of the NBs are quite sensitive to temperature fluctuations. As is seen in the thermal images, Joule heating, and to a lesser extent the Peltier thermal signals dissipate into the device substrate inducing background heating of the device. The impact of this heating would be exacerbated with additional bias cycles. In these measurements, we have indeed observed a baseline temperature increase, the most prominent shift occurred during measurements of NB_{type2} at the highest applied bias. This

effect is attributed to the significant Joule heating, but only increased the stage temperature by < 4° C over the course of 6500 averaging cycles (2 hours). Even so, the domain configuration in NB_{type2} did change after 4700 imaging cycles. Even with considerable background heating, the differential nature of the thermoreflectance measurement would negate this effect in regard to reflectivity acquisition and processing. Substrate heating would introduce a relatively slow temperature drift with a time constant much larger than the bias period, and would present as a DC offset which cancels out during image processing. The main issue created by background heating is the potential for domain wall movement or sudden phase changes, as seen in NB_{type2}.

The main challenges in measuring these very small devices are dictated by the optics. Image acquisition at 250x magnification results in a very shallow depth of field. At very long averaging times, the image blurs and the thermal signals start to drift. This effect is worsened with higher applied bias primarily due to slight movements of the device itself in response to the localized heating and thermal expansion in the experimental apparatus. We selected 500 cycles for the target averaging times since the data are virtually stable over the averaging window and offers a good compromise between sufficient thermal signal-to-noise ratio and minimal optical distortion. The thermal signals versus averaging time are plotted in Figure 5.7 for NB_{type2}.

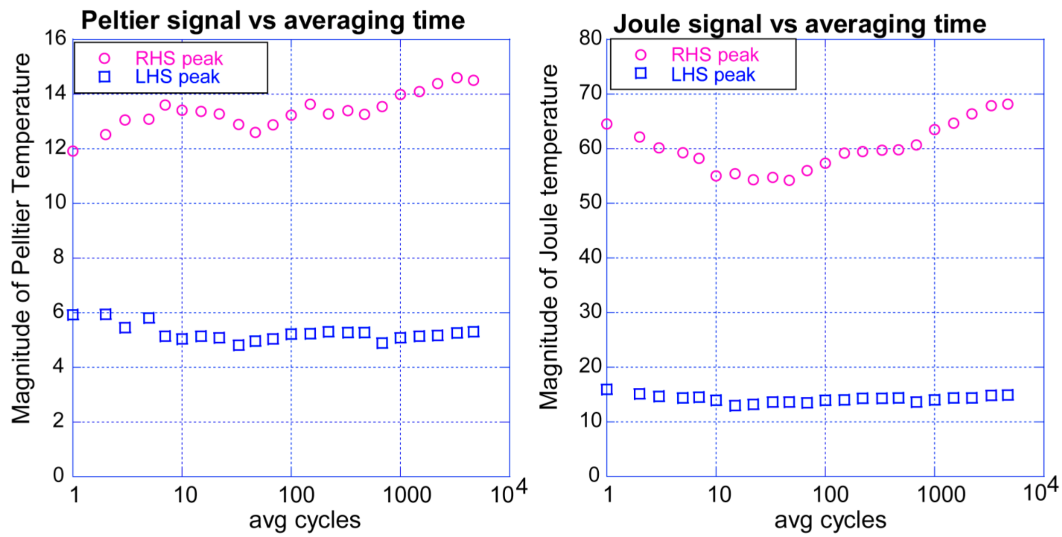

Figure 5.7: The variation in the magnitudes of temperature for NB_{type2} with 8 μA applied at 348 K. NB_{type2} represented the worst case scenario as it displayed the greatest heating, especially in the RHS peak. The averaged maximum deviation from the average temperature value spanning 100 to 1000 cycles is 10%; the data deviates by 20% over the two hour window.

Chapter 6 Design and fabrication of high temperature vacuum thermostat

Careful consideration is required when performing electro-thermal measurements at high temperatures. Potential detrimental effects can range from the presence of additional parasitic heat flow paths to the loss of sample integrity due to oxidation, contamination, or annealing effects. Implementation of the measurements in a vacuum environment removes convection in the experiment while eliminating the potential of sample oxidation. However, thermal conductance through the probes and probe leads extending out of a vacuum chamber can still be a source of significant error in high temperature thermoelectric characterization, as can the effect of Seebeck voltages inherent in the wiring junctions due to significant temperature gradients. All this must be addressed in the design of a high temperature characterization apparatus. In this chapter, the development of two high temperature thermostats used for this work is described. A third was initially employed for thin film measurements; more information about this thermostat is found in reference 31.

6.1 General Considerations

Vacuum insulation is essential for thermal management of any high temperature system. Convective heat loss is minimized, which has the additional benefit of reducing the power draw necessary to sustain high temperature in the measurement region. This work was executed in a high vacuum of ~10^{-6} mbar at temperatures up to 900 K, though the chambers have the potential to achieve higher temperatures. The vacuum thermostats were fabricated using high quality 316 L and 304 stainless steel. High vacuum components were

vacuum-welded to the chamber to create access flanges and feed-throughs for electrical leads and chamber evacuation. Ambient temperature control is accomplished using two high power density heater cartridges (up to 170 W/inch^2) installed in a copper heat sink/sample stage. Stainless steel radiation shielding consisting of several discrete layers of shim stock is utilized to help maintain temperature uniformity in the test region and thus deter parasitic Seebeck voltages that may appear in the measurements. The copper sample stage is further isolated from the surrounding environment by limiting its contact with the chamber to an isolated standoff with low thermal conductivity. The chamber assemblies and sample stages were initially baked to reduce volatiles from component outgassing. These components are displayed in Figure 6.1 in pictures of the bulk measurement chamber.

We employ refractory and inert (Pt) high temperature metals for probe tips and leads whenever direct sample contact is made. These materials have high melting points, low coefficients of thermal expansion, and are extremely stable to thermal cycling in the temperature range of the vacuum thermostat. Tungsten probe tips are primarily used for electrical measurements, while we utilize type R (Pt/13 % Rh-Pt) thermocouples for device temperature determination. A type K thermocouple (Ni-Al/Ni-Cr) is mounted in the stage and read by a PID controller governing the ambient heaters for each thermostat. We utilize type K thermocouples for ambient temperature sensing for their high measurement sensitivity over a wide temperature range (0 K to 1500 K). In addition, the materials that comprise the couple are robust and chemically inert and are significantly less costly than platinum. All heaters and general probe leads are made of copper insulated with a high temperature braided ceramic.

For thermoelectric measurements, thermocouple materials are selected for the small Seebeck voltages of the wires, 3-10 μV/K relative to other available materials in the measurement temperature range; their Seebeck voltage calibration data is well-known. The bare wire is run through alumina rods for electrical insulation and to construct a rigid probe. All probe leads are long and kept as thin as is practical to increase thermal resistance (R_{th}) and thus minimize the heat flux (Q) through the lead: $\Delta T_{\mathrm{lead}}=Q*R_{th}$. Any inhomogeneity/junction in the electrical leads will induce additional Seebeck voltages and invalidate the thermocouple calibration. Hence, the single thermocouple wire is continued from the measurement region for a length that gives an acceptable Q to the chamber feed-through (type R or K, accordingly). Outside the chamber, extension grade wiring is used and the thermocouple leads are run through an isothermal block to guarantee the temperature equivalence of all leads before entering the nanovolt meter/temperature sensor. We allowed thermal equilibrium to be reached in the chamber before beginning any measurements; to reduce thermal gradients across the contact between the samples and the probe tips and thermalize the leads for improved measurement accuracy.

6.2 Bulk measurement stage

We designed and fabricated a measurement stage for simultaneous measurement of both electrical conductivity and Seebeck coefficient of bulk materials (see Figure 6.1 for a schematic). In addition to the copper heat sink/ambient heater configuration that comprise the measurement stage, two boron nitride blocks each with an internal resistive heater are used to suspend the sample across a gap. The temperatures of the individual boron nitride blocks can be independently controlled to generate a temperature differential across the

sample and thus induce Seebeck voltage. Boron nitride is a machinable ceramic and is exploited in these experiments for its high thermal conductivity and highly insulating electrical properties. Each block has a recessed area in which the sample fits snuggly for heat sinking and a channel where a type R thermocouple can contact the sample along the minor edge. This design enables one-dimensional heat flow across the sample and utilizes the thermocouple wires for both temperature and voltage measurement probes during measurement of the Seebeck coefficient. Thermally conductive silver or platinum paint is applied at the thermocouple tip to secure thermal contact with the sample during thermal expansion of the chamber components with temperature ramping. Similarly, we apply high temperature thermal paste between the sample and the stage. Four tungsten probes are angled through a molybdenum probe mount with three degrees of freedom to set on the sample surface edge; these probes create an electrical pressure contact for measurement of electrical resistivity via the van der Pauw technique. Tungsten wiring is also used as probe leads.

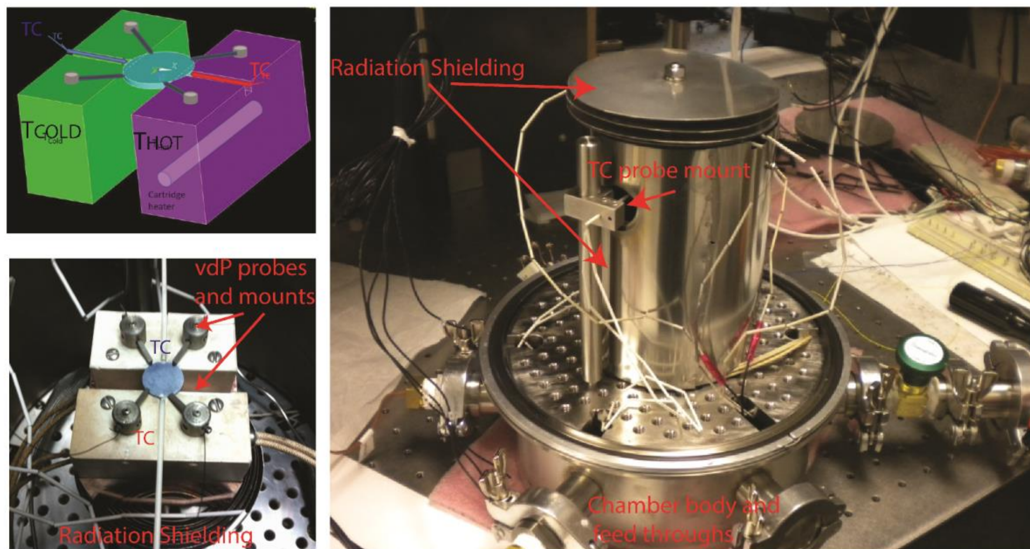

Figure 6.1: The bulk measurements chamber, viewed with vacuum lid off. Upper left depicts a diagram of the bulk measurement stage during the design phase, realized in the photo in the bottom left. The right hand photo illustrates thermal isolation of the measurement region.

Calibration measurements were performed on a lightly doped Mg_2Si bulk sample synthesized and previously measured at JPL. The results for electrical resistivity and the Seebeck coefficient are shown in Figure 6.2.

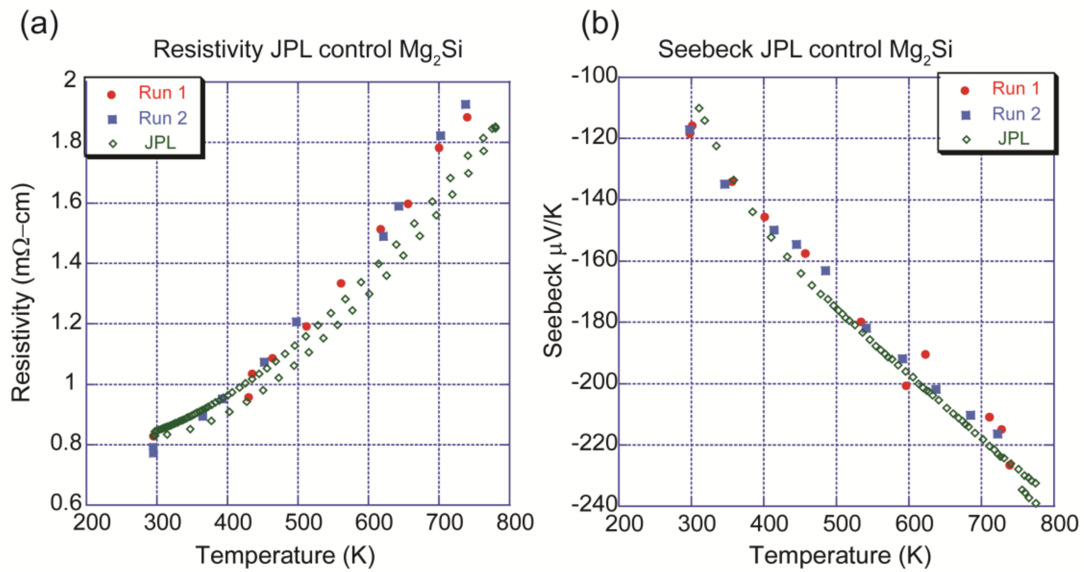

Figure 6.2: Calibration data of the bulk measurement stage for 0.15 % Bi doped Mg_2Si pellets, in comparison with measurements of the same sample performed at JPL. (a) van der Pauw electrical conductivity and (b) In-plane Seebeck measurement calibration results.

6.3 Chamber for optical measurement

Each chamber is built with the ability to interchange the sample measurement stages and implement the electrical measurements mentioned in the previous sections. However, the optical thermostat is designed specifically for high temperature thermoreflectance imaging. An optical viewport made of high quality sapphire with anti-reflectance coating is incorporated into the chamber lid. The lid itself is recessed to achieve the close working distance required for high magnification imaging. Four probe arms feed-through the chamber wall within a mechanical bellows to externally accessed x, y, z, θ micromanipulators. Consequently, multiple areas of the device under test can be probed during a measurement run without breaking vacuum. In addition, there are extra feed-throughs in the chamber body for supplementary electrical or thermocouple probe leads,

depending on the specific measurement requirements. A picture of the chamber during thermoreflectance measurement and schematic of the internal design are shown in Figure 6.3.

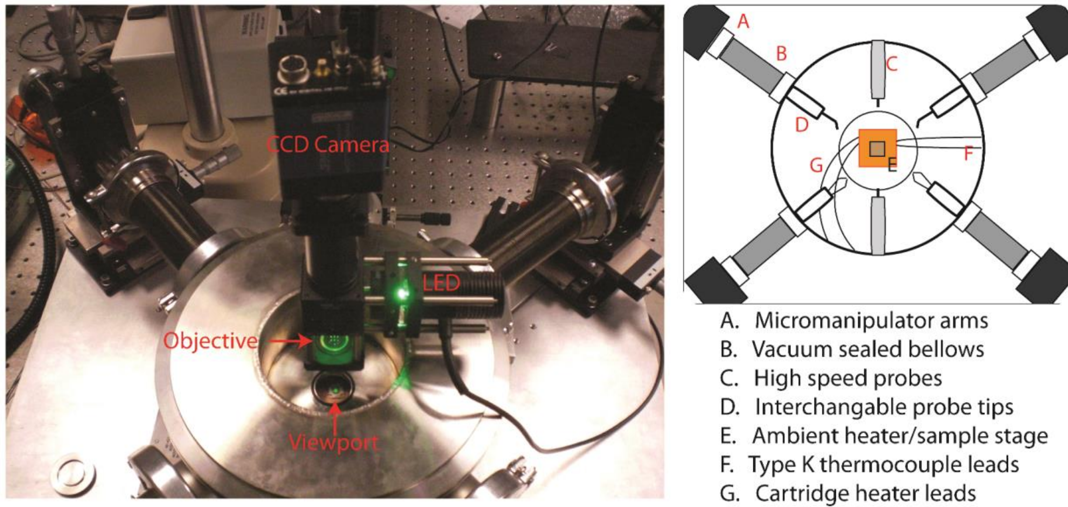

Figure 6.3: Optical thermostat during high temperature thermal imaging and internal schematic of chamber components.

The fast thermoelectric transients requisite of the transient Harman technique are resolved with the sample stage and circuitry as described in Singh et. al.,[31] with the exception that the stage for high temperature measurements was expanded to form a heat-sink encompassing two cartridge heaters for ambient temperature control. The thermoelectric device is mounted using thermally conductive silver or platinum paste onto alumina-on-gold packaging. This packaging serves to electrically isolate two impedance-matched transmission lines from the package backside-ground. The sample is wire bonded to these transmission lines, which directly connect to the Cu signal pin of a high speed coaxial cable, specially designed to withstand high temperatures and maintain circuit impedance.

Galinstan, a liquid eutectic alloy, is applied to the tips of the signal pin to maintain good electrical connection for the duration of the measurement. The cable ground (the outer sheath) is isolated from the center pin by a SiO_2 dielectric layer and positioned in intimate contact with the package ground. An impedance of 50 Ω was maintained throughout the circuit to minimize reflections at device turnoff.

Chapter 7 Conclusions

Recent innovations in material science have enabled material engineering at the nanoscale and stimulated renewed interest in thermoelectric generation as a viable technology. Accordingly, novel materials have demonstrated improved efficiency through experimental characterization. But perhaps more importantly, these measurements inform the theoretical understanding of device behavior at the nanometer level. Research into the development of high ZT materials has steadily evolved over the past decade; the figures of merit exhibited by many different material systems have steadily improved, achieving $ZT \approx 2$ in recent years.

Nevertheless, it is the potential for application that essentially opens the door to funding for research and implementation of a new technology. The most likely area thermoelectric devices will have the greatest impact is through incorporation into the automotive industry. The internal combustion engine constitutes well over 90 % of energy supplied for transportation, and is anticipated to continue to do so over the next thirty years.[109] However, vehicle exhaust is the largest source of environmentally harmful air emissions and the rising fuel demand is increasing the cost of petroleum. Even modest reductions in wasted heat energy will result in billions of dollars of fuel savings in the United States.

It is estimated that a device $ZT > 2$ at the temperatures of either the vehicle exhaust or cooling system will translate into 10 % decrease in fuel consumption.[110] Unfortunately, the most promising and widely studied material systems for efficient energy conversion are also the most scarce and/or exhibit high supply risk,[111]which translate to high consumer cost. This includes any material family that contain the elements bismuth (Bi), antimony (Sb),

tellurium (Te), and any of the rare earth and platinum group metals.[111] Mg_2Si and possibly some half-Heusler alloys are the most likely candidates for widespread deployment into thermoelectric generators for waste heat recovery in automobiles. Figure 7.1 illustrates the periodic table color coded in terms of elemental scarcity and production and reserve supply risk (Herfindahl-Hirschman Index or HHI values).

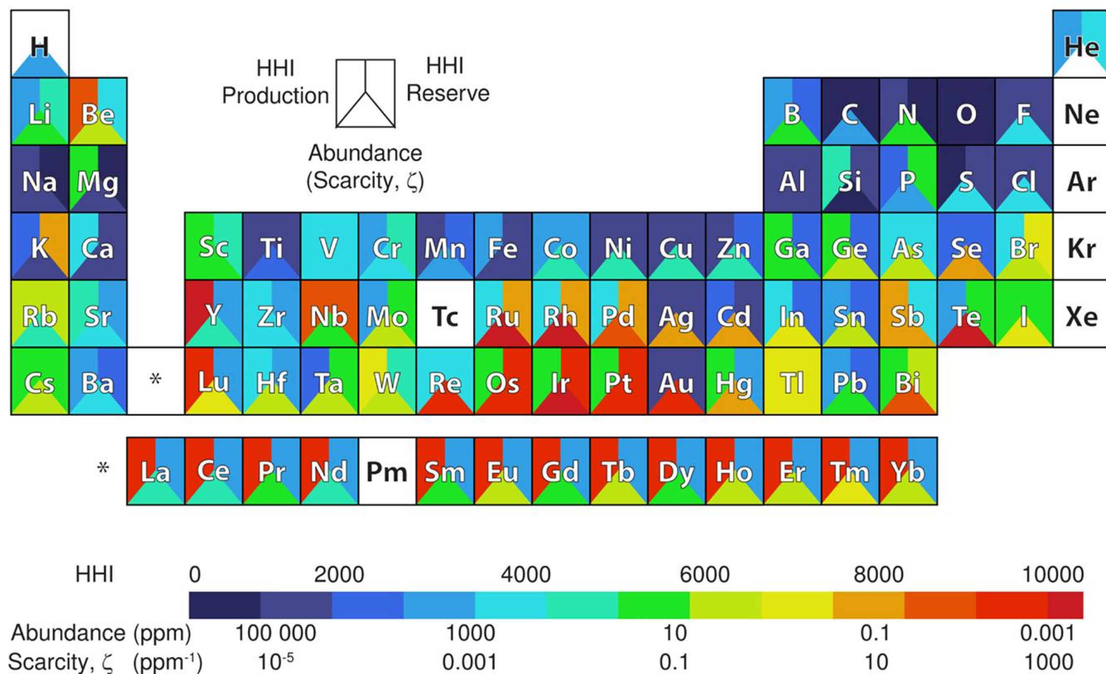

Figure 7.1: The periodic table of elements with color indicators of elemental abundance (scarcity) and the Herfindahl-Hirschman Index values (HHI) signifying market concentration (reserves) and geopolitical data (elemental production) which comprise supply risk. (Figure from reference 111)

It is important to note that is it not simply a material specific goal, overall generator performance must achieve efficient and cost-effective energy conversion. This may be accomplished through minimization of interfacial losses from parasitic resistances and/or thermal expansion coefficient mismatch, innovative module design such as with segmented

couples, the optimization of heat flow geometry with device thermal resistance, and, of course, utilization of cheap and abundant materials. The demand for higher fuel efficiency will encourage not only thermoelectric material research but also creative module design and thus drive the proliferation of thermoelectric energy generation technology.

Extensive physical testing of both the materials and the completed module is imperative to identify desired material attributes and eventually predict high temperature behavior. Once the fundamental physical mechanics are well-established, focus can then be shifted toward more inexpensive materials or employing alternative synthesis methods for scale-up to make thermoelectric energy generation economically feasible. The experimental methodology and apparatus presented in this thesis facilitate the advancement of thermoelectric technology by enabling more accurate characterization at high temperatures, similar to operational environment. Only slight modification to the measurement stage will be necessary to additionally characterize thermoelectric modules.

In this work, we successfully apply the transient Harman technique to thin film energy conversion devices with optimized design. We report the first CCD-based thermoreflectance temperature maps performed on thermoelectric devices at high ambient temperatures. These accomplishments facilitate the determination of the individual thermoelectric material properties and figure of merit of a device in a single high temperature measurement run. Accuracy in thermal imaging is achieved through careful calibration of the thermoreflectance coefficient using a novel technique ideally suited for the high vacuum environment of the high temperature measurement apparatus. The key experimental results and potential directions of research are summarized in the following sections.

High temperature thermoreflectance imaging and transient Harman characterization of thermoelectric energy conversion devices

This work[76] validates the use of the transient Harman technique to obtain the Seebeck voltages and thus the cross-plane ZT of thin-film thermoelectric materials at high temperatures, provided an optimized device design with a good ground electrode. When utilized in conjunction with thermoreflectance thermal imaging, it is a feasible approach that not only determines cross-plane Seebeck coefficient and the electrical and thermal conductivities, but also exposes device flaws and potential failure points during a single measurement run to high temperature. Hence, we avoid discrepancies and error accumulated over multiple measurements by applying these combined techniques.

We demonstrate these claims by using the collated data from the transient Harman and thermoreflectance measurements on multiple device sizes: we were able to determine the nature of the device defect and simulate the three dimensional electrical and thermal paths with finite element modeling. In this way, the thermoelectric properties of the thin film are extracted in spite of substantial processing faults. The poor device quality, i.e. atypical peeling/flaking of the upper device layers from the Au-bonded substrate, made the direct measurement of ZT impractical. Moreover, apparent metal diffusion or surface degradation limited the highest temperature for data acquisition. This is unfortunate as 0.2 % ErAs:InGaAs possesses a ZT > 1 at temperatures above 600 K; direct transient Harman characterization of high ZT values has yet to be realized on thin films. These high temperature results suggest the need to further develop the device design in order to address high temperature parasitic effects and improve diffusion barriers before full

confidence in this technique is achieved. As in-depth analyses optimizing thin film devices for transient measurements have only been carried out at room temperature, additional simulations that take into account temperature dependent material properties performed with thermoreflectance imaging could be the subject of future work.

Characterization of the temperature dependence of the thermoreflectance coefficient for conductive thin films

The change in the thermoreflectance coefficients as a function of temperature is presented for common metals used in device electronics[52] in order to establish their expected variation for high temperature thermal imaging. While the absolute values of the coefficient may vary with experimental optical system (lens coatings, numerical aperture, etc.), their temperature dependence is an intrinsic material property and therefore is directly applicable to various thermoreflectance investigations. The average rate of change in the thermoreflectance coefficient (C_{TR}) is in general quite small, though aluminum and gold (under 470 nm illumination) exhibited the highest variation in C_{TR} over the measurement temperature range: approximately 0.22 x 10^{-4} and 0.30 x 10^{-4} per 100 K temperature change, respectively. For aluminum, this is quite substantial considering the small values of C_{TR}; we ascribe this result to its large thermal expansion coefficient. The transparent SiN_x passivation layer has a non-monotonic effect on the thermoreflectance coefficient, determined by the optical interference of the Fabry-Perot etalon formed in the layer. While this may be detrimental to the strength of the reflectivity signal, it can also be selectively adjusted to enhance the signal with careful fine-tuning of the illumination wavelength and dielectric layer thickness.

Ideally, these measurements should have spanned the entire temperature range of the vacuum thermostat; however, severe device degradation restricted the upper temperature limit. The results reported here have established the validity of the technique and further measurements of improved samples, including copper at wavelengths near 600 nm illumination, will provide a more complete reference table. Additionally, more data points with different passivation layer thicknesses can help refine the analytical model presented to explain the effect of passivation and determine optimal layer thicknesses for the specific sample metallization. Curiously, platinum displayed opposing behavior with temperature as compared to the other metals in this study: the coefficient of thermoreflectance increases with temperature. This would imply that the dielectric spectrum of platinum shifts to higher energies near this particular transition, if the data extracted from Wilson *et al*. is correct. This is certainly a possible outcome and may be attributed to changes in the electronic transitions and thus absorption dominating the temperature response given the smaller thermal expansion coefficient of platinum. It would be interesting to understand more clearly the temperature dependency of the thermoreflectance coefficient for the various metals on the microscopic level.

Direct observation of nanoscale Peltier and Joule effects at metal-insulator domain walls in vanadium dioxide nanobeams

These results directly reveal the extremely local Peltier and Joule effects across the M-I domain walls.[100] Thermal images show that while alternating Peltier heating and cooling at neighboring domain interfaces exchange energy through the nanobeam, Joule heating dissipates in the substrate and can be an indicator of the quality of substrate adhesion. This

insight and the ability to distinguish between insulating phases determine the underlying impact of stress on the nanobeam and led to the revelation of the favored wall configurations for each monoclinic phase from microelasticity theory.

Furthermore, we conclude that electrical resistance comprised at the domain wall generates concentrated and significant Joule heating at the M-I interface. This heating dominates the thermal behavior of the nanobeam and is responsible for converting the phase of adjacent domains. However, from the electrical perspective, the domain wall resistance is much smaller than the total effective resistance across the nanobeam. Thus, subtle electronic behavior is masked from observation in measurements of the total electric resistance. Many authors speculate that a Schottky junction forms at the interface between the metal and insulating domains, and indeed preliminary analysis of the individual image 'buckets' at alternating current polarity taken during thermoreflectance exhibit an asymmetry not shown in typical (ohmic) thermoelectric devices. Figure 7.2 displays a comparison of the change in reflectivity (ΔR) of the nanobeam to that of a thermoelectric microcooler.

The presence of a Schottky barrier at the M-I junction is the explanation most consistent with experimental results, where the diode resistance is overwhelmed by the series resistance of the nanobeam resulting in a roughly linear IV curve. Consequently, the additional harmonics associated with diode behavior could affect the Peltier temperature magnitude, specifically; the signal may be distorted given a large anomalous contribution at higher applied currents, but most likely presents here as a large signal offset. The next step would be to analytically examine the individual image buckets with a diode model that accounts for not only the diode resistance but also the large series resistances of the

nanobeam and includes the slight influence of the diode effect on the calculation of the Peltier signal. Alternatively, additional bipolar measurements utilizing a square pulse excitation would remove harmonic considerations from the measurement and may facilitate the extraction of the Schottky diode signature. Quantizing the local Peltier/Seebeck coefficients is another important next step. This requires the detailed modeling of heat flow in the nanobeam and characterization of the thermoreflectance coefficient at the metal/insulator junctions. Due to the large and possibly nonlinear change in sample reflectivity near the M-I transition, accurate temperature measurement may require the deposition of a thin layer of electrically insulating and thermally conductive material with known thermoreflectance coefficient; though this action may fundamentally affect the domain organization in the nanobeam.

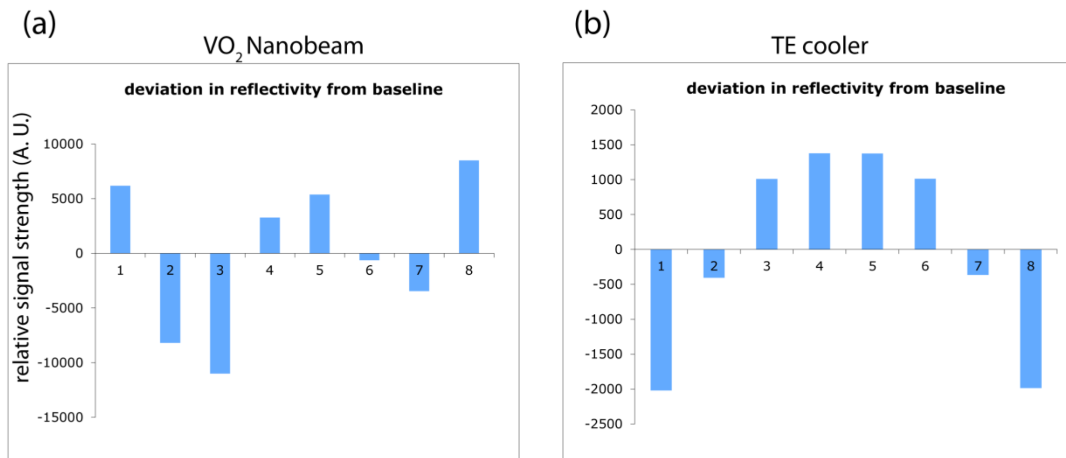

Figure 7.2: Comparison of the raw image buckets relative to the baseline reflectance (ΔR) of a VO_2 nanobeam (a) and a thermoelectric cooler (b) taken with the 8-bucket thermal imaging method. The typical thermoelectric cooler response shows a symmetric distribution while the nanobeam has an asymmetric reflectivity response to sinusoidal excitation. The y-axis is relative reflectivity strength in arbitrary units.

References

[1] Rowe, D. M., (ed.) *CRC handbook of thermoelectrics*. CRC press, Boca Raton, 1995.

[2] Cataldo, R. L. and Bennett, G. L., U. S. Space Radioisotope Power Systems and Applications: Past, Present, and Future. N. Singh (ed*.), Radioisotopes-Applications in Physical Sciences*, Chapter 22, InTech, 2011.

[3] Fleurial, J-P., *et al*., High Reliability, High Temperature Thermoelectric Power Generation Materials and Technologies. *Proceedings of the 3rd Thermoelectrics Applications Workshop*, US Office of Energy Efficiency & Renewable Energy, 2012.

[4] Multi-Mission Radioisotope Thermoelectric Generator (MMRTG) Fact Sheet. National Aeronautics and Space Admin., 2013. (http://mars.jpl.nasa.gov/msl/files/mep/MMRTG_FactSheet_update_10-2-13.pdf)

[5] Bell, L. E., Cooling, Heating, Generating Power, and Recovering Waste Heat with Thermoelectric Systems. *Science*, **321**:1457, 2008.

[6] Yang, J. and Stabler, F. R., Automotive Applications of Thermoelectric Materials. *J. of Elec. Mater*., **38**(7):1245, 2009.

[7] Kumar, S., Heister, S. D., Xu X., Salvador, J. R., and Meisner, G. P., Thermoelectric Generators for Automotive Waste Heat Recovery Systems Part 1. *J. Elec. Mater*., **42**(4):665, 2013.

[8] *HEATRECAR Project final report summary*, 2013. (http://cordis.europa.eu/result/rcn/58791_en.html)

[9] Singh, G. (Ap.), FY 2013 Progress report for advanced combustion engine research and development. DOE Vehicle Tech. Office, 2013.

[10] Meisner, G. P., Advanced Thermoelectric Materials and Generator Technology for Automotive Waste Heat at GM. *Proceedings of the 2d Thermoelectrics Applications Workshop*, US Office of Energy Efficiency & Renewable Energy, 2011.

[11] Crane, D. Thermoelectric Waste Heat Recovery Program for Passenger Vehicles. *Annual Merit Review,* DOE Vehicle Tech. Office, 2013.

[12] Hegarty, D., The woodstove-Satisfying a burning need. *Philips Research Password*, **28**:29, 2009.

---

[13] Biolite HomeStove (http://www.biolitestove.com/homestove/)

[14] Nuwayhid, R. Y., Shihadeh, A., Ghaddar, N., Development and testing of a domestic woodstove thermoelectric generator with natural convection cooling. *Energy Conversion and Mangement,* **46**:1631, 2005.

[15] Household air pollution and health Fact Sheet. World Health Organization Updated March 2014. (http://www.who.int/mediacentre/factsheets/fs292/en/)

[16] Lertsatitthanakorn, C., Electrical performance analysis and economic evaluation of combined biomass cook stove thermoelectric generator. *Bioresource Technology*, **98**:1670, 2007.

[17] Champier, D., Bedecarrats, J. P., Rivaletto, M., and Strub, F., Thermoelectric power generation from biomass cook stoves. *Energy,* **35**:935, 2010.

[18] Berkeley Air Monitoring Group, Evaluation of manufactured wood-burning stoves in Dadaab refugee camps, Kenya. USAID, 2010.

[19] Lawrence Livermore National Laboratory, Estimated U.S. Energy Use in 2013:~97.4 Quads. DOE EIA-0035, 2014.

[20] Snyder, G. J. and Toberer, E. S., Complex thermoelectric materials. *Nat. Mater*. **7**:105 2008.

[21] Vineis, C.J., Shakouri, A., Majumdar, A., and Kanatzidis, M.G., Nanostructured thermoelectrics: big efficiency gains from small features. *Adv. Mater*. **22**:3970, 2010.

[22] Shakouri, A. Recent developments in semiconductor thermoelectric physics and materials. *Ann. Rev. Mater. Res*. **41**:399, 2011.

[23] Hicks, L. D. and Dresselhaus, M. D., Effect of quantum-well structures on the thermoelectric figure of merit. *Phys. Rev. B,* **47**(19):12727, 1993.

[24] Hicks, L. D., Harman, T. C., Sun, X., and Dresselhaus, M. D., Experimental study of the effect of quantum-well structures on the thermoelectric figure of merit. *Phys. Rev. B, Condens. Matter,* **53**(16):10493, 1996.

[25] Heremans, J. P., Thrush, C. M., Morelli, D. T., and Wu, M-C., Thermoelectric Power of Bismuth Nanocomposites. *Phys. Rev. Lett.* **88**:216801, 2002.

[26] Zide, J. M., *et al*., Demonstration of electron filtering to increase the Seebeck coefficient in InGaAs/InGaAlAs superlattices. *Phys. Rev. B,* **74**:205335, 2006.

[27] Zide, J. M., *et al*., High efficiency semimetal/semiconductor nanocomposite thermoelectric materials. *J. Applied Phys.,* **108**:123702, 2010.

[28] Zebarjadi, M., *et al*., Thermoelectric transport in a ZrN/ScN Superlattice. *J. of Electr. Mater.,* **38**(7):960, 2009.

[29] Farzaneh, M., *et al.* CCD-based thermoreflectance microscopy: principles and applications *.J. Phys, D:Appl. Phys.* **42**:143001, 2009.

[30] Van der Pauw, L. J., A method of measuring the resistivity and Hall coefficient of lamellae of arbitrary shape. *Philips Research Rep.,* **13**:1, 1958.

[31] Singh, R. and Shakouri, A., Thermostat for high temperature and transient characterization of thin film thermoelectric materials. *Rev. Sci. Instrum.,* **80**:025101, 2009.

[32]Type R Thermocouple Reference Tables. Omega Engineering. (http://www.omega.com/temperature/Z/pdf/z210-211.pdf)

[33]Jha, P., Favaloro, T., *et al.* Cross-plane electronic and thermal transport properties of p-type LaSrMnO/LaMnO perovskite oxide metal/semiconductor superlattices. *J. Appl. Phys.* **112**:063714, 2012.

[34]ITS-90 Thermocouple Direct and Inverse Polynomials. Omega Engineering. (http://www.omega.com/temperature/Z/pdf/z198-201.pdf)

[35]Bahk, J-H., *et al.* High temperature thermoelectric characterization of III-V semiconductor thin films by oxide bonding. *J. Electron. Mater.,* **39**:1125, 2010.

[36] Cahill, D. G., Thermal conductivity measurement from 30 to 750 K: the 3ω method. *Rev. Sci. Instrum.,* **61**(2):802, 1990.

[37]Cahill, D. G., Katiyar, M., and Abelson, J. R., Thermal conductivity of a-Si:H thin films. *Phys. Rev. B,* **50**:6077, 1994.

[38]Borca-Tasciuc, T., Kumar, A. R., and Chen, G., Data reduction in 3ω method for thin-film thermal conductivity determination. *Rev. Sci. Instrum.,* **72**:2139, 2001.

[39] Dames, C. and Chen, G., 1ω, 2ω, and 3ω methods for measurements of thermal properties. *Rev. Sci. Instrum.,* **76**:124902, 2005.

[40] Feser, J. P., Scalable routes to efficient thermoelectric materials, PhD thesis, UC Berkeley, 2010.

[41]Kim, W., Thermal transport in nanostructured materials. PhD thesis, UC Berkeley, 2005.

[42] Glassbrenner, C. J. and Slack, G. A., Thermal Conductivity of Silicon and Germanium from 3 K to the Melting Point. *Phys. Rev. B,* **134**:A1058, 1964.

[43] Shanks, H. R., Maycock, P. D., Sidles, P. H., and Danielson, G. C., Thermal Conductivity of Silicon from 300 to 1400 K. *Phys. Rev. Lett.* **130**:1743, 1963.

[44]Yang, B., Liu, J. L., Kang, W. L., and Chen, G., Cross-Plane Thermoelectric Properties in Si/Ge Superlattices. *MRS Proceedings Fall Meeting,* MRS, 2001.

[45] Zhang, Y., *et al*., Measurement of Seebeck coefficient perpendicular to SiGe superlattice. *Proceedings of 21st International Conference on Thermoelectrics*, IEEE, 2002.

[46] Grauby, S., Forget, B. C., Hole, S., and Fournier, D., High resolution photothermal imaging of high frequency phenomena using a visible charge coupled device camera associated with a multichannel lock-in scheme. *Rev. Sci. Instrum.,* **70**:3603, 1999.

[47] Wang, X., *et al.* Characterization of Single Barrier Microrefrigerators at Cryogenic Temperatures. *J. Electron. Mater.* **38**(7):1309, 2009.

[48] Vermeersch, B. and Shakouri, A., Thermal Imaging of Peltier and Joule Effects. *IMAPS Thermal ATW*, 2010.

[49] Vermeersch, B., Bahk, J-H., Christofferson, J., and Shakouri, A., Thermoreflectance imaging of sub 100 ns pulsed cooling in high-speed thermoelectric microcoolers. *J. Appl. Phys.,***113**:104502, 2013.

[50] Favaloro, T., Kendig, D., Bian, Z., and Shakouri, A., Direct measurement of the thin film thermoelectric figure of merit at high temperatures. *APS March Meeting,* 2010.

[51] Favaloro, T., Singh, R., Christofferson, J., Essahri, Y., and Shakouri, A., Transient electrical and thermal characterization of InGaAlAs thin films with embedded ErAs nanoparticles. *APS March Meeting,* 2009.

[52] Favaloro, T., Bahk, J-H., and Shakouri, A., Characterization of the temperature dependence of the thermoreflectance coefficient for conductive thin films. *Rev of Sci. Instrum.* (to be submitted).

[53] Wilson, R. B., Apgar, B. A., Martin, L. W., and Cahill, D. G., Thermoreflectance of metal transducers for optical pump-probe studies of thermal properties. *Optics Express*, **20**(27):28829, 2012.

[54] Microsanj, LLC. Unpublished data.

[55]Komarov, P. L., Burzo, M. G., and Raad, P. E., A Thermoreflectance Thermography System for Measuring the Transient Surface Temperature Field of Activated Electronic Devices. *Proceedings of the 22nd SEMI-THERM Symposium,* IEEE, 2006.

[56]Winsemius, P., van Kampen, F. F., Lengkeek, H. P., and van Went, C. G., Temperature dependence of the optical properties of Au, Ag and Cu. *J. Phys. F: Metal Phys.,* **6**(8):1583, 1976.

[57] Christensen, N. E. and Seraphin, B. O., Relativistic Band Calculation and the Optical Properties of Gold. *Phys. Rev. B,* **4**(10):3321, 1971.

[58] Rosei, R. and Lynch, D. W., Thermomodulation Spectra of Al, Au, and Cu. *Phys. Rev. B,* **5**(10):3883, 1972.

[59] Pells, G. P. and Shiga, M., The optical properties of copper and gold as a function of temperature. *J. Phys. C: Solid State Phys.,***2**(2):1835, 1969.

[60] Humbert, A., Debever, J. M., and Hanus, J., Low energy interband transitions in aluminum. *Le Journal de Physique-Letters,* **38**(24):479, 1977.

[61] Rashidi-Hueyh, M. and Palpant, B., Counterintuitive thermo-optical response of metal-dielectric nanocomposite materials as a result of local electromagnetic field enhancement. *Phys. Rev. B,* **74**:075405, 2006.

[62] Sundari, S. T., Srinivasu, K., Dash, S., and Tyagi, A. K., Temperature evolution of optical constants and their tuning in silver. *Solid State Comm.* **167**:36, 2013.

[63]Heavens, O. S., *Optical Properties of Thin Solid Films.* Courier Dover Publications, New York, 1991. Chap. 4.

[64] Palik, E. D. (ed.), *Handbook of Optical Constants of Solids.* Academic Press, Boston, 1997.

[65] Duttagupta, S., Ma, F., Hoex, B., Mueller, T. and Aberle, A. G., Optimised antireflection coatings using silicon nitride on textured silicon surfaces based on measurments and multidimensional modeling. *Energy Procedia,* **15**:78, 2012.

[66] Zanatta, A. R. and Gallo, I. B., The Thermo Optic Coefficient of Amorphous SiN Films in the Near-Infrared and Visible Regions and Its Experimental Determination. *Appl. Phys. Exp.,* **6**:042402, 2013.

[67] Harman, T. C*.,* Special techniques for measurement of thermoelectric properties. *J. Appl. Phys.* **29**:1373, 1958.

[68] Harman, T. C., Cahn, J. H., and Logan, M. J., Measurement of thermal conductivity by utilization of the Peltier effect*. J. Appl. Phys*., **30**:1351. 1959.

[69] Buist, R. J., *CRC Handbook of Thermoelectrics,* edited by R. M. Rowe (CRCpress, Boca Raton, 1995) Chp. 18.

[70] Castillo, E., Hapenciuc, C., and Borka-Tasciuc, T. Thermoelectric characterization by transient Harman method under non-ideal contact and boundary conditions. *Rev. Sci. Instrum*., **81**:044902, 2010.

[71] McCarty, R., Thompson, J., Sharp, J., Thompson, A., and Bierschenk, J., Methodology for minimizing heat losses for the transient Harman technique at high temperatures. *J. Electron. Mater*., **41**:1274, 2012.

[72] Singh, R., Experimental characterization of thin film thermoelectric material and film deposition via molecular beam epitaxy. Ph.D. thesis, University of California, Santa Cruz, 2008.

[73] Singh, R., *et al.*, Direct measurement of the thin-film thermoelectric figure-of-merit. *Appl. Phys. Lett*., **94**:212508, 2009.

[74] Bian, Z. Zhang, Y. Schmidt, H., and Shakouri, A., Thin film ZT characterization using transient Harman technique. *Proceedings of 24th International Conference on Thermoelectrics,* IEEE, 2005.

[75] Venkatasubramanian, R., Siivola, E., Colpitts, T., and O'Quinn, B., Thin-film thermoelectric devices with high room-temperature figures of merit. *Nature,* **413**:597, 2001.

[76] Favaloro, T., *et al.* High temperature thermoreflectance imaging and transient Harman characterization of thermoelectric energy conversion devices. *J. Appl. Phys.,* **116**:034501, 2014.

[77] Dilhaire, S., Ezzahri, Y., Grauby, S., and Claeys, W., Thermal and thermomechanical study of micro-refrigerators on a chip based on semiconductor heterostructures. *Proceedings of 22th International Conference on Thermoelectrics,* IEEE, 2003.

[78] Wang, P., Bar-Cohen, A., Yang, B., Solbrekken, G. L., and Shakouri, A., Analytical modeling of silicon thermoelectric microcooler. *J. Appl. Phys*., **100**:014501, 2006.

[79] Székely, V., On the representation of infinite-length distributed RC one-ports, *IEEE T. Circuits Syst*., IEEE, **38**:711, 1991.

[80]Antonova, E.E. and Looman, D.C. Finite Elements for Thermoelectric Device Design in ANSYS. *Proceedings of 24th International Conference on Thermoelectrics,* IEEE, 2005.

[81] Cao, J., Fan, W., Zheng, H., and Wu, J., Thermoelectric Effect across the Metal-Insulator Domain Walls in VO2 Microbeams. *Nano Lett*. , **9**:4001, 2009.

[82] Fu, D., *et al.,* Comprehensive study of the metal-insulator transition in pulsed laser deposited epitaxial thin film. *J. Appl. Phys.,* **113**:043707, 2013.

[83] Morin, F. J., Oxides which show a metal-to-insulator transition at the Neel temperature. *Phys. Rev. Lett.*, **3**:34, 1959.

[84] Goodenough, J.B., Direct Cation-Cation Interactions in Several Oxides. *Phys. Rev.,* **117**:1442, 1960.

[85] Marezio, M., McWhan, D. B., Remeika, J. P., and Dernier, P. D. Structural Aspects of the Metal-insulator Transitions in Cr-Doped VO2. *Phys. Rev. B*, **5**:2541, 1972.

[86] Rakotoniaina, J. C., *et al.,* The thermochromic vanadium dioxide: 1. Role of Stresses and Substitution on Switching Properties. *J. Solid State Chem.*, **103**:81, 1993.

[87] Pouget, J. P., Launois, H., D'Haenens, J. P., Merenda, P., and Rice, T. M., Electron Localization Induced by Uniaxial stress in Pure VO_2. *Phys. Rev. Lett.*, **35**:873, 1975.

[88] Cao, J., *et al.,* Extended Mapping and Exploration of the Vanadium Dioxide Stress-Temperature Phase Diagram. *Nano Lett.*, **10**:2667, 2010.

[89] Jones, A. C., Berweger, S., Wei, J., Cobden, D., and Raschke, M. B., Nano-optical Investigations of the Metal-Insulator Phase Behavior of Individual VO2 Microcrystals. *Nano Lett.,* **10**:1574, 2010.

[90] Atkin, J. M., *et al.,* Stain and temperature dependence of the insulating phases of VO_2 near the metal-insulator transition. *Phys. Rev. B*, **85**:020101, 2012.

[91] Kasirga, T. S., Photoresponse of a strongly correlated material determined by scanning photocurrent microscopy. *Nat. Nanotechnol.*, **7:**723, 2012.

[92] Zhang, S., Chou, Y. C., and Lauhon, L. J., Direct correlation of structural domain formation with the metal insulator transition in a VO2 nanobeam. *Nano Lett.*, **9**:4527, 2009.

[93] Marini, C., *et al.,* Optical properties of $V_{1-x}Cr_xO_2$ compounds under high pressure. *Phys. Rev. B*, **77**:235111, 2008.

[94] Tselev, A., *et al*., Symmetry Relationship and Strain-Induced Transitions between Insulating M1 and M2 and Metallic R phases of Vanadium Dioxide. *Nano Lett.*, **10**:4409, 2010.

[95] Eyert, V. The metal-insulator transitions of VO2: A band theoretical approach. *Ann. Phys.(Leipzig)*, **11**:650, 2002.

[96] Lopez, R., Boatner, L.A., Haynes, T.E., Haglund, R.F., and Feldman, L.C. *Appl. Phys. Lett.*, **79**:3161, 2001.

[97] Wu, J-Q., Strain-induced Self Organization of Metal-Insulator Domains in Single-Crystalline VO_2 Nanobeams. *Nano Lett.*, **6**:2313, 2006.

[98] Cao, J., *et al.,* Strain engineering and one-dimensional organization of metal-insulator domains in single-crystal vanadium dioxide beams. *Nat. Nanotechnol.*, **4:**732, 2009.

[99] Lee, S., *et al.*, Axially Engineered Metal-Insulator Phase Transition by Graded Doping VO2 Nanowires. *J. Am. Chem. Soc.* 2013.

[100] Favaloro, T., *et al.,* Direct Observation of Nanoscale Peltier and Joule Effects at Metal-Insulator Domain Walls in Vanadium Dioxide Nanobeams. *Nano Lett*., **14**:2394, 2014.

[101] Gu, Q., Falk, A., Wu, J., Ouyang, L., and Park, H., Current-Driven Phase Oscillation and Domain-Wall Propagation in $W_xV_{1-x}O_2$ Nanobeams. *Nano Lett.*, ***7***:363, 2007.

[102] Miller, C., *et al.,* Unusually long free carrier lifetime and metal-insulator band offset in vanadium dioxide. *Phys. Rev. B*, **85**:085111, 2012.

[103] Oh, D. W., Ko, C., Ramanathan, S., and Cahill, D. G., Thermal conductivity and dynamic heat capacity across the metal-insulator transition in thin film VO2. *Appl. Phys. Lett.*, **96**:151906*,* 2010.

[104] Strelcov, E., *et al*., Doping-Based Stabilization of the M2 Phase in Free-Standing VO_2 nanostructures at Room Temperature. *Nano Lett.*, **12***:*6198, 2012.

[105] Wei, J., Wang, Z. H., Chen, W., and Cobden, D. H., New aspects of the metal-insulator transition in single-domain vanadium dioxide nanobeams. *Nat. Nanotechnol.*, **4***:*420, 2009.

[106] Cao, J., *et al.*, Constant threshold resistivity in the metal-insulator transition of VO_2. *Phys. Rev. B*, **82**:241101, 2010.

[107] Khachaturyan, A. G. *Theory of the structural transformation in solids.* Dover Publications: New York, 1983.

[108]Gu, Y., Cao, J., Wu, J., and Chen, L., Thermodynamics of strained vanadium dioxide single crystals. *J. Applied Phys.*, **108**:083517, 2010.

[109] Multi-year Program Plan 2011-2015. *Vehicle Technologies Program*, Office of Energy Efficiency and Renewable Energy, DOE, 2010.

[110]Singh, D. J., Thermoelectrics Theory and Structure. *Annual Merit Review,* DOE Vehicle Tech. Office, 2013.

[111] Gaultois, M. W., Sparks, T. D., Borg, C. K. H., Seshadri, R., Bonificio, W. D., and Clarke, D. R., Data-Driven Review of Thermoelectric Material: Performance and Resource Considerations. *Chem. Of Mater.,* **25**:2911, 2013.